A PELLET ABLATION MODEL IN THE PRESENCE OF MULTIPLE ENERGY CARRIERS AND ANALYSES OF PELLET INJECTION EXPERIMENTS

1986

YUJI NAKAMURA

A PELLET ABLATION MODEL IN THE PRESENCE OF MULTIPLE ENERGY CARRIERS AND ANALYSES OF PELLET INJECTION EXPERIMENTS

1986

YUJI NAKAMURA

ABSTRACT

In this thesis, we describe a new model to calculate the ablation rate of a solid pellet injected into a magnetically confined toroidal plasma. In this model, multiple energy carriers to the pellet surfaceare treated, because they are considered to be important to explain the enhancement of the pellet ablation in the neutral beam heated or the RF heated plasma. The model shows that the existence of multiple energy carriers changes appreciablly the dynamics of the shielding ablation cloud surrounding the pellet. When an energy carrier has a shorter range in the ablation cloud than the other energy carriers and heats the cloud far from the pellet surface, the Mach number of the cloud decreases and the subsonic region of the cloud flow expands. This reduces the cloud flow velocity near the pellet surface and the resultant ablation rate becomes different from that obtained by the single energy carrier approximation.

This ablation model is applied to calculations of ablation rate profile for the pellets injected into toroidal plasmas and compared with experimental results and other ablation models. For the pellet injections into NBI heated plasmas, the enhancement of the ablation rate due to fast ions is demonstrated, especially in the edge region of the plasma column where the thermal electron density and temperature are low, and the fast ion heat flux is relatively high. This result is consistent with the experimental result.

Transport for the pellet injection experiments in ISX-B

tokamak and Heliotron E are studied. We couple a standard transport code with our pellet ablation code, ABLATE. The energy balance and the confinement time before and after the pellet injection are shown. The experimental transport properties after the pellet injection in ISX-B can be explained by choosing the transport coefficients consistent with the Alcator scaling, which is the same transport as that used before the pellet injection. For the NBI heated current-free plasmas of Heliotron E, the plasma temperature can recover quickly after the pellet injection by enhanced thermalization of the fast ions due to increased plasma density. Then the total internal energy increases after the pellet injection.

By using the ABLATE code and a transport code which is modified to treat D-T burning plasmas, possibility of achieving $Q>1$ by the tritium pellet injection into deuterium plasmas is studied. Both the sufficient Two-Component-Torus effect and the deep penetration of the tritium pellet are essential factors to achieve $Q>1$ When the pellet with a radius of 2 mm and a velocity of 5 km/s is injected into a plasma of 'hot-ion-mode', $Q>1$ will be obtained.

ACKNOWLEDGEMENTS

I wish to thank Professor H.Nishihara for guiding and teaching me the way of thinking.

With appreciation, I acknowledge the support by Professors K.Uo, A.Iiyoshi, and T.Obiki. In particular, T.Obiki has given the opportunity and the place for my studying at the doctor course in Kyoto University.

Sincerely, I thank Professor M.Wakatani for his patient tutelage, many personal kindness, and investing in me an enormous fraction of his precious time over six years. It is to him that I owe practically almost all the basic ideas presented in this thesis.

Doctor M.Fukao has given useful discussions and suggestions. I also thank M.Fukao for his helpful comments on this manuscript. I acknowledge useful discussions with Doctors H.Zushi and S.Sudo about the pellet injection experiments in Heliotron E. I gratefully thank Professors T.Amano and M.Okamoto of Institute of Plasma Physics in Nagoya University for providing me with the tokamak transport code. Other members of Plasma Physics Laboratory in Kyoto University, and plasma physics group in Nuclear Engineering Department of Faculty of Engineering in Kyoto University have also contribute to my education in all things wise and wonderful.

Finally, I thank my wife Yumiko for her continuous aid.

TABLE OF CONTENTS

CHAPTER 1

Introduction

In magnetic confinement research of toroidal plasmas to achieve a break-even condition, much efforts have been made to raise or maintain plasma density against the particle loss due to unavoidable diffusion. In the present state of experiments, there are two ways for the particle supply. One is neutral gas puffing or gas injection, which is the blow-in of hydrogen gas isotopes into the plasma through a nozzle built into the wall structure. This means gas is supplied to the edge region of the plasma column. All experimental devices have this kind of system at least for plasma initiation. The other is pellet injection[1),2)], which has mainly been used to raise central plasma density in a short time. It seems easy to raise the plasma density simply by puffing gas. In large devices, however, the neutral gas introduced from the outside of the plasma is ionized in the peripheral region of the plasma column, where particle confinement is poor and it is not easy to raise the plasma density at the central region. This problem becomes more serious especially in devices with magnetic divertors, because the screening effect of the divertor blocks the penetration of gas into the core plasma[3)]. Pellet injection is a method to supply particles to a plasma by the ablation of a solid pellet injected directly into the core region of the plasma with high injection velocity. This method can supply particles efficiently to the central region of plasma, and deposition of ablated pellet particles in a scrape-off region surrounding a core plasma is small

even for a device with a divertor[4] .

The pellet injection has a desirable feature for particle supply to the central region of the plasma, but it has a possibility to induce serious plasma instabilities and degradate the plasma confinement. An appropriate pellet size, repetition rate of injection, and injection velocity must be compromized, considering stability and transport associated with the pellet injection as well as the technical restrictions of pellet formation and acceleration.

In this thesis, we study the physics related to the pellet injection theoretically, especially the ablation theory of the pellet injected into a magnetically confined plasma, and transport and stability analyses for high density plasmas after the pellet injection. Objectives of this study are (1) to built a model taking account of the presence of multiple energy carriers with different energies in the ablation process, (2) to develop a numerical code to calculate the ablation rate, ABLATE code, (3) also to develop a transport code coupled with the ABLATE code for studying the pellet injection experiments, and (4) to investigate a possibility of achieving $Q>1$ by tritium pellet injection into deuterium plasmas, where Q is the ratio of total fusion output to injected neutral beam power. In chapter 2, we will review both theoretical and experimental studies of the pellet injection and show the present status of the pellet fueling research. In chapter 3, by extending the neutral shielding model introduced by Parks and Turnbull[5),6)], we develop a new ablation model, in which multiple energy carriers incident to the pellet surface, such as thermal electrons, fast ions produced by neutral beam injection, or fast electrons produced

by RF heating, can be treated. In chapter 4, our model is applied to analyze the pellet ablation in the presence of the fast ions or the fast electrons as the energy carriers to the pellet[7]. The physical explanation of the results is discussed how the existence of multiple energy carriers affects the ablation rate of the pellet. Calculations of the ablation profiles for the pellets injected into toroidal plasmas are described in chapter 5. The effect of fast ions in a target plasma on the ablation rate profile is extensively investigated and the computational result by our model is compared with that by the Milora model[8], in which the effect of fast ions is also included in a different way. In chapter 6, we describe the transport code coupled with the ABLATE code to study transport properties after the pellet injection. The code is applied to simulate the pellet injection experiment in ISX-B tokamak. Analysis of pellet injection experiments in Heliotron E is discussed in chapter 7. This chapter also contains results of ablation rate profile for the pellet injected into the neutral beam heated plasmas. Transport analyses after the pellet injections into both Ohmically heated plasma and neutral beam heated currentless plasma are shown. MHD stability related to the pellet injection is also briefly discussed[10]. In chapter 8, we investigate a possibility of achieving $Q>1$ by the tritium pellet injection into deuterium plasmas with the neutral deuterium beam injection[11]. We use a transport model for D-T burning plasmas including the Two-Component-Torus effect (thermal tritium reaction with beam dueterons) and find essential factors to achive $Q>1$. Concluding remarks are given in chapter 9. We summarize main results and mention about future studies.

CHAPTER 2

Review of Pellet Injection into Magnetically Confined Plasmas

2.1 Introduction

In these years, physics of pellet injection into a high termperature magnetic confined plasma have been gradually understood in accordance with the increase of pellet injection experiments[1),2),21)]. As for pellet ablation process, usually models based on neutral cloud shielding have been used to understand experimental results of pellet injection into Ohmically heated plasmas[12)]. Many uncertainties about the ablation of the pellet, however, still remain[13)]. Improvement of the ablation model is required for studying pellet injection into neutral beam heated or electromagnetic wave heated plasmas and future burning plasmas. We will review recent pellet ablation theories and comment limitation and uncertainty of each model in section 2.2.

An important factor in the development of pellet fueling is injector technology. In section 2.3, the present status of pellet injector and possibility of pellet fueling with high injection velocity appropriate for reactor plasmas are discussed briefly.

In section 2.4, pellet injection experiments performed in tokamak or stellarator/heliotron[72),73)] devices are reviewed. In these experiments, pellet penetrations in Ohmically heated plasmas are consistent with the neutral cloud shielding model. In the pellet injection into plasmas with additional heating, it is shown

that non-thermal particles contribute to the ablation. In many experiments, improvement of comfinement properties associated with the pellet injection was observed.

Finaly, several applications of pellet injection to plasma diagnostics are given in section 2.5.

2.2 Development of ablation theories

When a pellet suffers heat flux from an ambient plasma, pellet particles are ablated from the surface and a dense and relatively cold gas cloud is formed around the pellet and most of the incident plasma particles are intercepted from hitting the pellet. We need to know the state of particles (e.g. neutral molecules, cluster ions, or ion pairs) ablated from the surface, since the energy required for the ablation is different by orders of magnitude. When a high energy electron incident to the solid pellet, it is expected that numerous secondary electrons of low energy are emitted. Since these secondary electrons are localized through energy loss due to collisional excitation of hydrogenic molecules in the vicinity of the surface, the resultant emmision of the secondary electron from the surface is significantly supressed[14]. The bulk of the energy of the primary incident electron is deposited as a heat through the collisional excitation at the surface. It is reasonable, therefore, that the diminant state of particles ablated from the surface is assumed molecular hydrogen.

Milora estimated the condition that self-shielding mechanism due to the ablation cloud becomes invalid[2] ;

$$q_\infty(\mathrm{eV/m^2s}) = \frac{n_e C_e}{4} 2T_e(\mathrm{eV}) < \frac{2\lambda v_p}{r_p \alpha}. \qquad (2.1)$$

Here r_p is the instanteneous pellet radius, v_p is the flow velocity of gas away from the pellet surface, $n_e C_e/4$ is incident electron flux to the pellet, λ is the sublimation energy (0.005 eV/atom), q_∞ is the external plasma heat flux, and α is a cross-section taking into account of both energy loss of the incident beam by

inelastic collisions and reduction of the forward particle flux by backscattering. From Eq.(2.1), it is found that a large pellet in a high temperature and high density plasma is easily self-shielded. Usually, the pellet ablation is governed by the self-shielding due to the ablation cloud.

Firstly, Gralnick investigated the self-sielding mechanism due to the ablation cloud[15]. He supposed that the ablation cloud was fully ionized in a region close to the pellet surface according to the ion evapolation model by Rose[16]. In this model, it is assumed that ions are emitted from the surface and the ionization energy is taken as the ablation energy of the pellet particles. He improved the previous unshielded ion evaporation model by solving hydrodynamic equations describing the motion of the ablation cloud, or under the self-shielding model. His analysis showed that about 50% reduction of the pellet ablation rate could be expected for high density thermonuclear plasmas (n_e=10^{15}cm^{-3}, T_e~10keV) in comparison with the unshielded ion evaporating pellet.

In the initial ORMAK experiments the higher ablation rate than those predicted by any ion evaporation models is observed[17]. It seems that this discrepancy comes from the assumption of the ablation energy of 36 eV in the ion evaporation models. The values estimated from the experimental data were closer to the sublimation energy, λ, than 36 eV. Moreover, in this experiment, the existence of a cloud is confirmed by the measurement of H_α line radiated from exited neutrals, which is several times larger than the pellet radius. In accordance with this experimental result, Parks et al.[5] and Vaslow[18] independently developed so called the neutral cloud shielding model. When a pellet is immersed in a hot plasma, a dense

neutral gas blanket is formed arround the pellet. As a result, the energy flux arrived at the pellet surface is significantly reduced. And they assumed that only electrons penetrating the shielding cloud carry the heat flux to the pellet surface. The electron flux is modeled by a monoenergetic beam subject to energy slowing down due to inelastic collisions. On taking account of the low sublimation energy of solid hydrogen isotope, only a small amount of energy flux to the pellet surface is enough to maintain the sufficiently thick cloud around the pellet. Although the ablation cloud is ionized by the incident electrons, the ionization degree in the the cloud, where the electron energy is substantially slowing down, is low. Therefore, the ablation cloud is considered to be neutral in the following self-shielding model. Parks and Turnbull numerically solved the hydrodynamic equations describing the transonic flow of the ablated neutral gas and the associated attenuation of the electron heat flux (Parks and Turnbull model, or PT model)[6] . In their model, they assumed reduction of the forward heat flux by elastic backscattering is somewhat larger than or comparable to that by inelastic collisions. Milora and Foster also solved the same problem and obtained the relation between the cloud thickness and the averaged incident power (we will call this model as the MF model in this paper)[19] . It is different from PT model that they assume spatial uniformity of energy deposition to the cloud and neglect the elastic backscattering of incident electrons. Later, Milora included the effect of the backscattering only for low energy electrons[8] . Both (PT and MF) models showed that the intrinsic shielding mechanism of the cloud dominates the dynamics of the ablation cloud and ensures the heat flux arrived at

the surface is negligibly small in comparison to the heat flux from the background plasma.

In the neutral shielding models, thermal conduction effects have been neglected. It was pointed out in Ref.(20) that the temperature gradient obtained from the neutral shielding model at the pellet surface yields heat conduction flux comparable with free fall heat flux of the incident beam. It is a posteriori not justified to neglect the thermal conductivity. It should be noted, however, that the inclusion of the collisional thermal conduction term in the pressure equation would not necessarily resolve the problem. The assumption of the local thermal conduction is only valid, if the mean free path of the energy carriers is sufficiently small compared to the scale length of the temperature gradient. Lengyel pointed out that hot electrons residing in the high electron temperature wing of the temperature gradient may transport energy to the colder region through collisionless motion, even though the collisional conduction flux based on the local temperature values is negligibly small[13].

The assumption of a monoenergetic particle beam for incident fluxes is one of disputable points in the neutral cloud shielding model. Since incident particles with various energies have different ranges, the energy deposition profile obtained by an integral over the Maxwellian energy distribution may be different from that by a monochromatic beam with an average energy. If various energy carriers, such as nonthermal electrons or fast ions, are present in a target plasma, the effect of the energy distribution of incident particles or the effect of multiple energy carriers on the pellet ablation becomes more important. Indeed, the

effect of nonthermal particles such as fast ions on the pellet ablation is observed in several pellet injection into neutral beam heated plasmas. Milora has improved his model to include the fast ion heat flux in the ablation analysis (the Milora model)[8] , and also Houlberg extended the Milora model to include an energy distribution of thermal electrons by using multiple electron beams[21] , but these improved models did not take into account of the modification of ablation dynamics due to multiple energy carriers. The modification of ablation dynamics due to multiple energy carriers will be studied intensively in the following chapters.

Additional mechanisms that might further reduce the heat flux, such as dissociation, ionization, and line radiation, were investigated by Felber et al[22] . Only volume dissociation was found to be effective, which may prolong pellet lifetime by $\sim$ 10 to 20 %.

Various attempts have been made to estimate the effect of the magnetic shielding, beginning with the Rose's diamagnetic balloon model[16] , in which it is assumed that the ablation cloud instantaneously ionizes and expands like a diamagnetic balloon around the pellet. Chang considered partial trapping of the magnetic field in the cloud and analysed the corresponding flexible magnetic nozzle flow[23] . Here the abltion process is based on the ion evaporation model. It was shown in Ref.(24) that the magnetic Reynolds number of the cloud plays a role in the rate of convection of the magnetic field lines away from the pellet and their diffusion to the pellet. Using the result of Felber et al.[22] for the distribution of the degree of ionization and flow velocity in the cloud, Parks calculated the distortion of a magnetic field near a pellet by considering the above mentioned two process

(convection and diffusion of the magnetic field lines)[25]. For parameters typical in a fusion reactor, a reduction in the pellet ablation of ~10 to 30 % could be expected.

There is a different theory. Mayer applied a pellet ablation theory, which is directly related to astrophysics and laser fusion (the Cowie and McKee model), to a pellet injected into a magnetically confined plasmas[26),27)]. In this model, the evaporated ions from the pellet surface are accelerated to energies considerably in excess of the background thermal energies. He considerd this process, where thermal electron energy is converted to evaporated ion kinetic energy, as 'energy transduction'.

Recently, Kaufmann et al. investigated the additional shielding mechanism of the pellet by the high density, medium temperature plasma generated by the ablated material, which spreads along the magnetic field lines[28)]. This result supports the experimental data obtained in ASDEX[29)] and TFR[30)], where the extent of the H_α luminosity parallel to the magnetic field lines is observed. They concluded that this effect might lead to a distinct decrease in the ablation rate.

As pointed out by Lengyel[13)], existing ablation models yield acceptable results for thermal plasmas at low and intermediate temperatures, however, care should be taken in extrapolating these results to thermonuclear plasmas because of the several limitations inherent in these models.

2.3 Present status of pellet injectors

Pellets can be produced in two different ways. One is droplet source, which is produced by forming a liquid source and freezing upon evaporation of an outer layer of the droplet[1),2)]. Liquid droplets can be produced by the instability of capillary jet flow from nozzle, which is stimulated by transducer. For the pellet injection experiments in the ORMAK, which is the first injection experiment into a tokamak plasma, the droplets were used[17)]. Advantages of this pellet source are that this method can produce a spherical pellet which has small surface area compared to its volume and that multiple pellets can be produced periodically With this method, however, production of large pellets is difficult and control of the pellet size is also difficult. Therefore, this method is not taken for the present injectors.

In almost all injectors except for ORMAK, solid pellets are produced directly by heat exchange with liquid helium. Solid hydrogen is created in a condensate well, cutted, and loaded to a gun burrel. Or solid hydrogen rod is extruded, cutted, and loaded. The former type of pruduction of pellets were adopted for single pellet or four-pellets injector developed in Oak Ridge National Loboratory (ORNL) which were used for ISX-A, ISX-B, Alcator C, and other devices[2),31)]. The pellet injector for Heliotron E also belongs to this type of injector. The latter type of pellet source is suitable for continuous pellet injections since solid hydrogen for multiple pellets is created beforehand. Many of recent pellet injectors adopt this pellet source.

At present, practical pellet acceleration methods are

pneumatic (gas gun) and centrifugal acceleration. The former is the most practical method of pellet acceleration and is used widely in various pellet injectors. This acceleration method has advantages of stable operation and reliability, but it is not appropriate for multi-pellets injection. Also exhaust of propellant gas becomes a problem. Centrifugal acceleration is used for repeated injections of multiple pellets. High repetition rate and contineous fueling can be achieved by this method and this type of injector was designed to be a primary fueling device for the large, long-pulse tokamaks. Problems of centrifugal acceleration are mechanical stress of rotor and divergence of injection angle. Centrifugal pellet injectors were developed at ORNL and Max-Planck Institute of Plasma Physics (Garching) and equipped for Doublet Ⅲ [32),33)] and ASDEX[34)].

We will survey developments of pellet injectors at ORNL and Institute of Plasma Physics (Garching) First practical injector developed in ORNL was pneumatic injector with droplet sources, which was equipped for ORMAK. This injector can produce relatively small pellets of 70 μm or 210 μm in diameter and accelerate pellets at the velocity of about 100 m/s[17)]. Larger and faster pellet injection was realized by a single-pellet and four-pellets pneumatic injectors. These injectors have disks with condensate well and frozen pellets are loaded to gun barrel by rotating the disks[2),31)]. A single pellet injector was capable of injecting a single, solid hydrogen pellet nominally 1 mm in diameter at speeds in the 600 to 1000 m/s range. It was used on ISX and PDX. Four-pellets injectors were used in experiments on ISX, PDX, Alcator C, and PLT. Helium propellant gas was used in these

injectors.

Recently, a repeating pneumatic pellet injector (RPI), which uses extruded source and H_2 propellant gas, has been developed[33),35),36)]. The highest measured velocities were 1600 m/s with deuterium pellets of 4 mm in diameter and 1900 m/s with hydrogen pellets. Repetition rates as high as 6 pellets/sec for 2.5-sec bursts in hydrogen pellets and 5 pellets/sec for 4-sec bursts in deuterium pellets were obtained. This injector has already installed in TFTR and used to realize a high density plasma[37)]. The deuterium pellet injector (DPI) capable of eight-pellets pneumatic injection is being designed and fabricated for TFTR[35),38)]. The DPI is a hybrid injector using the extruder design from the RPI and an eight-burrel gun similar to that used in the four-pellet injectors. The DPI will fire up to eight cylindrical pellets (two 4.0 mm diameter by 3.5 mm length, three 3.5 mm diameter by 3.5 mm length, and three 3.0 mm diameter by 3.5 mm length) at velocities of almost 2000 m/s at a programable repetition rate. A tritium pellet injector (TPI) system has also been designed for TFTR $Q\sim1$ phase of operation[35),39)]. This has the same structure as the DPI. It utilizes eight guns and gun burrels but formation of the pellet is different from the DPI. The pellet is formed in a central magazine block and transported to the gun block using a pellet slide. The main advantage of this configuration is that it minimizes the tritium inventory ($\sim$ 3000 Ci).

A centrifuge injector equipped in Doublet Ⅲ can inject D_2 pellet of 1.3 mm diameter in equivalent sphere in every 31 or 39 ms at velocities of 800 m/s[32)]. A new version of the centrifugal

injector was designed and the construction was started[33]. The design parameters of the injector are a pellet size of 1.5 to 3.5 mm, a velocity of 1.2 km/s, and a repetition rate of 30 pellets/s for a pulse length of 30 s.

In IPP (Garching), both a pneumatic injector and a centrifugal injector have been developed, the former was installed in Wendelstein Ⅶ-A, and the latter has been installed in ASDEX[34]. Deuterium pellets with diameters of 0.6 mm and 0.8 mm and velocities of 400 to 800 m/s were injected by using the single shot pneumatic gun. By means of a centrifugal pellet injector, multi-pellets up to 80 frozen D_2 pellets of 1 mm diameter and 1.2 mm length, were injected with intervals ranging from 20 to 50 ms, and velocities of 720 m/s[34].

Alternative acceleration methods to obtain high pellet injection velocity over 10 km/s by electromagnetic rail gun, ark discharge, or CO_2 laser, are proposed and tested, but these type of injector have not yet been available[21]. Further development will be required for pellet injector appropriate to reactor plasmas.

2.4 History of pellet injection experiments

The pellet injection experiment into a tokamak plasma was initiated on ORMAK[17]. This experiment gave various informations for pellet ablation process. However, since the size of pellets was small and the injection velocity was low, the results were limited for relatively tenuous and cold edge plasmas. Pellet injection into dense and hot plasmas was performed in the ISX-A (Impurity Study Experiment)[40]. From this experiment, applicability of the neutral cloud shielding model to ablation analysis in Ohmically heated plasmas was shown. Enhancement of pellet ablation due to runaway electrons in low density discharges or fast ions in NBI heated discharges was observed in the pellet injection experiments of ISX-B[12]. After this experiment, similar enhancement of pellet ablation due to non-thermal particles have been observed in various experiments. In the ISX-B experiment, MHD activities and transport properties after the pellet injection were also studied with respect to penetration depth of the pellet. First pellet injection experiment into a divertor plasma was performed in the PDX (Poloidal Divertor Experiment). These results were reviewed by Milora.

We will review recent pellet injection experiments performed in tokamaks and stellarator/heliotron devices. Recently, in ISX-B, an increase of plasma stored energy by as much as 50 % has been observed after the pellet injection[33]. With the 1.5 mm pellet, the density increased to $n_e = 6\times10^{19}$ m^{-3} and the value of the gross energy confinement time reached to 1 7 times compared to Ohmically heated plasmas at the same density by gas puffing. The pellet

injection in ISX-B revealed better energy confinement than that in titanium getterd discharges, which is comparable to the Z-mode obtained in ungettered discharges. From ISX-B experiments, it was found that adequate pellet penetration in a target plasma with small or no MHD fluctuations before injection seems to be required to obtain confinement improvement.

The pellet fueling in Alcator C produced highly peaked density profiles and gave line-averaged densities as high as 10^{21} m^{-3} [41]. Global confinement time of the pellet-fueled plasma is found to be longer than that in similar discharges fueled by gas puffing. From the transport analysis, the ion thermal conductivity, which is typically higher than the neoclassical theory by a factor of three to five in the gas-fueled plasma in Alcator C, is found to be approximately neoclassical after pellet injection. The electron thermal conductivity is consistent with the Alcator scaling even after the pellet injection[42]. The improvement in the ion transport was considerd to be correlated with the peaking of the density profile and/or the reduction in quantity $\eta_i \equiv d(\ln T_i)/d(\ln n)$, which is inferred to lie close to the critical value for stability of the drift mode driven by the ion temperature gradient.

Continuous pellet injections performed on Ohmic, NBI, and ICRH heated discharges in ASDEX have shown that the most important parameter characterizing the discharge is the ratio of the pellet penetration depth, Δ, to the fall-off length for neutral particles in a gas fueled case (typically 5 to 8 cm in ASDEX)[34]. For shallow penetration, only minor difference compared to gas fueled discharges, was obserbed. In contrast, for deep penetration (e.g. $\Delta \geq a/2$) the density profile was more peaked and the temperature

profile was more flattened at the same line-averaged density. Ohmic discharges with deep pellet penetration reach to the higher density limit and are maintained by a low particle supply rate than that in gas fueled discharges. The peaked profiles accompanied with a slightly non-adiabatic pressure evolution, however, lead to degradation of energy confinement in ASDEX, which may be caused by the enhanced convection and radiation. Even in ASDEX, however, recent data indicated improvement of the confinement time[43]. It is concluded that the pellet injection is able to change the confinement properties of tokamak discharge fundamentally. The confinement improvement is possible with pellet injection penetrating within the half-radius.

Preliminary results was obtained by injecting 1.5 mm diameter D_2 pellets into Ohmically heated discharges and low-power (about 600 kW) ICRF heated discharges in PLT[33]. In the Ohmic discharge, the post-pellet T_e profile was slightly flatter than the pre-pellet profile and the sawtooth inversion radius increased slightly. The sawtooth period also increased 1.5 times. Neutron production increased threefold after the pellet injection. Like the line-averaged density, neutron production continued at elevated rate for the duration of the discharge, indicating good confinement of the particles deposited by the pellet. In ICRF heated plasmas, both neutron production and T_e increase steadily after the pellet injection as long as the ICRF power continues. A promising indication of the improved ICRF heating by the pellet injection was seen.

A centrifugal injector that repetitively injects 1.3-mm deuterium pellets at a rate of 32 pellets per second was used to

build up and maintain the density at a line-averaged value of 1×10^{20} m^{-3} in the 2.4 MW-NBI heated limiter discharge of Doublet Ⅲ [32),44)]. So far as a pellet penetrates deeply into the plasma (more than 30 cm), the energy confinement time is improved in beam-heated limiter discharges associated with a peaked density profile and low edge recycling. The energy confinement time is improved 1.7 times, compared to that of similar gas fueled discharges with 2.4 MW of NBI. This value is comparable to that of Doublet Ⅲ H-mode discharges with similar plasma current. A centrally peaked density profile (peak-to-average ratio about 2.0) is maintained for a considerable time by the continuous pellet injection. Coupled with the improved confinement, this discharge gave a higher neutron production rate (more than ten times higher than that of similar gas-fueled discharges). Keeping the deep pellet penetration is important, especially in high power NBI. It was found that the pellet penetration is improved by the neutral beam interruption before the pellet injection. Therefore, a synchronized beam interruption has been employed to maintain the good energy confinement time in the high power NBI heated plasma in Doublet Ⅲ .

Central density above 1.6×10^{20} m^{-3} has bee produced in TFTR by the injection of 4 mm deuterium pellet[37)]. Injection of multiple 2.67 mm pellets produces hollow density profiles which relax within 20 to 100 ms. When the neutral beam injection started after the pellet injection, a rapid recovery of temperature was observed, and sawtooth oscillations were supressed. Global confinement time is between 200 and 250 ms, comparable to that obtained by gas fueling. Confinement in the central region is appreciably improved. The best

result was obtained in Ohmic plasmas with a=0.7 m, R=2.35 m, I_p=1.6 MA by optimizing the pellet penetration, the pellet size, and velocity (diameter is 2.67 mm and velocity is 1250 m/s)[45]. Sequences of up to 5 such pellets have been injected and the central density has reached to 4×10^{20} m^{-3} immediately after injection. The density profiles in these discharges are highly peaked. The density decays with a time constant of approximately one second, and keeps a peaked profile. At the peak of the stored energy, the energy confinement time was 0.53± 0.05 sec and $n_e(0)\tau_E(a)$ was $1.5\pm0.3\times10^{20}$ m^{-3} s, which is nearly double the previous best result in Alcator C, with central electron temperature of 1.3 keV. The global energy confinement in these discharges is better than that in deuterium or helium gas fueled discharges, in which the confinememt time appears to saturate at $\tau_E\sim$300 ms in the region of line-averaged densities above 4.5×10^{19} m^{-3} .

Experiments of pellet injection has been performed not only in tokamaks as described above but also in stellarator/heliotron devices such as Wendelstein Ⅶ-A and Heliotron E[74]. Deuterium pellets with diameters of 0.6 mm and 0.8 mm and velocities of 400 to 800 m/s were injected into ECR and NBI heated plasmas of Wendelstein Ⅶ-A[71]. In ECRH plasmas, only 30 to 50 % of pellet particles was confined. It was mentioned that ablation near the edge of the plasma by fast electrons produced by ECRH could be a possible explanation of this reduction. In NBI heated plasmas, it was indicated that fast ions directly contribute to the ablation of the pellet. With pellet injection, a fast density rise can be produced without increasing the impurity level simultaneously.

In NBI heated current-free plasmas in Heliotron E, the increase of line-averaged density after the pellet injection up to 8.2×10^{19} m^{-3} was observed, which corresponds approximately to the confinement of total particles of the pellet[46]. The highest density of $\bar{n}_e=1.35\times10^{20}$ m^{-3} was achieved by the pellet injection. The apparent density decay time after pellet injection is longer than 50 ms in the case with magnetic field strength of 1.9 T. In most cases with 0.94 T, it is less than 10 ms. This has been considered to be related to radiation loss and breakdown of the power balance.

2.5 Applications to diagonostics

Vasin et al. have used impurity pellets, for example carbon pellets, to measure the effective charge, Z_{eff}, profile, where $Z_{eff}=\sum n_j Z_j^2/\sum n_j Z_j$ and n_j and Z_j are the density and charge of the ion specie j[47]. To determine the effective charge, they made use of the circumstance that the intensity of the continuum emmision, I_c, is proportional to Z_{eff} and is related to the plasma density and temperature. They showed an expression for the effective charge which requires only relative measurements of I_c, T_e, and n_e.

Andersen used a small pellets of frozen deuterium to study the profile of runaway electrons in plasma[48]. He paied attention to the toridal deflection of pellet orbit due to runaway electrons which give an asymmetrical ablation of the pellet. He calculated the necessary fast electron flux responsible for this deflection and obtained a fast electron flux profile.

Heidbrink discusses diagnostic applications of fast neutron measurements during pellet injection on TFTR[49]. At first, application of pellet injection to the problem of extrapolating the neutron measurement in a deuterium plasma to the fusion production in an equivalent deuterium-tritium plasma was discussed. Next, an application to measurement of the radial profiles of energetic beam ions was also considered. Finally, it was shown that, during wave heating, the "temperature" of the deuterium tail can be inferred from neutron flux measurements alone.

Sasao et al. have proposed diagnostics of confined alpha-particles by pellet injection[50]. The alpha-particle density can be obtained from the number of decaying photons emitted from

He^{+*} ($n \geq 2$) ions which are producd through the one-electron transfer reaction of an alpha-particle with the probing ion ablated from the pellet before it is fully ionized. The counting rate estimated by using theoretical cross sections and the calculated pellet ablation rate is sufficient to be observed under the bremmstrahlung background. The alpha-particle velocity distribution will be also obtained from the Doppler broadening of the spectral lines.

CHAPTER 3

A Pellet Ablation Model Including Multiple Energy Carriers in Shielding Cloud

3.1 Introduction

Enhancements of pellet ablation during the neutral beam injections (NBI) heating were observed in many pellet injection experiments performed in tokamaks or helical devices as discussed in chapter 2. In the experiments of ISX-B, for example, penetration length of the pellet injected into the plasma without NBI was compared with that 3 msec after the beginning of NBI[12]. Although plasma densities and temperatures were almost the same for both experiments, it was shown that the latter penetration was substantially shallower. It could be considered naturally that fast ions produced in the plasma due to NBI would contribute the ablation of the pellet. In RF heated plasmas or runaway plasmas, similarly, non-thermal component of electrons or ions will contribute the ablation of the pellet.

Pellet ablation calculations done by the Parks and Turnbull model (PT model)[6] or the Milora and Foster model (MF model)[19], which are based on the neutral cloud shilding model including incident heat flux of thermal electrons to pellet surface only, agreed well with experiments in Ohmically heated plasmas except for the case of runaway or slide-away discharges. Usually in NBI heated plasmas, there appeared discripancies between the experiments and the calculations based on the PT or the MF model. First attempt to

include the effect of fast ions in ablation model was performed by Milora[8], which was applied to the pellet injection experiments in PDX and DoubleⅢ tokamaks. He used a scaling relation between an average heating power and a column integrated density of a neutral shielding cloud, which is obtained from a numerical solution of the fluid equations based on the neutral cloud shielding model including thermal electron only (MF model). A summation of heat fluxes both due to electrons and fast ions is interpreted as an average heating power in the cloud surrounding the pellet. This model has an advantage that pellet ablation rate is calculated rather simply even though the effect of fast ions is included. On the other hand, the assumption seems crude. At first, although heat fluxes due to charged particles with different range, such as thermal electrons and fast ions, exist in the cloud, it is assumed that the structure of the cloud is the same as the case taking into account of electrons alone. And the average heating power is used in the calculation of the cloud density by neglecting the spatial profile of the both heat fluxes. Moreover, as pointed by Lengyel, energy distribution of incident particles might affect the structure of the cloud and ablation rate, even though it takes a Maxwellian[13].

In order to study the structure of the ablation cloud surrounding the pellet and the ablation rate in the case that multiple energy carriers exist in the cloud, we develop a new ablation model which is applicable to the case of multiple energy carriers. Since our model is based on the PT model, by neglecting the additional heat source term and the equations to determine this heat source, the original PT model can be recovered.

3.2 Description of the model

Based on the neutral cloud shielding model introduced in chapter 2, we describe the model equations for the shielding cloud or ablation cloud surrounding the pellet.

An ablation cloud, which is composed of neutrals surrounding the pellet and regarded as an ideal gas, shields or absorbs heat fluxes from the background plasma to the pellet surface. The heated cloud is assumed to expand spherically and form transonic flow. In our model, multiple energy carriers are taken into account in the incident heat fluxes to the pellet. For simplicity, the approximation is invoked that each energy carrier has a monochromatic energy. When incident particles have an energy distribution, this energy distribution can be taken into account by dividing it into several energy carriers with different monochromatic energies. In the PT model, incident thermal electrons are treated as a single energy carrier with energy of $2T_e$, where T_e is the electron temperature. If the ablation energy on the pellet is as low as the sublimation energy, only a small amount of incident heat flux to the pellet surface is required to maintain the necessary neutral density to attenuate the heat flux sufficiently. Thus, the total heat flux at the pellet surface, q_p, is considered to be much less than the total heat flux from the exterior plasma, q_∞;

$$q_p \ll q_\infty \ . \tag{3.1}$$

In the above situation, ablation process of the pellet is self-regulated by the surrounding neutrals. For example, if the

ablation rate on the pellet surface is suddenly enhanced, this is accompanied by an increase in the neutral density in the cloud, which decreases q_p through the enhanced shielding effect of the cloud. Therefore, the increase in the ablation rate is supressed by the decrease in q_p. On the other hand, when a perturbation reduces the ablation rate on the pellet surface, q_p is increased to maintain the stationary value of the neutral density. From the considerations, we see that the ablation rate of the pellet is directly related to the shielding mechanism of the neutral cloud.

Since characteristic time of the flow of the ablated neutrals is usually much shorter than the characteristic times of the motion of the injected pellet itself, of the change in the macroscopic plasma parameters and of the recession of the pellet radius, the profile of the neutral cloud will rapidly become quasi-stationary. In the description of the ablation cloud, therefore, the pellet radius and the plasma parameters are assumed to be time independent.

By assuming that the cloud expands spherically, the conservation laws for mass, momentum, and energy in the cloud and the equation of state for the cloud as an ideal gas are written as follows;

$$\rho v r^2 = \frac{G}{4\pi} = \text{const.}, \tag{3.2}$$

$$\rho v \frac{dv}{dr} + \frac{dp}{dr} = 0 , \tag{3.3}$$

$$\rho v \frac{d}{dr}\left(\frac{\gamma e T}{(\gamma-1)m} + \frac{v^2}{2}\right) = e\rho \sum_j W_j , \tag{3.4}$$

$$p = \frac{\rho e T}{m} \quad . \tag{3.5}$$

Where m, ρ, v, p represent the average molecular mass, the mass density, the fluid velocity, and the pressure of the cloud, respectively. The temperature of the cloud, T, is measured in unit of eV (e=1.602×10^{-19}Joule/eV), and r is radial distance from the center of the spherical pellet, γ is the ratio of specific heats, and G denotes the ablation rate in kg/sec. In Eq.(3.4), W_j means the heat source in the cloud due to respective energy carrier and is expressed by the heat flux q_j and ρ as

$$W_j = \frac{f_{Bj}}{\rho} \frac{dq_j}{dr} \qquad (\mathrm{eV/kg \cdot sec}) \quad , \tag{3.6}$$

in the slab approximation. If the bulk of the cloud, where heat flux attenuation is substantial, does not extend far from the pellet surface, this approximation will be reasonable. Here, f_{Bj} designates the fraction of the heat flux due to different energy carrier, which is deposited for net heating of the cloud. The value of f_{Bj} is determined by including the effects of atomic process and of geometry for the incident flux.

Equations (3.2) to (3.5) describe a free spherical expansion of a neutral gas with volumetric heat source. Without volumetric heat source, the flow velocity, v, coincides with the local sound velocity, $C_s=\sqrt{\gamma e T_*/m}$, at the pellet surface, and the Mach number, $M=v/C_s$, gradually increases as going far away from the pellet surface and approaches the asymptotic value, $\sqrt{5/\gamma}$, corresponding to the supersonic flow[19]. With a strong heat source near the pellet surface, the Mach number decreases and becomes less than unity at the pellet surface. Since the value of M will approach $\sqrt{5/\gamma}$ far

from the pellet surface where the heat source becomes negligible, M coincides unity at a certain point, where the transition of the subsonic flow to the supersonic flow occers like in the Laval nozzle. Such a flow is called the transonic flow. At this sonic transition point, $r=r_*$, which is called a sonic radius, a constraint comes out to avoid a singularity. In order to be suitable for numerical calculations, physical quantities are normalized by the values at the sonic radius. From Eqs.(3.2) and (3.5),

$$\rho' = \frac{1}{v' r'^2} \tag{3.7}$$

and

$$p' = \frac{T'}{v' r'^2} \tag{3.8}$$

is obtained. Here the primes denote the normalized quantities. Using the relations (3.7) and (3.8), the momentum equation (3.3) is rewritten as

$$\frac{dT'}{dr'} = \left(\frac{T'}{v'} - \gamma v'\right)\frac{dv'}{dr'} + \frac{2T'}{r'} \ . \tag{3.9}$$

The energy equation (3.4) becomes

$$\frac{dv'}{dr'} = \frac{1}{(1-\gamma)v'}\frac{dT'}{dr'} + \frac{e r_* W_*}{v_*^3}\frac{W'}{v'^2} \tag{3.10}$$

by using Eq.(3.7). Where asteriscs designate values at $r=r_*$, and

$$W_* \equiv \sum_j W_{j*}$$

$$W' \equiv \sum_j W_j / W_* \ .$$

By substituting Eq.(3.9) into Eq.(3.10),

$$\frac{dv'}{dr'} = \frac{1}{T'-v'^2}\left[\frac{er_*W_*}{v_*^3}(\gamma-1)W' - \frac{2T'v'}{r'}\right] \qquad (3.11)$$

is obtained. Since the ablation cloud is continuously accelerated, dv'/dr' should be a continuous function of r'. To avoid the singularity at the sonic radius, therefore, a relation,

$$v_*^3 = e(\gamma-1)r_*W_*/2 \ , \qquad (3.12)$$

is required.

By using Eq.(3.12), differential equations in the normalized form (3.11) and (3.10) become

$$\frac{dv'}{dr'} = \frac{2}{\Theta'^2-v'^2}\left(W' - \frac{\Theta'^2v'}{r'}\right) \ , \qquad (3.13)$$

$$\frac{d\Theta'}{dr'} = \frac{W'}{v'\Theta'} + \frac{(1-\gamma)v'}{2\Theta'}\frac{dv'}{dr'} \ , \qquad (3.14)$$

where $\Theta' \equiv T'^{1/2}$.

In order to determine the heat source in the cloud W_j, which is expressed as Eq.(3.6), a relation for attenuation of the heat flux must be given for each energy carrier. We use following expressions to describe the attenuation of the heat flux ;

$$\frac{dE_j}{dr} = \frac{\rho L_j(E_j)}{m} \ , \qquad (3.15)$$

$$\frac{dq_j}{dr} = \frac{\rho \Lambda_j(E_j)q_j}{m} \ , \qquad (3.16)$$

where E_j is the energy, L_j is the energy loss function and Λ_j is the effective cross section of heat flux loss for the respective energy carrier in the cloud. These equations can be written

$$\frac{dE_j'}{dr'} = g_j(\lambda_*, E_{j*})\rho' L_j' \ , \qquad (3.17)$$

$$\frac{dq_j'}{dr'} = h_j(\lambda_*, E_{j*})\rho' \Lambda_j' q_j' \quad , \tag{3.18}$$

in the normalized forms by values at the sonic radius. Here dimensionless parameters g_j and h_j are functions of

$$\lambda_* \equiv \rho_* r_* / m \tag{3.19}$$

and if we define $L_{j*} \equiv L_j(E_{j*})$ and $\Lambda_{j*} \equiv \Lambda_j(E_{j*})$, these are expressed as

$$g_j \equiv \lambda_* L_{j*} / E_{j*} \quad , \tag{3.20}$$

$$h_j \equiv \lambda_* \Lambda_{j*} \quad . \tag{3.21}$$

In Eqs.(3.17) and (3.18), g_j and h_j or λ_* and E_{j*} are unknown parameters and they must be determined from boundary conditions. Integrating Eq.(3.15) from $r'=1$ to $r'=\infty$, we obtain

$$\int_{E_{j*}}^{E_{j\infty}} dE_j / L_j = \chi \quad , \tag{3.22}$$

where

$$\chi \equiv \lambda_* \int_1^\infty \rho' dr' \quad .$$

When the energies in background plasma $E_{j\infty}$ is given, the energy at the sonic radius E_{j*} can be obtained from χ through Eq.(3.22). If E_{j*} is found uniquely in the range $(0, E_{j\infty})$, the parameters g_j and h_j are also determined by χ through E_{j*} . When it is failed to find the root of E_{j*} in $(0, E_{j\infty})$, it means that the respective energy carrier will not reach the sonic radius. In the neutral cloud shieding model, the shielding effect due to the ablation cloud is assumed to be dominant in the subsonic region near the pellet surface. If the cloud structure in the supersonic region would give the dominant contribution for the pellet ablation, the neutral

cloud shielding model becomes questionable. This is because the ionization degree of the ablation cloud in the supersonic region will be considerably high and it cannot be assumed to be neutral. In such a case, the effect of the magnetic shielding may become important[1),2)]. Here we consider the case that the neutral cloud shielding model is valid and assume the energy carrier which cannot reach the sonic radius does not contribute to the ablation process.

In the same way as for E_{j*}, q_{j*} will be obtained from Eq.(3.16). Since the cloud density is low and the attenuation of the incident energy is small in the supersonic region generally, we assume $\Lambda(E_j)$ in Eq.(3.16) to be uniform in space and set $\Lambda[(E_{j*}+E_{j\infty})/2]$ to obtain q_{j*} approximately. Then

$$q_{j*} \simeq q_{j\infty}\exp\left[-\chi\Lambda[(E_{j*}+E_{j\infty})/2]\right] \tag{3.23}$$

is obtained from Eq.(3.16). Here q_{j*} is not directly related to the attenuation of the incident heat flux of Eqs.(3.17) and (3.18) but it is used to determine W' in (3.13) and (3.14) through (3.6). From (3.6) and (3.16), the heat source at the sonic radius, W_* is given by

$$W_* = \sum_j \frac{f_{Bj}q_{j*}\Lambda_{j*}}{m}. \tag{3.24}$$

By using W_*, the normalized heat source is written as

$$W' = \sum_j \xi_j q_j' \Lambda_j' \ , \tag{3.25}$$

where

$$\xi_j \equiv \left[\frac{f_{Bj}q_{j*}\Lambda_{j*}}{m}\right]/W_* \tag{3.26}$$

is regarded as a function of χ through q_{j*} and E_{j*} like g_j and h_j.

The equations for the cloud in normalized forms are summarized as

$$\frac{dv'}{dr'} = \frac{2}{\Theta'^2 - v'^2}\left(\sum_j \xi_j(\chi) q_j' \Lambda_j' - \frac{\Theta'^2 v'}{r'}\right) , \tag{3.27}$$

$$\frac{d\Theta'}{dr'} = \frac{\sum_j \xi_j(\chi) q_j' \Lambda_j'}{v'\Theta'} + \frac{(1-\gamma) v'}{2\Theta'} \frac{dv'}{dr'} , \tag{3.28}$$

$$\frac{dE_j'}{dr'} = g_j(\chi, \lambda_*) \frac{L_j'}{r'^2 v'} , \tag{3.29}$$

$$\frac{dq_j'}{dr'} = h_j(\chi, \lambda_*) \frac{q_j' \Lambda_j'}{r'^2 v'} . \tag{3.30}$$

Accompanied by the expressions for ξ_j, g_j, h_j, L_j and Λ_j, these equations are closed. When the parameters χ and λ_* are given, ξ_j, g_j and h_j are determined. Then, the normalized equations for the cloud are able to be solved. The parameters χ and λ_* must be determined to satisfy the boundary conditions.

To solve the normalized cloud equations we must determine the starting value of dv'/dr' at $r'=1$, since dv'/dr' has the improper form of 0/0 at $r'=1$ in Eq.(3.13). If we define $Z \equiv dv'/dr'|_{r'=1}$ and $D \equiv dW'/dr'|_{r'=1}$ for simplicity, the relation of Z and D,

$$D = -\tfrac{1}{2}(1+\gamma)Z^2 + (3-\gamma)Z + 1 , \tag{3.31}$$

is obtained by Eqs.(3.13), (3.14) and L'Hospital's theorem. Since the Mach number, $M \equiv v'/\Theta'$, is less than unity in the subsonic region, the inequality, $Z > d\Theta'/dr'|_{r'=1}$, must be satisfied. This inequality and Eq.(3.14) give a lower bound of Z ;

$$Z_{lb} = 2/(1+\gamma) . \tag{3.32}$$

If $D > 0$, it follows from Eq.(3.31) that the upper bound of Z is

given by

$$Z_{ub} = \left(\frac{3-\gamma}{1+\gamma}\right)\left(1+\sqrt{1+2(1+\gamma)/(3-\gamma)^2}\right). \tag{3.33}$$

The range of Z or D, therefore, is as follows :

$$\begin{cases} Z_{lb} < Z < Z_{ub} \\ \dfrac{5-\gamma}{1+\gamma} > D > 0 \end{cases}. \tag{3.34}$$

Since the range of Z is limited like this, the value of Z is determined uniquely from D with Eq.(3.31) in spite that it has a quadratic form of Z ;

$$Z = \left(\frac{3-\gamma}{1+\gamma}\right)\left(1+\sqrt{1+2(1+\gamma)(D-1)/(3-\gamma)^2}\right). \tag{3.35}$$

From the expression of W', Eq.(3.25), and

$$\frac{d\Lambda_j'}{dr'}\Big|_{r'=1} = \left(\frac{E_{j*}}{\Lambda_{j*}}\right)\frac{d\Lambda_j}{dE_j}\Big|_{E_j=E_{j*}}\frac{dE_j'}{dr'}\Big|_{r'=1},$$

D is written as

$$D = \sum_j \xi_j(\Lambda_{j*}+N_{j*})\lambda_* \ , \tag{3.36}$$

$$N_{j*} \equiv \left(\frac{L_{j*}}{\Lambda_{j*}}\right)\frac{d\Lambda_j}{dE_j}\Big|_{E_j=E_{j*}} \ . \tag{3.37}$$

If λ_* and χ are given, E_{j*} and D can be calculated. Afterward Z is obtained from Eq.(3.35). It must bear in mind that λ_* should be given in the range

$$0 < \lambda_* < \left(\frac{5-\gamma}{1+\gamma}\right)\left(\frac{1}{\Sigma\xi_j(\Lambda_{j*}+N_{j*})}\right) \tag{3.38}$$

from Eq.(3.34). It is also remarked, since D, Z and λ_* are mutually related, each of these can be used as a shooting parameter to find the solution.

Next we consider the boundary conditions at the pellet surface. At first, the relation which must be satisfied at the pellet surface is the energy conservation. As mentioned in Chapter 2, the bulk of the incident energy to the pellet surface is deposited as heat and this is used to sustain the surface temperature at nearly equal to triple-point temperature in the phase diagram against the cooling due to evapolation of molecular hydrogen gas. Therefore, the incident energy to the pellet surface must balance the ablation energy in steady state. The energy conservation at the pellet surface is expressed as

$$-4\pi r_p^2 \lambda n_s \frac{dr_p}{dt} = \sum_j A_j q_j \qquad (3.39)$$

where λ is the ablation energy per molecule of the pellet and n_s is molecular density of the pellet. In the neutral cloud shielding model, the ablation energy λ is considered to be equal to the sublimation energy at the triple-point temperature. For H_2-pellet, λ= 0.01 eV/mol. A_j is the effective cross-section of the pellet for the respective energy carrier. If the energy flux incidents along the magnetic field line, A_j is about $2\pi r_p^2$. And if it incidents isotropically to the pellet surface, $A_j \sim 4\pi r_p^2$. Similarly, mass conservation at the surface is written as

$$-4\pi r_p^2 m n_s \frac{dr_p}{dt} = G$$

$$= 4\pi r_*^2 \rho_* v_* \ . \qquad (3.40)$$

from (3.2). Combining Eqs.(3.39) and (3.40),

$$\sum_j A_j q_j = 4\pi \lambda \lambda_* v_* r_* \qquad (3.41)$$

must hold at the pellet surface, where we use the definition of λ_*, (3.19). Since the surface temperature of the pellet is nearly equal to the triple-point temperature, T_t, the cloud temperature on the pellet surface is approximated to this temperature ;

$$T = T_t \qquad at \ r=r_p. \tag{3.42}$$

Thus, the boundary conditions (3.41) and (3.42) must be satisfied simultaneously at the pellet surface. Physical data for hydrogen isotopes are shown in Table 3-I[1]. For example, triple-point temperature of H_2-pellet is 13.9K. Typically, this temperature which corresponds to 1.2×10^{-3} eV is much smaller than that at the sonic radius ($\sim$1 eV).

An algorithm to solve the cloud equations are shown in Fig.3.1. The four differential equations, (3.27) $\sim$ (3.30), associated with boundary conditions are solved numerically from the sonic radius, $r'=1$, to the pellet surface, $r'<1$. At first, χ is fixed and the solutions, which satisfy the boundary conditions at the pellet surface (3.41) and (3.42), are searched for the shooting parameter λ_*. This is equivalent to that an eigenvalue problem with eigenvalue λ_* is solved with the shooting method. After the eigenvalue λ_* satisfying the boundary conditions at the pellet surface is obtained, the cloud equations are solved in the supersonic region, $r'>1$, by using the same values of χ and λ_* as those for $r'<1$ and an asymptotic value of E_j' at $r'\to\infty$, $\tilde{E}_j'$, is calculated. Here it is checked whether this value coincides with the value of $E_{j\infty}/E_{j*}$ calulated from χ with Eq.(3.22) or not. If there is a difference between these values, the expected value of χ is changed and the above procedure is repeated from the beginning.

By this algorithm, the value of χ is obtained to satisfy the boundary condition at $r' \to \infty$. In this way, the eigenvalue and eigen-functions satisfying the boundary conditions at both $r=r_p$ and $r \to \infty$ can be obtained.

By these procedures, normilized solutions and the eigenvalue λ_* and χ can be obtained numerically. When plasma parameters in the background plasma and pellet radius r_p are given, following quantities are calculated ;

$$r_* = r_p/\hat{r}_p \tag{3.43}$$

$$\rho_* = m\lambda_*/r_* \tag{3.44}$$

$$v_* = [e(\gamma-1)r_*W_*/2]^{1/3} \ . \tag{3.45}$$

Here $\hat{r}_p$ is the normalized pellet radius where boundary conditions (3.41) and (3.42) are satisfied. In Eq.(3.45), W_* is calculated from Eq.(3.24). Accordingly, physical quantities in the ablation cloud are derived from the normalized solutions and thier values at the sonic radius. Ablation rate of the pellet is caluculated from the mass conservation law (3.40) by using the values of ρ_*, v_* and r_*.

Table.3-I. Physical data for hydrogen isotopes.

	H	D	T
Boiling point at 1 atm	20.4 K (1.76×10^{-3} eV)	23.7 K (2.04×10^{-3} eV)	25.0 K (2.15×10^{-3} eV)
Triple-point temperature	13.9 K (1.20×10^{-3} eV)	18.7 K (1.61×10^{-3} eV)	20.6 K (1.78×10^{-3} eV)
Density (kg/m^3)	88.3	200	324
Heat of sublimation at triple-point (eV/atom)	0.005	0.008	-----

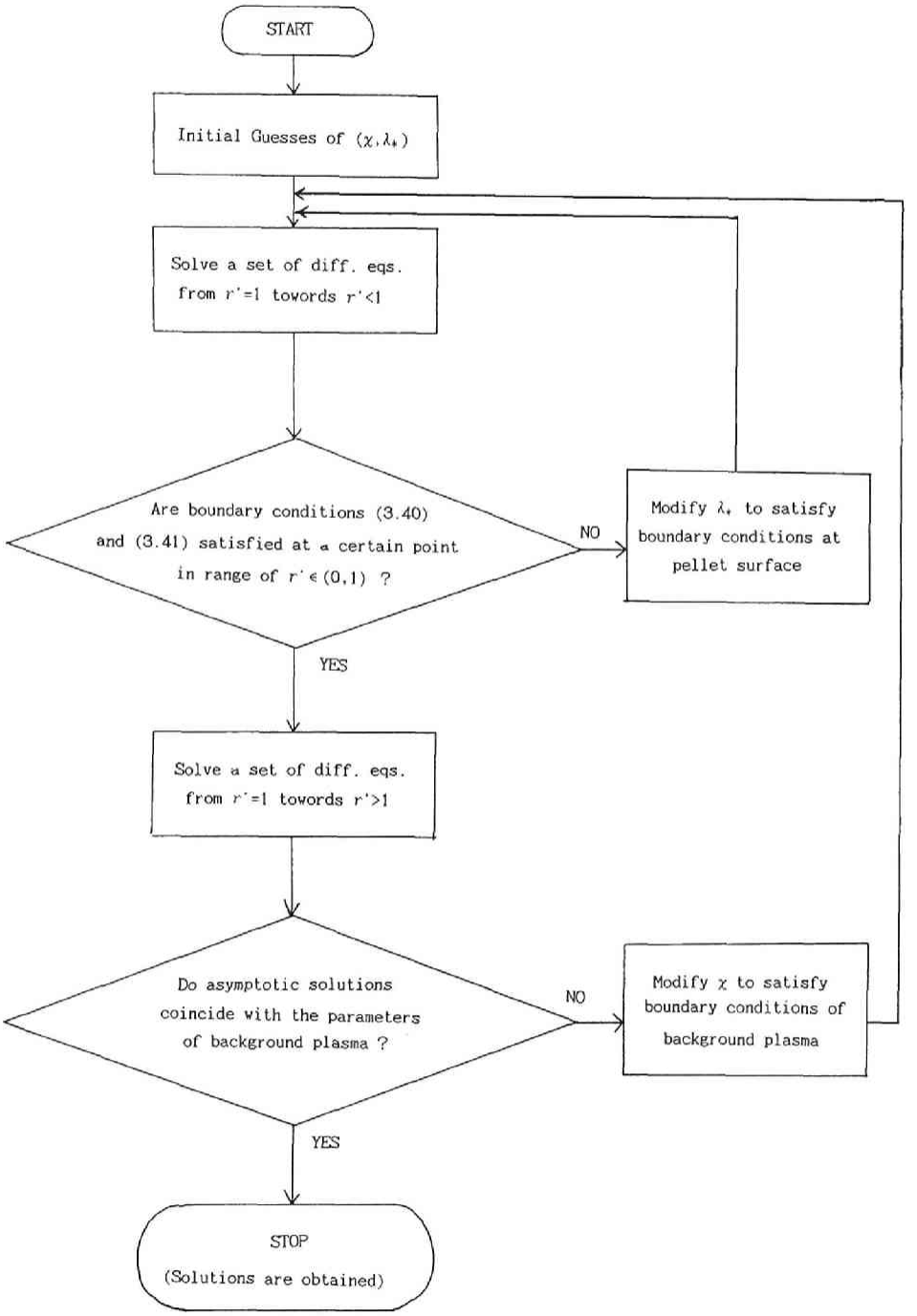

Fig.3.1. Algorithm to solve a set of cloud equations.

CHAPTER 4

Applications of the Present Model

4.1 Introduction

In this chapter, we apply our model described in the previous chapter to (1) the case including energy carriers both of thermal electrons and fast ions[7] and (2) the case including energy carriers both of thermal electrons and non-thermal electrons. The former case correspends to the pellet ablation in NBI or ICRF heated plasmas and the latter case corresponds to that in ECH or runaway plasmas. Although our model will be able to take into account for the energy distribution of incident particles principally, it will use much computational time to obtain an ablation rate profile. Therefore, for simplicity, we assume that each incident flux of thermal electrons, fast ions or non-thermal electrons can be treated as an energy carrier with monochromatic energy, even though it has an energy distribution.

4.2 Effects of fast ions on pellet ablation

We consider the case including two energy carriers of thermal electrons and fast ions[7] . In the following subscript e denotes thermal electrons and f does fast ions. For thermal electrons, the representative energy E_e and heat flux to the pellet q_e are given by

$$E_e = 2T_e \qquad \text{(eV)} \ , \tag{4.1}$$

$$q_e = \Gamma_e E_e$$

$$= G_e n_e E_e^{3/2} \qquad \text{(eV/m}^2\text{sec)} \ , \tag{4.2}$$

where

$$\Gamma_e \equiv G_e n_e E_e^{1/2} \ ,$$

$$G_e = \frac{1}{2}\sqrt{\frac{e}{\pi m_e}} \ ,$$

and Γ_e denotes the electron particle flux. The energy loss function for the electrons in the cloud, $L_e(E_e)$, is given by a semi-empirical form[19] ,

$$L_e(E_e) = (2.35\times10^{18} + 4\times10^{15}E_e + 2\times10^{21}E_e^{-2})^{-1} \ . \tag{4.3}$$

Here the loss function has a unit of eV-m^2 . In the low electron energy regime, decrement of the incident electron density due to elastic collisions affects the attenuation of the electron heat flux. By using the total cross-section for the elastic backscattering, $\hat{\sigma}_T$, the decrease of the incident electron density n_e is written as

$$\frac{dn_e}{dr} = \frac{\rho n_e \hat{\sigma}_T(E_e)}{m} \ , \tag{4.4}$$

where $\hat{\sigma}_T$ is given as a function of electron energy by Parks et

al.[5]

$$\hat{\sigma}_T = \begin{cases} 1.13\times10^{-18}E_e^{-1} & for\ E_e<100\text{eV} \\ 8.8\times10^{-17}E_e^{-1.71}-1.62\times10^{-16}E_e^{-1.932} & for\ E_e\geqq100\text{eV}, \end{cases} \tag{4.5}$$

in m^2. From Eqs.(3.15),(3.16) and (4.2), the attenuation of the electron heat flux in the ablation cloud is written as

$$\frac{dq_e}{dr} = \frac{\rho}{m}\left(\hat{\sigma}_T + \frac{3L_e}{2E_e}\right)q_e$$

$$= \frac{\rho}{m}\Lambda_e(E_e)\,q_e \ , \tag{4.6}$$

where $\Lambda_e(E_e)\equiv\hat{\sigma}_T+3L_e/2E_e$ means effective cross section for the attenuation of the electron heat flux.

The energy flux of the incident fast ions q_f is assumed as the same form as for the electrons

$$q_f = G_f n_f E_f^{3/2} \tag{4.7}$$

where G_f is a numerical factor derived from the moment calculation of the fast ion distribution function ; its value depends on the distribution function. E_f and n_f are the representative energy and the density of the incident fast ions, respectively. The energy loss function for the incident fast ions $L_f(E_f)$ is given by[8]

$$L_f(E_f) = 1.93\times10^{-20}E_f^{0.4}\ (\text{eV-m}^2) \ . \tag{4.8}$$

For fast ions, decrement of the fast ion density due to the elestic backscattering may be negligible. Therefore, the attenuation of the heat flux for the fast ions is written as

$$\frac{dq_f}{dr} = \frac{\rho\Lambda_f(E_f)\,q_f}{m} \ , \tag{4.9}$$

where $\Lambda_f(E_f)\equiv3L_f(E_f)/2E_f$ becomes effective cross section for the fast ion heat flux loss in the shielding cloud.

As mentioned in section 3.1, total heat flux at the pellet surface q_p is considered to be much less than that at the sonic radius, since the ablation energy of the pellet is very small and the attenuation of the heat flux is substantial in the subsonic region. Moreover, the cloud temperature on the pellet surface is much lower than that at the sonic radius. When the ablation process is self-regulated by the shielding mechanism, ablation rate is determined by the cloud structure. Therefore, the values of the normalized cloud temperature T' and total heat flux q' on the pellet surface are much less than unity and are not important to the cloud structure or the ablation rate. We assume for simplicity that the boundary conditions at the pellet surface are

$$q' \sim 0 \tag{4.10}$$

$$v' \sim 0 \tag{4.11}$$

instead of (3.41) and (3.42). These are also assumed in PT model[6] . Since Mach number $M=v'/\Theta'$ is less than unity in the subsonic region, the boundary condition (4.11) is equivalent to $\Theta' \sim 0$.

We use D defined by (3.31) as a shooting parameter. Since only two energy carriers are included, we does not use parameter χ (see (3.22)) and directly find E_{e*} , E_{f*} and ξ_e ($\xi_f=1-\xi_e$; see (3.26)), whose asympotic solutions at $r' \to \infty$ coincide with given plasma parameters, by the iterative procedure. Here ξ_e is related to the ratio between the incident heat fluxes at the sonic radius, β, by

$$\beta \equiv q_{f*}/q_{e*} = \frac{f_{Be}\Lambda_{e*}\xi_f}{f_{Bf}\Lambda_{f*}\xi_e} \tag{4.12}$$

from (3.26). For the sake of simplicity, it is assumed that fractions f_{Be} and f_{Bf} are uniform in the cloud, and $f_{Be} \sim 0.6$, $f_{Bf} \sim 1.0$. The former value has been estimated by considering that

the incident electrons move almost along the magnetic field lines to the pellet and that their Larmor radii are tipically smaller than the pellet radius r_p [6] . The latter has been adopted by assuming that the Larmor radii of the fast ions will be larger than the pellet radius and that the cloud is heated isotropically.

Typical results of numerical calculations are shown in Table 4-I and Fig.4.1 for three cases; (a) incident heat flux of only electrons is included, (b) incident heat flux of only fast ions is included, (c) incident heat fluxes of both electrons and fast ions are included. These calculations are performed for the same ambient plasma parameters ($n_{e\infty}=6\times10^{19}\mathrm{m}^{-3}$, $T_{e\infty}=200\mathrm{eV}$, $n_{f\infty}=2\times10^{18}\mathrm{m}^{-3}$, $E_{f\infty}=25.53\mathrm{keV}$, and $q_{f\infty}=1.44\times10^{28}\mathrm{eV/m^2sec}$) and pellet size ($r_p=0.5\mathrm{mm}$) in which the effect of the heat flux due to fast ions is significant.

First, we compare (a) with (b). The case of (a) exactly corresponds to PT model and the heat flux of the fast ions is neglected ($\xi_e=1$). For this case, electron energy at the sonic radius, E_{e*}, is required to obtain the normalized solutions. On the other hand, in the case of (b) the heat flux of the electrons is ignored and only the fast ions are considered as the heat source ($\xi_e=0$). For this case, the normalized equations for the cloud, Eqs.(3.27) to (3.30), reduce to

$$\frac{dv'}{dr'} = \frac{2}{\Theta'^2-v'^2}\left(E_f'^{0.9} - \frac{\Theta'^2 v'}{r'}\right) , \tag{4.13}$$

$$\frac{d\Theta'}{dr'} = \frac{E_f'^{0.9}}{v'\Theta'} + \frac{(1-\gamma)v'}{2\Theta'}\frac{dv'}{dr'} , \tag{4.14}$$

$$\frac{dE_f'}{dr'} = \frac{E_f'^{0.9}D}{0.9r'^2v'} . \tag{4.15}$$

The eigenvalue of these equations is D in (4.15), which is related to $dv'/dr'|_{r'=1}$ by Eq.(3.35), and, regardless of the fast ion energy, this eigenvalue and normalized solutions are determined uniquely to be D=0.55279, $\hat{r}_p$=0.61560, $\tilde{E}_f$=1.3429 as in Table 4-I. When the heat flux of the electron is ignored, the heat source is determined by the fast ion energy only in the normalized form as $W'=E_f'^{3/2}\Lambda_f'=E_f'^{0.9}$ This is the reason why the normalized solutions are independent of the fast ion energy. Therefore, the ablation rate of the pellet is given by a scaling law such as

$$G = 5.712\times10^{7}m^{2/3}q_{f\infty}^{1/3}E_{f\infty}^{2/5}r_p^{4/3}$$
$$= 5.712\times10^{7}m^{2/3}(G_f n_{f\infty})^{1/3}E_{f\infty}^{0.9}r_p^{4/3} \ (\mathrm{kg/sec}) , \qquad (4.16)$$

or

$$\dot{r}_p = 4.55\times10^{6}\rho_s^{-1}m^{2/3}(G_f n_{f\infty})^{1/3}E_{f\infty}^{0.9}r_p^{-2/3} \ (\mathrm{m/s}) . \qquad (4.17)$$

Since the heat source of the cloud for (a) is stronger than for (b), the velocity v becomes larger in (a) (see Fig.4.1). However, from the mass conservation law (3.2), the ablation rate of the pellet is determined by ρv. In the case of (b), therefore, the cloud density ρ in Fig.4.1 becomes large enough that (b) has the larger ablation rate than (a) (see Table 4-I). The reason is that the attenuation of the fast ions in the present energy ranges is much less than that of the thermal electrons, which requires the high cloud density to attenuate the heat flux due to fast ions sufficiently. Accordingly, fast ions contribute weakly to the heating of the whole cloud but have a significant influence on the heating in the neighborhood of the pellet surface or on the energy balance at the pellet surface.

For the case of (c), the cloud has also high density like (b)

to attenuate incident fast ions sufficiently (see Fig.4.1). Incident electrons, therefore, cannot reach to the pellet surface and contribute only to heat up the cloud around the sonic radius. The cloud temperature and the flow velocity near the pellet surface are low, since the heat source due to fast ions only is weak and the cloud density is high. However, in the distance of about two pellet radii from the center of the pellet where electrons can reach, the cloud is heated up and accelerated by the strong heating from the incident electrons. These are the reason why Mach number has a dip in the subsonic region and the sonic transition point moves further from the pellet surface. This phenomena might be general for the case that heat fluxes with different ranges exist in the cloud. And the ablation cloud structure might differ from the case that one of the incident heat fluxes is assumed to be dominant like (a) or (b). The effect of the change of the cloud structure on the ablation rate is considered in next section 4.3. If the range of electrons is quite different from that of ions and electrons can not reach to the sonic radius, Mach number might have a dip in supersonic region. It is unable to calculate this case by our model; however, the dip in Mach number in supersonic region might have little effects on the ablation rate. The cloud heating in the region far from the pellet surface does not affect the cloud parameters near the pellet surface, which determine the ablation rate. Accordingly, neglect of the incident electrons like (b) will be good approximation for such a case.

In analyses of the neutral beam heating experiments, a fast ion distribution function is discussed and there are several standard methods to calculate it. We assume, therefore, that a

distribution function of fast ions, $f(v_f,\theta)$ at each flux surface is known by using a Fokker-Planck code, where v_f is velocity of fast ions and θ is pitch angle against a magnetic field line. We write an averaged distribution function of $f(v_f,\theta)$ over θ as $f(v_f)$. Representative energy of fast ions which has weight on high energy components is given by[12)]

$$E_{f\infty} = \left(\frac{4\pi}{n_{f\infty}}\int_0^\infty \left(\frac{1}{2e}m_f v_f^2\right)^3 f(v_f)\, v_f^2 dv_f\right)^{1/3}, \tag{4.18}$$

where

$$n_{f\infty} = 4\pi\int_0^\infty f(v_f)\, v_f^2 dv_f \ . \tag{4.19}$$

Heat flux of fast ions to the pellet is estimated by

$$q_{f\infty} = \frac{\pi m_f}{2e}\int_0^\infty v_f^5 f(v_f)\, dv_f \ . \tag{4.20}$$

Figure 4.2 shows a dependence of the ablation rate, $|dr_p/dt|$, on $n_{e\infty}$ and $T_{e\infty}$ for a fixed distribution function of fast ions and pellet radius. In this case, one dimensional analytic solution of Fokker-Planck equation for fast ions

$$f(v_f) = \sum_{j=1}^{3}\frac{S_j\tau_s}{4\pi(v_f^3+v_c^3)}U\left(t-\frac{\tau_s}{3}\ln\frac{v_{0j}^3+v_c^3}{v_f^3+v_c^3}\right) \tag{4.21}$$

is used to calculate representative energy (4.18) and heat flux (4.20)[12)], where U means a step function, S_j is a particle source for j-th injection energy component of fast ions, τ_s is Spitzer's slowing down time, v_{0j} is an injection velocity of the j-th component, v_c is a critical velocity, and t is a time duration from the beginning of NBI-heating. For Fig.4.2 parameters of fast ions derived from Eqs.(4.18)-(4.20) are fixed as $n_{f\infty}=2\times10^{18}\mathrm{m}^{-3}$, $E_{f\infty}=25.53\mathrm{keV}$, and $q_{f\infty}=1.44\times10^{28}\mathrm{eV/m^2sec}$, and the pellet radius is

0.5mm. These are the same parameters as used for Fig.4.1. Similarly, Fig.4.3 shows a dependence of $|dr_p/dt|$ on $n_{e\infty}$ and $T_{e\infty}$ for the case of neglecting fast ions or $\xi_e=1$. It is noted that the ablation rate is governed by fast ions in low $T_{e\infty}$ plasmas and the difference between Fig.4.2 and Fig.4.3 becomes small for high $T_{e\infty}$ plasmas. It is reasonable that influence of fast ions is significant for low $n_{e\infty}$, since $n_{f\infty}$ is fixed. The effect of fast ions, therefore, is more pronounced, when $n_{e\infty}$ and $T_{e\infty}$ are low like in the peripheral region of plasma column

We compare our results with Milora model including the heat flux due to fast ions[8] described briefly in Appendix. We developed a numerical code based on this Milora model and obtained Fig.4.4 for the same conditions as Fig.4.2. By comparing Fig.4.4 with Fig.4.3, the effect of fast ions on the pellet ablation rate is small in the high electron temperature regime, where our model agrees with Milora model except difference owing to the numerical method. However, this becomes more significant for the low $T_{e\infty}$ and low $n_{e\infty}$ regime than our model in Fig.4.2. In an intermediate regime where $T_{e\infty}\sim 1$ keV for this example, this difference is more pronounced. Our model predicts that the ablation rate does not increase monotonically, when $T_{e\infty}$ increases. However, Fig.4.4 shows monotonic increase of ablation rate. It is considered that the change of the cloud structure due to fast ions is not taken into account in Milora model. In Milora model, it is assumed that the relationship between the heating power in the cloud and the integrated column density of the cloud follows the same scaling as that is obtained for electron heating only even in the presence of fast ions. On the contrary we solved the fluid equations for the

cloud. It is also assumed that the heat source for the cloud is uniform in Milora model. This means that, even in the situation that $T_{e\infty}$ is low and the range of electrons in the cloud is short, the electrons can heat the cloud near the pellet surface. Accordingly, it is probable that the ablation rate is overestimated for low $T_{e\infty}$. However, when both $n_{e\infty}$ and $T_{e\infty}$ are low and the deposited power from electrons is much smaller than that from fast ions, this assumption does not matter.

4.3 Effects of non-thermal electrons on pellet ablation

Here, we consider effects of non-thermal electrons on ablation cloud dynamics and ablation rate. We will consider two components for electrons; one is thermal electrons and the other is non-thermal electrons. In our model, both are treated as monochromatic beams with respective energies. Theoretical treatments of those two energy carriers are the same as thermal electrons and fast ions in section 4.2, but the loss function L_e of Eq.(4.3) and the effective cross-section Λ_e of Eq.(4.6) are used for both energy carriers. Heat flux of non-thermal electrons is estimated that

$$q_f = \Gamma_f E_f, \tag{4.22}$$

where

$$\Gamma_f = n_f v_f,$$
$$v_f = \sqrt{2eE_f/m_e} \quad .$$

In this section, subscript f denotes quantities for non-thermal electrons. Fractions in Eq.(3.6), f_{Be} and f_{Bf} , are assumed to be 0.6. Results of calculations are qualitatively the same as the case considering fast ions instead of the non-thermal electrons. Hereafter, we omit the subscript ∞ which designates the value in the background plasma for simplicity. In Fig.4.5, dependence of regression velocity of pellet radius for H_2-pellet on the plasma thermal electron temperature is shown at $n_e=3\times10^{19}$ m^{-3} and $r_p=0.5$ mm. The density of fast electrons is fixed to 1/1000 of thermal electron density and three cases of E_f = 10 keV, 30 keV, 50 keV are plotted in this figure. Solid line designates T_e-dependence without

considering fast electrons. In these calculations, when eigenvalue λ_* (see (3.19)) cannot be found appropriately by the shooting method, we assume that the range of thermal electrons in the cloud is much shorter than that of fast electrons and thermal electrons cannot reach the sonic radius. In such a case, we neglect thermal electrons as mentioned in section 3.2. The part where curves are flat in low T_e regime denotes the region where contribution of thermal electrons to the ablation is negligible. There is a limitation in our model for the ablation due to non-thermal electrons. If the energy of fast electrons is more than several hundred keV, the shielding of cloud may not effective for these particles and they penetrate into the solid pellet deeply. The assumption of surface ablation of the pellet, therefore, may be invalid. An application of our model to such a case results in a contradictory solution that the cloud density near the pellet surface becomes much higher than the solid density of the pellet.

In the cases shown in Fig.4.5, however, the solutions, whose eigenvalues can be successfully obtained, have an asymptote to the solutions in the low T_e regime where thermal electrons are neglected. The approximation of neglecting thermal electrons, therefore, is allowed for the low T_e cases. From Fig.4.5, the results are shown that (1) ablation rate is larger for the higher energy of fast electrons, (2) effects of fast electrons are significant in low T_e regime and negligible in high T_e regime. It is noted that there is a region where the ablation rate decreases as T_e increases. This tendency is also seen in the case of the ablation considering fast ions, but less pronounced compared to Fig.4.5. This is manifestation of importance of the cloud structure

on the ablation rate. The change of cloud sturucture is significant, when the difference between energies of two energy carriers is large. We show the results of the cases that E_f = 50 keV, 75 keV, 100 keV in Fig.4.6. Here we assumed n_f/n_e = 1/10000. (As mentioned above, there is a possibility that the results at E_f $\sim$ 100 keV in low T_e regime violates the assumption of the neutral cloud shielding.) A spike of the ablation rate at T_e = 2keV for the case of E_f = 75 keV is due to the change of the numerical procedure from the root-finding of λ_* by the shooting method to the region of neglecting thermal electron heat flux.

In order to examine the effect of two energy carriers on the cloud structure or ablation rate, the cloud stuructures for the representative cases of A (pointed with arrow A in Fig.4.6) and B (pointed with arrow B in Fig.4.6) are shown in Fig.4.7. Case A is that only fast electrons of E_f = 100 keV is considered and Case B is that both fast electrons of E_f = 100 keV and the thermal electrons of T_e = 4 keV are included. From the total value of incident heat flux to the pellet, larger ablation rate is expected for Case B; however, the result is different from the simple expectation. In Fig.4.7 for Case B, it is found that thermal elelctrons heat up the region of the cloud far from the pellet surface intensively and the subsonic region extends widely. Moreover, density of the cloud ρ is lowered by the heating and the expansion due to the thermal electrons far from the pellet surface for Case B; however, the difference of ρ in both cases of A and B is relatively small near the pellet surface. The significant differences appear in the cloud flow velocity and temperature. Equation for the cloud flow velocity (3.13) is rewrited as

$$\frac{dv'}{dr'} = \frac{2W'}{\Theta'^{2}(1-M^2)} - \frac{2v'}{(1-M^2)r'} \quad . \tag{4.23}$$

Second term of r.h.s. of this equation decreases flow velocity of the cloud in the subsonic region (where $M < 1$) and increases if in the supersonic region ($M > 1$). Since energy of non-thermal electrons is large, their attenuation is weak or heat flux deposited to the cloud W' is small. The contribution of the second term of r.h.s. in (4.23) is larger than the first term near the pellet surface ($r < 0.8$ mm) where only fast electrons reach. For Case B, therefore, expansion of the subsonic region due to heating of the cloud far from the pellet surface by thermal electrons supresses the cloud flow velocity at a value smaller than the sound velocity. Then the resultant ablation rate $dr_p/dt \propto \rho v r^2$ is smaller than that of Case A. When the energy of thermal electrons becomes high, they can reach near the pellet surface. Here the thermal electrons heat and expand the cloud near the pellet surface dominantly and the ablation rate is enhanced. These tendencies are similar to those found in ablation due to both thermal electrons and fast ions (see Fig.4.1).

4.4 Conclusion

We apply our model, which can treat multiple energy carriers incident to the pellet, to the cases (1) including incident heat fluxes both of thermal electrons and fast ions[7] and (2) including incident heat fluxes both of thermal electrons and non-thermal electrons. It is found that the existence of multiple energy carriers can modifiy the ablation cloud dynamics substantially. It is concluded that, if the pellet is shielded by its ablation cloud, the ablation rate of the pellet cannnot be determined simply by the total incident heat flux to the pellet surface or deposited power to the cloud. The ablation rate must be calculated considering the modification of the cloud dynamics by the presence of multiple energy carriers. We have also found that, when the incident heat flux of fast ions dominates the ablation properties or that of thermal electrons can be neglected in the pellet injection into an NBI heated plasma, the ablation rate can be calculated by the simple scaling law.

Table.4-I. Numbers from the solutions of the fluid equations for the cloud corresponding to three cases in Fig.4.1. Eigenvalue, $D_*\lambda_*$ or λ_*, asymptotic values of normalized solutions, $\tilde{E}_e$, $\tilde{q}_e$, and $\tilde{E}_f$, and normalized pellet radius, $\hat{r}_p$, are obtained from the solutions of normalized equations with input parameters, (E_{e*}, E_{f*}, ξ). The r_* and $\dot{r}_p$ are calculated for ambient plasma parameters, $n_{e\infty}=6\times10^{19}m^{-3}$, $T_{e\infty}=200$ eV, $n_{f\infty}=2\times10^{18}m^{-3}$, $E_{f\infty}=25.53$ keV, and $q_{f\infty}=1.44\times10^{28}$ eV/m^{2}sec, and the pellet radius, $r_p=0.5$mm.

	E_{e*}(eV)	E_{f*}(keV)	ξ	$D_*\lambda_*$	E_e	q_e	E_f	r_p	r_*(mm)	$\lambda_*(m^{-2})$	$\dot{r}_p$(m/s)
(a)	358.9	-----	1.000	0.586	1.115	1.553	-----	0.6036	0.828	3.04×10^{20}	-0.313
(b)	-----	19.01	0.000	0.553	-----	-----	1.343	0.6156	0.812	1.18×10^{22}	-2.560
(c)	354.6	25.33	0.985	0.651	1.129	1.634	1.008	0.1471	3.400	3.36×10^{20}	-2.244

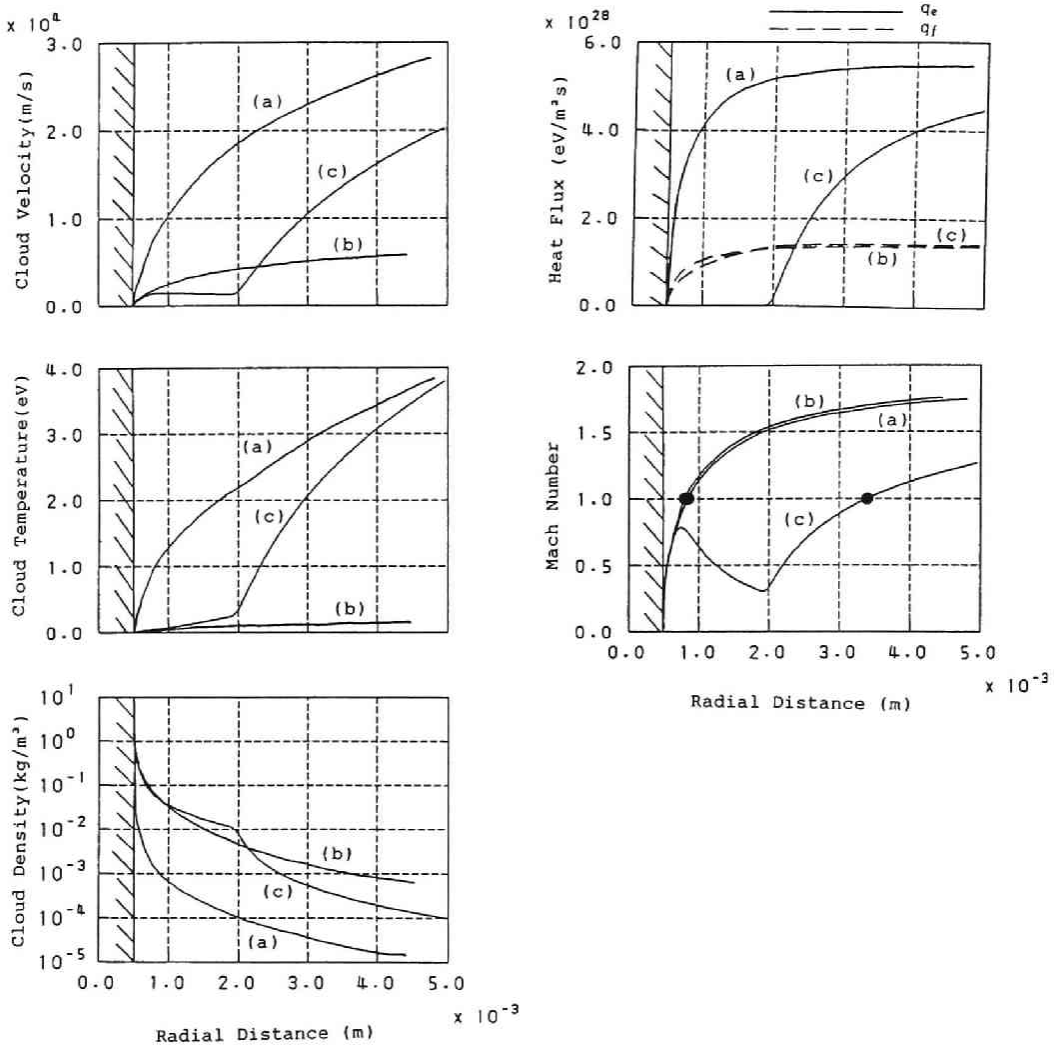

Fig.4.1. Cloud structure of H_2 pellet by the present model for three cases including incident heat flux due to (a) electrons only, (b) fast ions only, (c) both electrons and fast ions. Ambient plasma parameters are $n_{e\infty}=6\times10^{19}m^{-3}$, $T_{e\infty}=200$ eV, $n_{f\infty}=2\times10^{18}m^{-3}$, $E_{f\infty}=25.53$ keV, and $q_{f\infty}=1.44\times10^{28}$ eV/m^{2}sec ; the pellet radius, $r_p=0.5$mm. The abscissas denote radial distances from the pellet center. In the figure of Mach number, dark circles denote the positions of sonic radii where Mach number becomes unity.

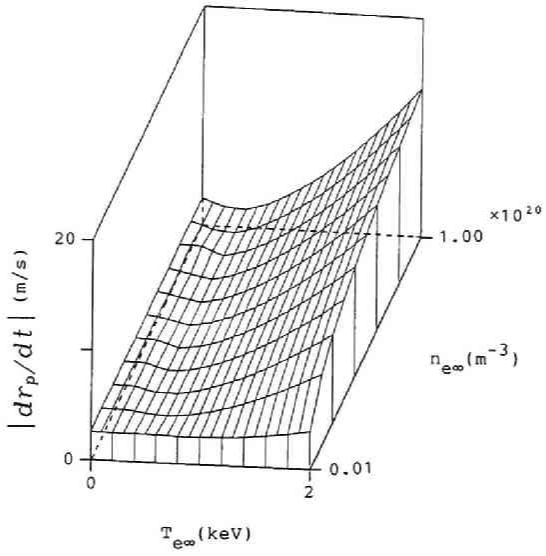

Fig.4.2. Dependence of ablation rate $|dr_p/dt|$ of H_2 pellet on $n_{e\infty}$ and $T_{e\infty}$ for a fixed distribution function of fast ions and a pellet radius obtained by including both electron and fast ion heat flux. r_p=0.5mm, $n_{f\infty}$=2×10^{18}m^{-3}, $E_{f\infty}$=25.53 keV, $q_{f\infty}$=1.44×10^{28} eV/m^{2}sec .

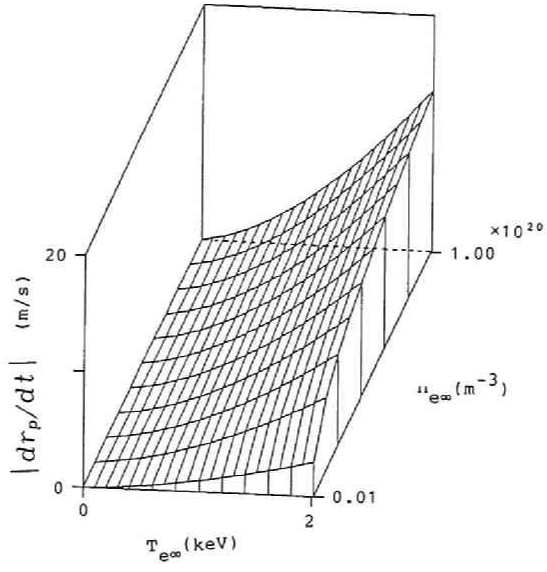

Fig.4.3. Dependence of ablation rate $|dr_p/dt|$ on $n_{e\infty}$ and $T_{e\infty}$ of H_2 pellet for the case where fast ion heat flux is neglected. r_p=0.5mm.

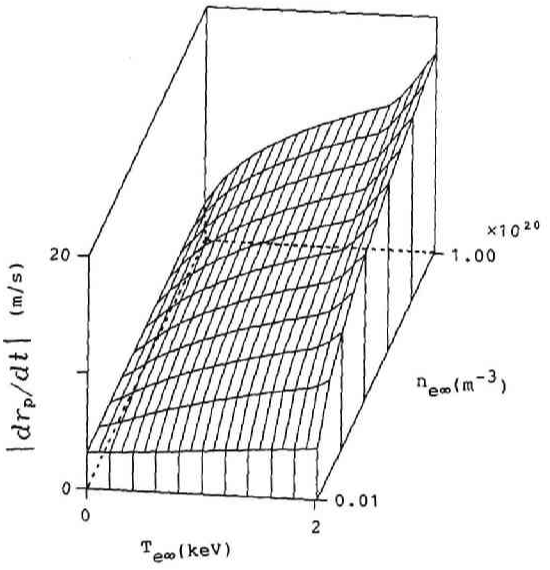

Fig.4.4. Dependence of ablation rate $|dr_p/dt|$ of H_2 pellet obtained from Milora model on $n_{e\infty}$ and $T_{e\infty}$ under the same conditions as in Fig.4.2.

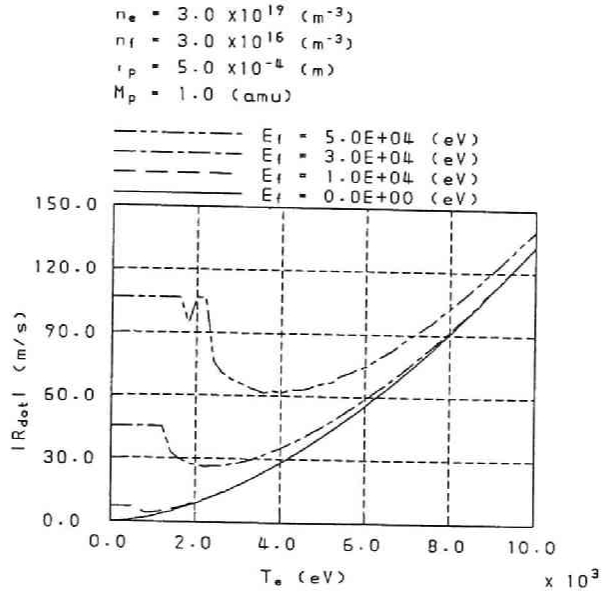

Fig.4.5. Dependences of ablation rate $|dr_p/dt|$ of H_2 pellet on $T_{e\infty}$ obtained by including both thermal electron and non-thermal electron heat flux. r_p=0.5mm, n_e=3×10^{19}m^{-3}, n_f=3×10^{16}m^{-3}, E_f=10keV,30keV,50keV

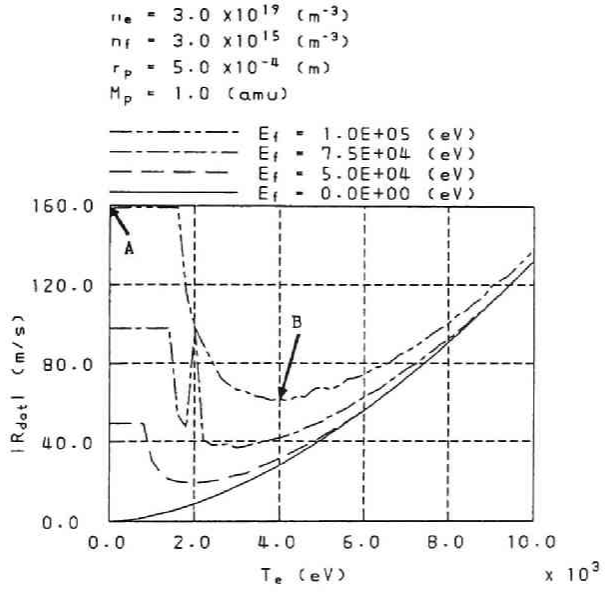

Fig.4.6. Dependences of ablation rate $|dr_p/dt|$ of H_2 pellet on $T_{e\infty}$ obtained by including both thermal electron and non-thermal electron heat flux. r_p=0.5mm, n_e=3×10^{19}m^{-3}, n_f=3×10^{15}m^{-3}, E_f=50keV,75keV,100keV. Cloud structures for cases A and B indicated with arrows in this figure are shown in Fig.4.7.

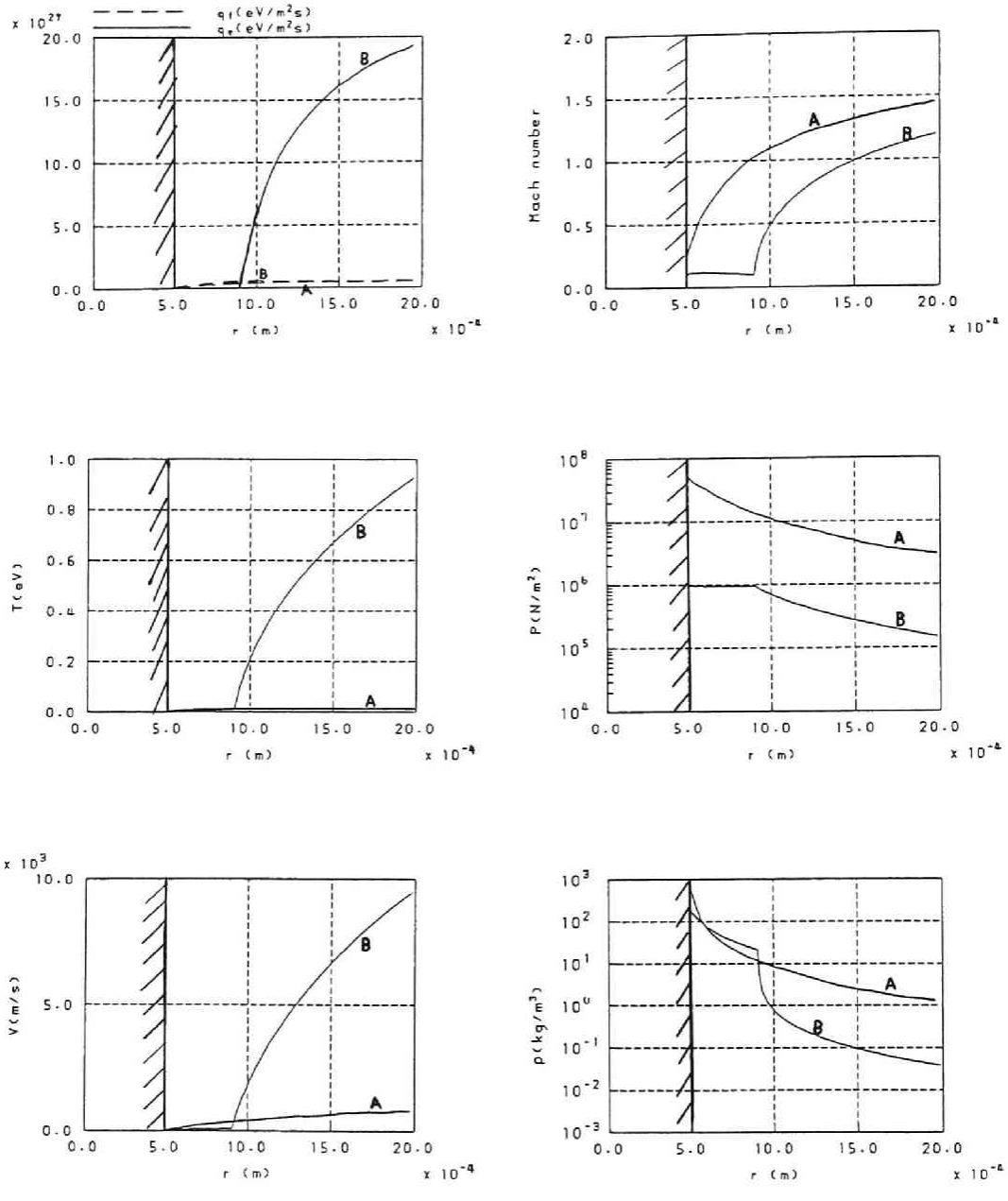

Fig.4.7 Cloud structure of H_2 pellet by the present model for cases including incident heat flux due to (A) non-thermal electrons only, (B) both thermal electrons and non-thermal electrons. Ambient plasma parameters are indicated with arrows in Fig.4.6.

CHAPTER 5

Calculations of Pellet Ablation Rate Profile Injected into Torus Plasmas

5.1 Introduction

The pellet ablation model presented in chapter 4 makes it possible to calculate cloud structure surrounding a pellet and instantaneous ablation rate, when a pellet is explosed in the plasma with given parameters. In pellet injection experiments, a pellet moves in an inhomogeneous plasma with various plasma parameters and size of the pellet itself changes by ablation process during penetrating into the plasma. An ablation rate profile is measurable from H_α line due to the neutrals surrounding a pellet[12),17)]. Increase of line averaged plasma density is also usable to study the ablation rate profile. Therefore, we need comparison of the ablation rate profiles between experimental data and numerical results to test the pellet ablation theory. In this chapter, we describe a method to calculate the ablation rate profile in a toroidal plasma with inhomogeneous plasma parameters by considering change of the pellet size, and we compare results from the present model, which includes the effect of fast ions, to those from the Milora model (it is also includes the effect of fast ions in a different way, see Appendix). An analysis to optimize pellet injection parameters according to the experimental conditions, such as injection velocity of the pellet and its size, is also discussed.

5.2 Development of ABLATE code

A code which calculates ablation rate profiles of pellets injected into magnetically confined plasmas is named as ABLATE. During the development of this code, 'Pellet' routine by W.A.Houlberg et al.[51] was referred. In the ABLATE code, cross-section of a toroidal plasma is divided by several spatial grids on flux surfaces shown in Fig.5.1 and time evolution of a pellet radius r_p is described by

$$\frac{dr_p}{dt} = -\dot{R}_p(r_p(t), (\text{plasma parameters})) \qquad (5.1)$$

in each mesh region. Here, $\dot{R}_p$ is an absolute value of regression velocity of the pellet radius determined by the pellet ablation process and it is a function of r_p and plasma parameters generally. When spatial grid spacing is appropritely chosen, plasma parameters can be approximated to be uniform in each mesh region. If the pellet injection velocity is considerably large and perturbations of plasma parameters due to the pellet ablation are sufficiently small, plasma parameters in the j-th mesh where the pellet exists are assumed constant for Δt_j ;

$$\Delta t_j = \Delta x_j / v_p \qquad (5.2)$$

which denotes a time that the pellet pass through the j-th mesh. Here, Δx_j is a pass length of the pellet in j-th mesh region (see Fig.5.2) and v_p is a pellet injection velocity. By integrating Eq.(5.1) over the period Δt_j, therefore, a change of the pellet radius in j-th mesh region or particle numbers deposited in this region is calculated and the volume-averaged density increment is

give by averaging the deposited particle numbers over the volume of the j-th mesh.

From these procedures, the ablation rate of the pellet and the neutral particle source are obtained; however, perturbations of the background plasma parameters due to the pellet ablation are not considered so far. When the pellet is injected into a plasma with $T_e \sim T_i$, electrons having large thermal velocity compared to ions move along the magnetic field lines and reach to the pellet dominantly and lose their energy due to both the impact ionization with pellet particles and collisions with cold electrons produced by the pellet ablation. When cold electrons are increased in the background plasma, the electron energy distribution changes to a new Maxwellian distribution after several electron-electron collision times τ_{ee} . These cooling of plasma temperature and increase of plasma density affect the pellet ablation itself, when the characteristic time of the pellet motion is much longer than τ_{ee} . This mechanism is called 'self-limiting ablation'[51], which is included in the ablation rate calculation of the ABLATE code.

Interactions between the plasma and the pellet may be assumed adiabatic, since Δt_j is much smaller than the characteristic time of plasma radial transport generally. Then, we describe the change of the density and the energy of plasma electrons as

$$\frac{d(n_e)_j}{dt} = \frac{4\pi r_p^2 n_s \dot{R}_p}{V_j} \quad , \tag{5.3}$$

$$\frac{d(\frac{3}{2}n_e T_e)_j}{dt} = -\frac{4\pi r_p^2 n_s \dot{R}_p \varepsilon_l}{V_j} \quad , \tag{5.4}$$

where n_s is a number density of pellet atoms, V_j is a volume in j-th mesh region, and ε_l is an average electron energy loss due to

ionization and dissociation of a pellet particle. Here, we assume that ε_I is 40 eV/atom. By solving a set of differential equations (5.1), (5.3), and (5.4) simultaneously for the period Δt_j in each mesh, changes of r_p, n_e, and T_e are obtained. These are several options in ABLATE code, MF model[19], the Milora model including fast ion ablation process[8], PT model[6], and our model discussed in chapter 3 and 4.

As an example of results from the ABLATE code, ablation rate profiles in a torus plasma are shown in Fig.5.3. The plasma has a major radius of 2.2 m and a minor radius of 0.2 m. Parameters of plasma electrons are

$$n_e(r) = 6\times10^{19}\{1-(r/a)^2\}+5\times10^{17}\ [m^{-3}] \quad ,$$
$$T_e(r) = 600\{1-(r/a)^2\}+10 \qquad [eV] \quad ,$$

and the pellet contains 5.86×10^{19} H-atoms corresponding to 1 mm-diameter and 1.4 mm-length cylindrical pellet. In this example, the original Milora-Foster model is used which includes the ablation due to only thermal electrons. When the pellet velocity exceed 600 m/s, a pellet can reach the magnetic axis. Here, the ablation rate is significantly supressed at the magnetic axis. Since the volume V_j between the spatial grids becomes small in the neighborhood of the magnetic axis and increase of plasma electron density due to the pellet ablation is considerable and the 'self-limiting ablation' mechanism becomes more effective near the magnetic axis[12]. Electron density and electron temperature profiles just after the pellet injection calculated from (5.3) and (5.4) are shown in Fig.5.4. The pellet injection condition and the target plasma parameters are the same as those in Fig.5.3. Although the

ablation rate decreases in the central region of the plasma column due to the 'self-limiting ablation', significant density increase and temperature decrease are still observed. When the pellet injection velocity is 800 m/s, nearly 70 % of pellet particles ablate in the central region of $r/a<0.5$.

When plasma parameters are given, we can estimate injection conditions required for effective supply of neutral particles or control of density profile by using the ABLATE code for various pellet sizes and injection velocities. The results are summariezed in Fig.5.5. Plasma parameters are the same as those used in both Fig.5.3 and 5.4, and total number of electrons is appproximately 5×10^{19} before pellet injection and this is shown in this figure by dashed line. Figure 5.5 shows contours of content numbers of pellet particles ablated in a central region of plasma ($r/a<0.5$) and the dotted region denotes injection parameters with which above 60 % of the total pellet particles can ablate in the central region. When the injection parameter exists in the up and right region from dot-dashed line in this figure, the pellet exceeds the magnetic axis, and when it is in the up and right region from dot-dot-dashed line, the pellet goes through the whole plasma column before it ablates completely From this figure, if we design to inject a pellet containing neutral particles equal to total number of plasma particles and to supply as possible as particles to the plasma central region under the condition that the pellet ablates completely inside the plasma column, injection velocity of 800 to 900 m/s is required.

As shown above, even if plasma parameters are fixed, pellet size and injection velocity depends on requirements. Since

effectiveness of pellet injection is related to the macroscopic stability and transport process, further examination taking into account of experimental conditions will be needed. Stability analysis related to the pellet injection is discussed in 7.4 and the transport coupled to the pellet injection is one of the main problems of this thesis and it is discussed in 6.3, 7.3, and 8.3.

5.3 Ablation rate profile by the present model and comparison with the Milora model

First, by using the ABLATE code, pellet injection into a plasma in a PDX-tokamak-like device is analysed by our including fast ions. The ablation rate profile is calculated, for the case where a spherical H_2 pellet of a diameter of 1.7 mm (1.37×10^{20} atoms in the pellet) is injected at a velocity of 900 m/s into a toroidal deuterium plasma with circular cross-section, major radius R_0=1.38 m, and minor radius a=0.45 m. The plasma is heated for 30 ms by a deuterium neutral beam, with injection energies of 50 keV, 50/2 keV, 50/3 keV, whose beam fraction is 0.45:0.30:0.25[8] . In Fig.5.6(a) and (b), the n_e and T_e profiles both just before and just after pellet injection are shown. The profiles just before the pellet injection are given by

$$n_e(r) = (4\times10^{19}-2\times10^{18})\{1-(r/a)^4\}^2+2\times10^{18}\ [m^{-3}] \quad ,$$

and

$$T_e(r) = (1100-50)\{1-(r/a)^2\}+50 \qquad [eV]$$

They are represented by dashed lines in the figures. Here, r denotes the radial distance from the magnetic axis. The solid lines in these figures designate the n_e and T_e profiles just after pellet injection calculated from our model. Parameters for the fast ions are shown in Fig.5.6(c). Here, instead of a self-consistent calculation for the deposition profile of the fast ions, a probable density profile of the fast ions is assumed in the form

$$n_f(r) = (5\times10^{18}-1\times10^{16})\{1-(r/a)^2\}^2+1\times10^{16}\ [m^{-3}]$$

We calculate E_f and q_f from Eqs.(4.18) and (4.20) with a distribution function of the form (4.21), where the S_j are determined so as to reproduce the above mentioned density profile. In Fig.5.6(d), the ablation rate profiles are shown with the number of ablated atoms per unit path length of the pellet. The ablation rate profiles as calculated by including heat fluxes of both electrons and fast ions are represented by the solid line. The dashed line refers to the Parks-Turnbull model which neglects the heat flux of the fast ions ($\xi_e=1$) and the dot-dashed line shows the case where the heat flux of the electrons is neglected ($\xi_e=0$), which is hypothetical since fast ions cannot exist alone in the plasma bulk, where ξ_e is a ratio of the heating power to the cloud due to thermal electrons to the total heating power at the sonic radius (see Eq.(3.26)). From these curves, it is found that the pellet ablation rate is enhanced by the heat flux of the fast ions and that the pellet lifetime becomes shorter than the value obtained by the Parks-Turnbull model. For this example, the pellet lifetime for the solid line is nearly equal to that obtained from the model considering fast ions only (dot-dashed line), which is calculated from the scaling equation (4.16) or (4.17). The ablation rate is enhanced by the effect of fast ions, especially in the peripheral region of the plasma where both electron density and temperature are low. These results seem to be consistent with the experimental results.

In order to compare our results with those of the Milora model including heat flux due to fast ions. The ablation rate profile calculated from the Milora model, when a pellet is injected into the same plasma as in the case of Fig.5.6, is shown in Fig.5.7. The

pellet life time is , then, half of that from our model. In Ref.(8), the penetration obtained from Milora model is 27 cm, which is larger than that shown in Fig.5.7. The difference may come from the fast ion density profile. We took a broader profile than Ref.(8), since the $E_f/2$ and $E_f/3$ components were assumed to deposit near the edge region, where E_f is the injectin beam energy The penetration length in the experiment is estimated to be 29 to 32 cm[8] . This is a little shorter than that shown in Fig.5.6. The experimental information is limited to the function of determining which model is more suitable for an analysis of pellet injection experiments. We need the profiles of plasma parameters, in particlar the local distribution function of the fast ions, in order to verify our model. It is not only necessary to compare the lifetimes but also the ablation rate profiles with the experimental data for different parameter ranges.

Next, we consider the effect of non-thermal electrons on the ablation rate. Figure 5.8(a) shows the ablation rate profile in a plasma with a major radius of 2.2 m and a minor radius of 0.2 m in the presence of non-thermal electrons with energy of E_f=10 keV. Plasma thermal electron density and temperature profiles and fast electron density profile just before the pellet injection are also shown in Fig.5.8(b), (c), and (d). For this example, the fast electrons are assumed to be localized around r=0.12 m and maximum density is 10^{17} m^{-3} . H_2 pellet with radius of 0.572 mm, which is equivalent to a cylindrical pellet with diameter of 1 mm and length of 1 mm, is injected with velocity of 800 m/s. As a result, the pellet penetration of 8 cm is obtained. To see the effect of fast electrons, the ablaiton rate profile calculated without considering

the fast electrons (PT model) is shown in Fig.5.9. In this case, the pellet exceed the magnetic axis and the pellet penetration becomes 35 cm. These results show that non-thermal electrons may contribute pellet ablation significantly. The non-thermal electrons are produced in a runaway or slide-away discharge or RF heating such as electron cyclotron heating and lower hybrid heating in tokamaks.

5.4 Conclusion

We developed the ABLATE code which calculates ablation rate profiles of pellets injected into magnetically confined toroidal plasmas. By using this code, we can estimate the ablation rate profile in the experiment, and optimize pellet injection conditions required for effective fueling. Moreover, by coupling it with a transport code, it is able to analyze transport properties after the pellet injection, which will be discussed in sections 6.3, 7.3, and 8.3.

We analysed pellet injection into a neutral beam heated toroidal plasma by using the ABLATE code and compared the results from our model to those from the Milora model[8]. It is found that fast ions affect the pellet ablation espcially in the peripheral region of the plasma column as observed in the experiments. Our model gives a longer pellet life-time than the Milora model. As discussed in chapter 4, the main reason is that our model includes the effect of the modification of ablation dynamics due to fast ions but the Milora model does not. We also showed that non-thermal electrons, produced by such as ECRF heating, may contribute to the pellet ablation considerably.

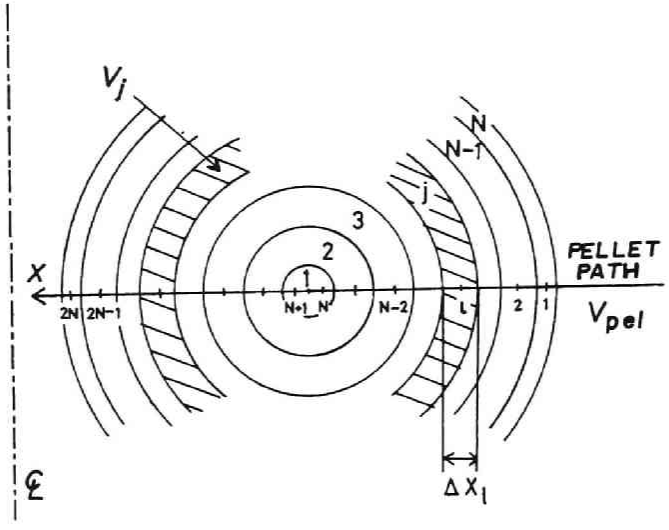

Fig.5.1. Spatial meshes of plasma column. Δx_l is path length of pellet through l-th mesh region (or j-th mesh region), and V_j is volume contained in j-th mesh region.

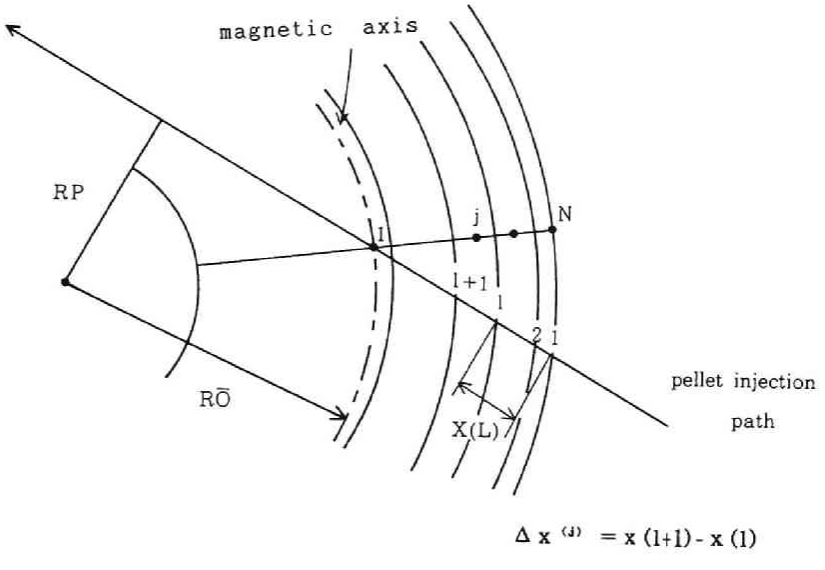

Fig.5.2. Top view of plasma column and pellet injection path.

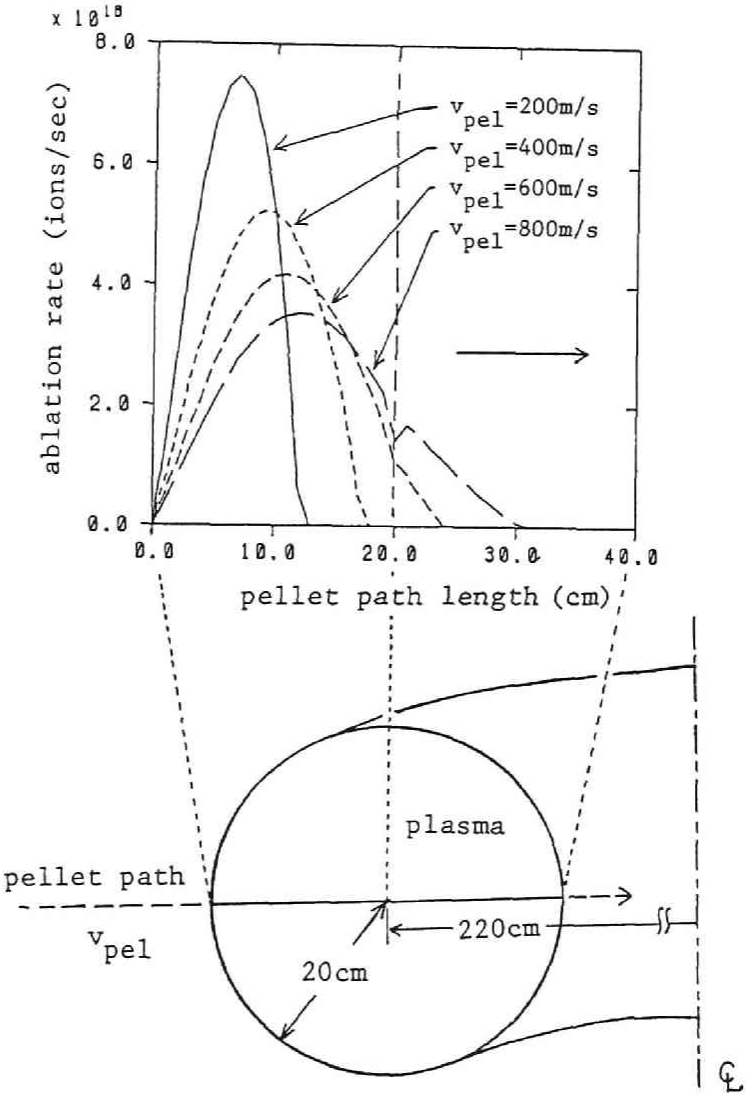

Fig.5.3. Example of ablation rate profile obtained by ABLATE code with the Milora Foster model.

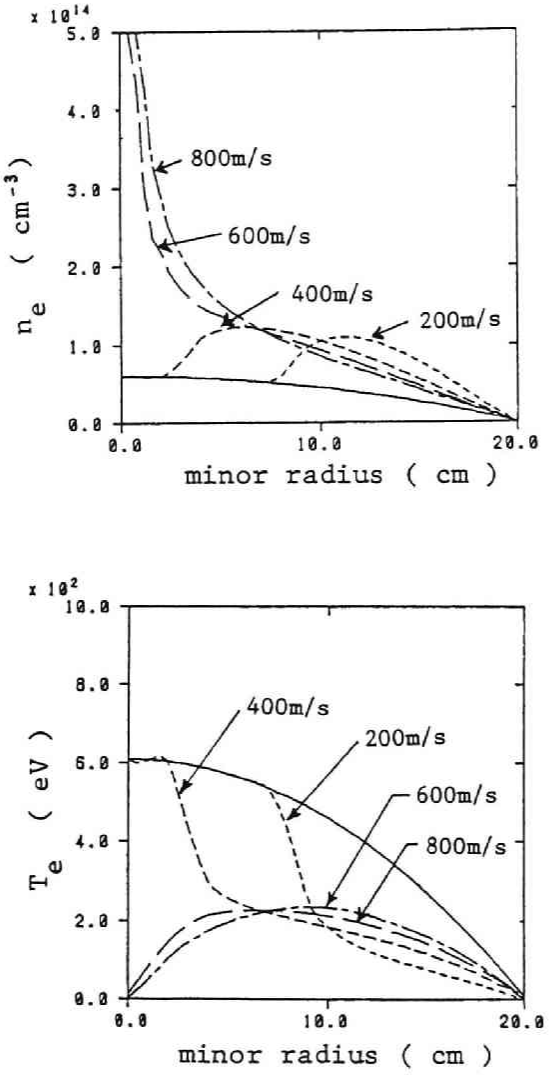

Fig.5.4. Example of density and temperature profile just before and after pellet injection corresponding to Fig.5.3.

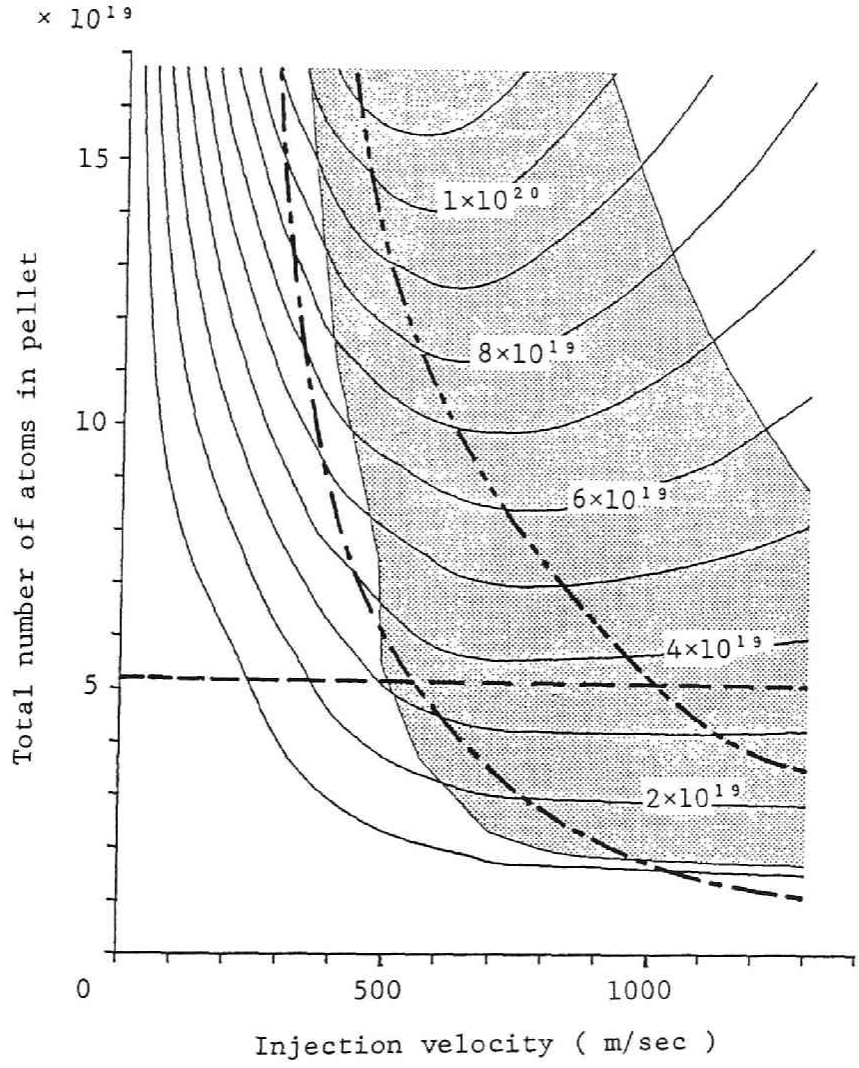

Fig.5.5. Contour plots for number of pellet atoms deposited in core plasma, $r/a<0.5$. Dotted region corresponds to injection parameters with which 60% of the total pellet particles ablate in core plasma. Pellet passes the magnetic axis in the region above dash-dotted line and passes through the plasma column in the region above dash-dot-dotted line.

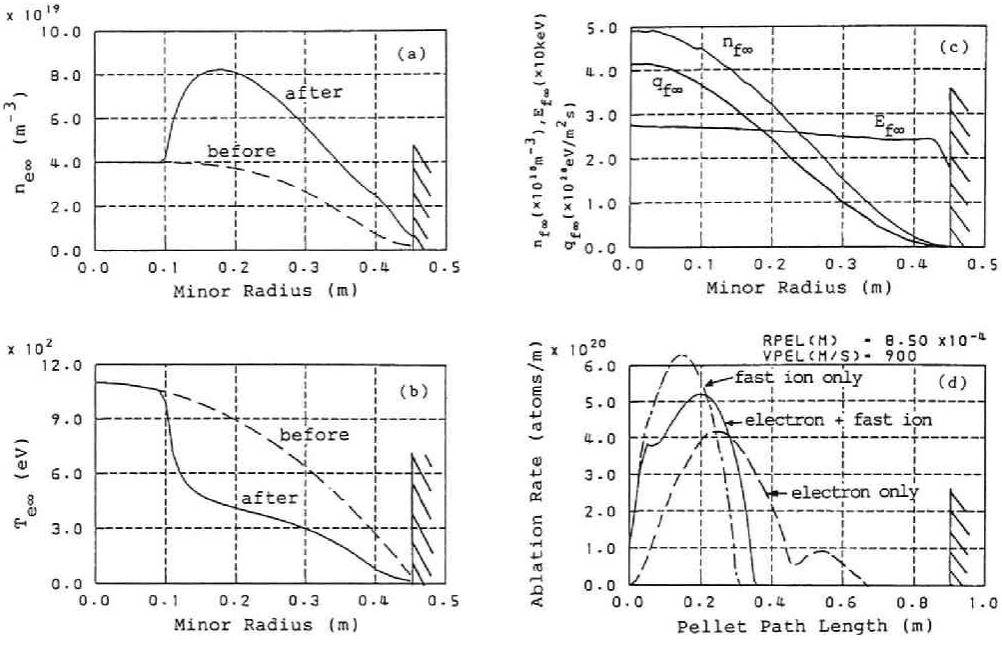

Fig.5.6. Ablation rate profile obtained by our model for the H_2 pellet injection into toroidal deuterium plasma of PDX-tokamak-like-device (R_0=1.38 m and a=0.45m). The pellet diameter is 1.7mm. Target plasma parameters are shown in figures (a), (b) and (c). (a), (b); profiles of $n_{e\infty}$ and $T_{e\infty}$ after pellet injection when both electron and fast ion heat fluxes are included. Figure (d) shows ablation rate profiles along the pellet path; dashed line denotes case of electron heat flux only, dash-dotted line denotes case of fast ion heat flux only, and solid line denotes the case with both heat fluxes.

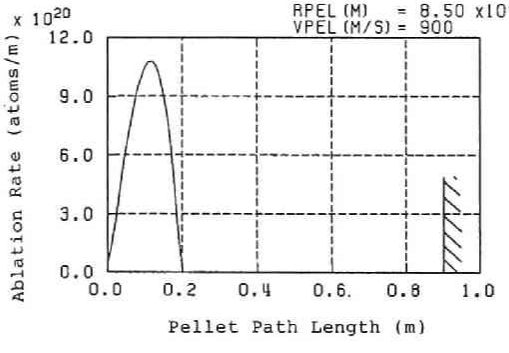

Fig.5.7. Ablation rate profile obtained from Milora model for the same conditions as in Fig.5.6.

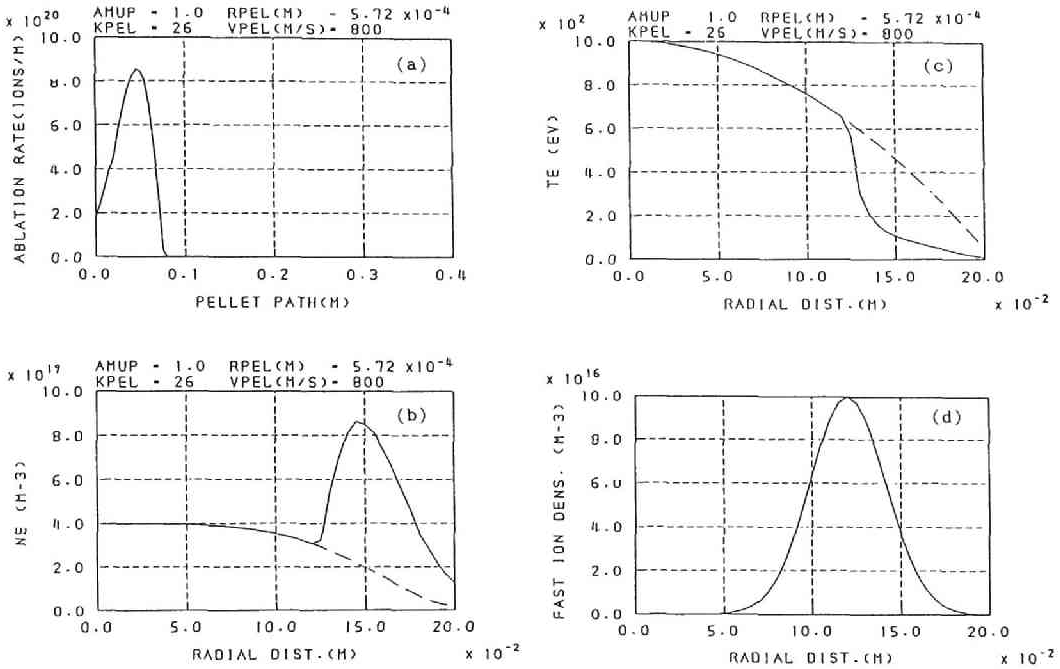

Fig.5.8. Results for the case in the presence of non-thermal electrons. (a) Ablation rate, (b) thermal electron density, (c) thermal electron temperature, and (d) non-thermal electron density profiles just before and after pellet injection. Non-thermal electron energy is 10keV.

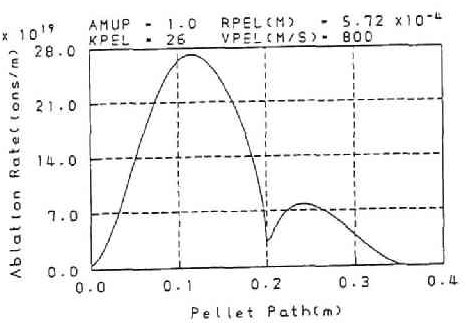

Fig.5.9. Ablation rate profile obtained by neglecting non-thermal electrons for the same conditions as in Fig.5.8.

CHAPTER 6

Transport Code Including Pellet Injection and Its Application to ISX-B Experiment

6.1 Introduction

Influences of the pellet injection on plasma equilibrium, stability and transport is the most important issue for the pellet fueling. To study transport properties numerically, one dimensional (1-D) transport code[52),53)] coupled with ABLATE code (see section 5.2) has been developed. Using the code, we studied the time evolution of plasma parameter, such as density, temperature and current profile, after the pellet injection. First, we describe our transport model and discuss the coupling of the ABLATE code to the transport code. As an example, we analysed a pellet injection into an Ohmic heating plasma in the ISX-B tokamak[12)].

6.2 Description of the transport model

In order to examine the time evolution of plasma parameters and to calculate the confinement time and the energy balance at steady stata, we use one dimensional transport code. In our transport code, coupled with the ablation code ABLATE, we solve the following equations for electron density, n_e, electron temperature, T_e, ion temperature, T_i, and poloidal magnetic field, B_p :

$$\frac{\partial n_e}{\partial t} = -\frac{1}{r}\frac{\partial}{\partial r}(r\Gamma_e) + \dot{S} , \tag{6.1}$$

$$\frac{\partial}{\partial t}(\frac{3}{2}n_eT_e) = -\frac{1}{r}\frac{\partial}{\partial r}(rQ_e) + W_e , \tag{6.2}$$

$$\frac{\partial}{\partial t}(\frac{3}{2}n_iT_i) = -\frac{1}{r}\frac{\partial}{\partial r}(rQ_i) + W_i , \tag{6.3}$$

$$\frac{\partial B_p}{\partial t} = \frac{\partial}{\partial r}(\frac{\eta}{\mu_0}\frac{1}{r}\frac{\partial}{\partial r}(rB_p)) , \tag{6.4}$$

where n_i is ion density, Q_e and Q_i include both conduction and convection terms as

$$Q_e = \chi_e n_e\frac{\partial T_e}{\partial r} + \frac{3}{2}T_e\Gamma_e , \tag{6.5}$$

$$Q_i = \chi_i n_i\frac{\partial T_i}{\partial r} + \frac{3}{2}T_i\Gamma_e , \tag{6.6}$$

and Γ_e is radial particle flux for electrons,

$$\Gamma_e = D\frac{\partial n_e}{\partial r} . \tag{6.7}$$

$\dot{S}$ is the electron source term due to ionization of recycled neutrals and neutral beam particles during NBI heating. W_e includes the energy deposition to electrons by NBI, Ohmic input power, and

ionization loss, and W_i includes the energy deposition to ions by NBI and charge exchange loss. Both terms also include the energy exchange between electrons and ions. In the calculation of neutral beam heating, we solve numerically the two dimensional linearized Fokker-Planck equation in velocity space for fast ions (Fast Ion Fokker-Planck Code ; FIFPC)[54]. Furthermore, we assume tangential injection of NBI. The neutral particles are included through the AURORA code which is based on the Monte-Carlo method[55], the halo neutrals produced by the NBI are, however, neglected. The impurity effect is included through Z_{eff}=2 and the radiation loss is simulated by enlarging the electron ionization loss energy to 40 eV. In transport coefficient in Eq.(6.6) is assumed neoclassical. However, electron thermal conductivity in (6.5) and diffusion coefficient in (6.7) include both neoclassical transport coefficients and anomalous transport coefficients obtained emperically. These anomalous coefficients are adjusted to reproduce the experimental plasma parameters.

For simulations of pellet injection experiments, there are two ways to introduce density increase and temperature decrease in the 1-D transport code. One is the ablated pellet particles are regarded as the particle source term in the corresponding mesh region by assuming that are ionized instantly and that pellet particles become electrons and ions on the same flux surface. The other is that plasma density increases through the interaction between electrons and neutral particles by considering the pellet is the source for neutrals[56]. Depending on the selection, the radial diffusion velocity of supplied particles due to the pellet may be different. If we adopt the latter way, for example, the

ablated particles fly through the plasma as neutrals. In a real plasma, almost all ablated particles are ionized immediately and confined within the magnetic surface, and the others fly across the magnetic surface as neutrals. In the present study concerning high temperature target plasmas, we adopt the former way.

For pellet ablation calculation, we use ABLATE introduced in chapter 5. In this code, several ablation models are implemented for ablation rate calculation according to situations. If we consider the 'self-limiting ablation' mechanism[51], the changes of electron density and temperature are given simultaneously by this code. For ion temperature, we assume the adiabatic change and calculate ion temperature profile after the pellet injection, $T_i(new)$, from $T_i(new)=n_i(old)T_i(old)/n_i(new)$, where charge neutrality $n_i=n_e$ is used. These plasma parameters just after the pellet injection are taken into account as initial values for next time step calculation in the transport code, since a pellet life-time and time scale for change of plasma parameters due to the pellet ablation are much shorter than the characteristic time for plasma transport.

When we calculate the transport for Heliotron E in chapter 7, we will modify the above 1-D tokamak transport code. Heliotron E is not a tokamak-type device but the toroidal helical device with a helical coil wound around the vacuume chamber producing both toroidal and poloidal magnetic fields. In 1-D transport calculation only the rotational transform produced by the helical coil winding is included. Thus, for Heliotron E, the plasma is approximated by a circular cross-section with an averaged radius and the poloidal magnetic field produced by the helical coil, B_p^h, and that by the

plasma current, B_p^{OH} (in the case of Ohmic heating). The former poloidal magnetic field is calculated from the rotational transform profile produced by the helical coil, $\iota^h(r)$, as

$$B_p^h(r) = B_t r \iota^h(r)/R_0$$
$$= \frac{B_t r}{R_0}\{\iota_0 + (\iota_a - \iota_0)(\frac{r}{a})^4\}, \qquad (6.8)$$

where $\iota_0=\iota^h(0)$, $\iota_a=\iota^h(a)$, B_t is the toroidal magnetic field produced by the helical coil, and R_0 is the major radius. In the present study, we took $\iota_0=0.55$ and $\iota_a=2.5$. Equation (6.4), therefore, is used only for B_p^{OH} and the total poloidal magnetic field in transport coefficients is given by a summation of B_p^{OH} and B_p^h . In the calculation for Heliotron E in chapter 7, ripple transport and radial electric field on the transport are neglected, since collisionality is estimated in the plateau regime. When the Ohmic current is zero (called as current-free plasma), the plasma is maintained only by the external rotational transform, ι^h . In the simulations, we took into account the observed small toroidal current in Heliotron E instead of completely current-free plasma, but its contribution to confinement and heating is negligible[57] .

6.3 Transport study of pellet injection experiments in ISX-B

We will analyse a pellet injection experiment in the ISX-B tokamak device[12] by the 1-D tokamak transport code explained in section 6.2. The ISX-B tokamak plasma has a major radius of 0.92 m and a minor radius of 0.27 m. Calculations were carried out for an experiment of pellet injection into low density Ohmic heating plasma with the line averaged density of $10^{19}m^{-3}$, the toroidal magnetic field of 1.51 T, and the plasma toroidal current of 110 kA. An H_2-pellet which consists of 3.2×10^{19} atoms was injected at a velocity of 900 m/s.

Transport coefficients in Eqs.(6.5), (6.6), and (6.7), or diffusion coefficent for particles, D, electron thermal conductivity, κ_e, and ion themal conductivity, κ_i are given as

$$D = D^{neo} + D^{ano} ,$$

$$\kappa_e = n_e\chi_e = \kappa_e^{neo} + \kappa_e^{ano} ,$$

$$\kappa_i = n_i\chi_i = \kappa_i^{neo} ,$$

where transport coefficeints with superscripts of neo are calculated from the neoclassical theory[58] and those with ano are anomalous transport coefficients. We assume the anomalous transport coefficients will obey the empirical Alcator-like scaling,

$$D^{ano} = C_1/n_e ,$$

$$\kappa_e^{ano} = C_2 n_e D^{ano} .$$

Here C_1 and C_2 are adjusted so as to reproduce the experimental plasma parameters just before the pellet injection and we took

C_1=5.5×10[18] and C_2=2.1 for the example of ISX-B tokamak.

Now, the result of the numerical calculation are explained. Figure 6.1 shows the ablation rate profile calculated from ABLATE with Milora-Foster model[19] and electron density and temperature profiles at different times. The origin of the time shown in the figure for the electron density and temperature profiles is the pellet injection time. For example, the Fig.6.1(b) signified TIME = -2 ms denotes the electron density and temperature just before the pellet injection. Fig.6.1(a) show the ablation rate profile of the pellet injected into the plasma in Fig.6.1(b). In experiments of pellet injections into low density Ohmic heating plasmas of ISX-B, it was shown that the lifetime of the pellet in a plasma becomes smaller than that predicted by the Milora-Foster model due to the presence of runaway electrons[12]. Here, since our main purpose is examining transport process after the pellet injection, we use a pellet injection velocity of 500 m/s in this simulation and adjust the penetration length of the pellet to the experimental value. The effect of runaway electrons can be examined by our model in chapter 3 and a typical example is shown in section 4.3. Since the pellet cannot reach to the magnetic axis, the density profile just after the pellet injection shows a hollow profile and the electron temperature profile just after the pellet injection becomes peaky. These profiles gradually recover the original bell-shaped profiles through the transport process during 20 ms after the pellet injection. When we compare the numerical result to the experimental data of electron density profile 1.7 ms after the pellet injection, The peak of density profile around r=7 cm seems to be broader in the experiment than that in the simulation (see Fig.6.1(c)). If

it is meaningful, it is conjectured that the ablated pellet particles fly in a plasma as neutrals and expansion of the density becomes more rapid than our result. Then, a volumetric source of particles extended spatially is more appropriate than the point source assumed in the numerical model. From the measurements of the ablation cloud surrounding the pellet with visible light, it was shown that the ablation cloud spread over 5 cm width, and there is a possibility that the ablated particles becomes fully ionized in the region far from the pellet surface. It is not easy to examine the volumetric particle source in the ablation model, and this will be a future problem.

There is another difference between the experimental result and the numerical result. The recovery of the central electron temperature in Fig.6.1 is a little slower than that of the experimental result. This might be related to the improvement of the electron energy confinement after the pellet injection, but this is not clear. Though there are some small quantitative differences mensioned above, the time evolutions of the plasma parameters after the pellet injection by our code agree well with the experimental data without change of the transport coefficients. It is summarized that the transport phenomena do not change by the pellet injection in this ISX-B experiment.

Next, we show the volume averaged electron density, the central ion temperature, the loop voltage, and energy confinement time in Fig.6.2. Typical characteristics are that total number of plasma particles increases three times, volume averaged electron temperature decreases by factor 3, and central ion temperature increases by factor 1.5 after the pellet injection. Main reason for

increase of the central ion temperature is that energy transfer from electrons to ions through collisions is enhanced by the density increase due to the pellet injection. The increase of the loop voltage after the pellet injection is related to the increase of plasma resistivity due to the electron temperature decrease. Also the energy confinement time τ_E increases accompanied by the density increase, which is understandable from the Alcator confinement scaling. Here we define the energy confinement time by

$$\tau_E \equiv \frac{Q}{W_J - dQ/dt} \ , \tag{6.9}$$

where Q designates total heat content of plasma and W_J denotes total heat power due to the Ohmic heating. These results also agree well with the experimental results in ISX-B tokamak.

6.4 Conclusion

We described the transport code including the pellet injection to investigate transport properties after the pellet injection. By the application of the transport code to a pellet injection into an Ohmically heated plasma in ISX-B tokamak, it is found that this transport code can reasonably simulate a pellet injection experiment in ISX-B. It seems that transport phenomena do not change by the pellet injection in this experiment, and energy confinement time increases according to the Alcator scaling. The increase of the central ion temperature can be explained by the enhancement of energy transfer from electrons to ions through collisional coupling due to the density increase after the pellet injection.

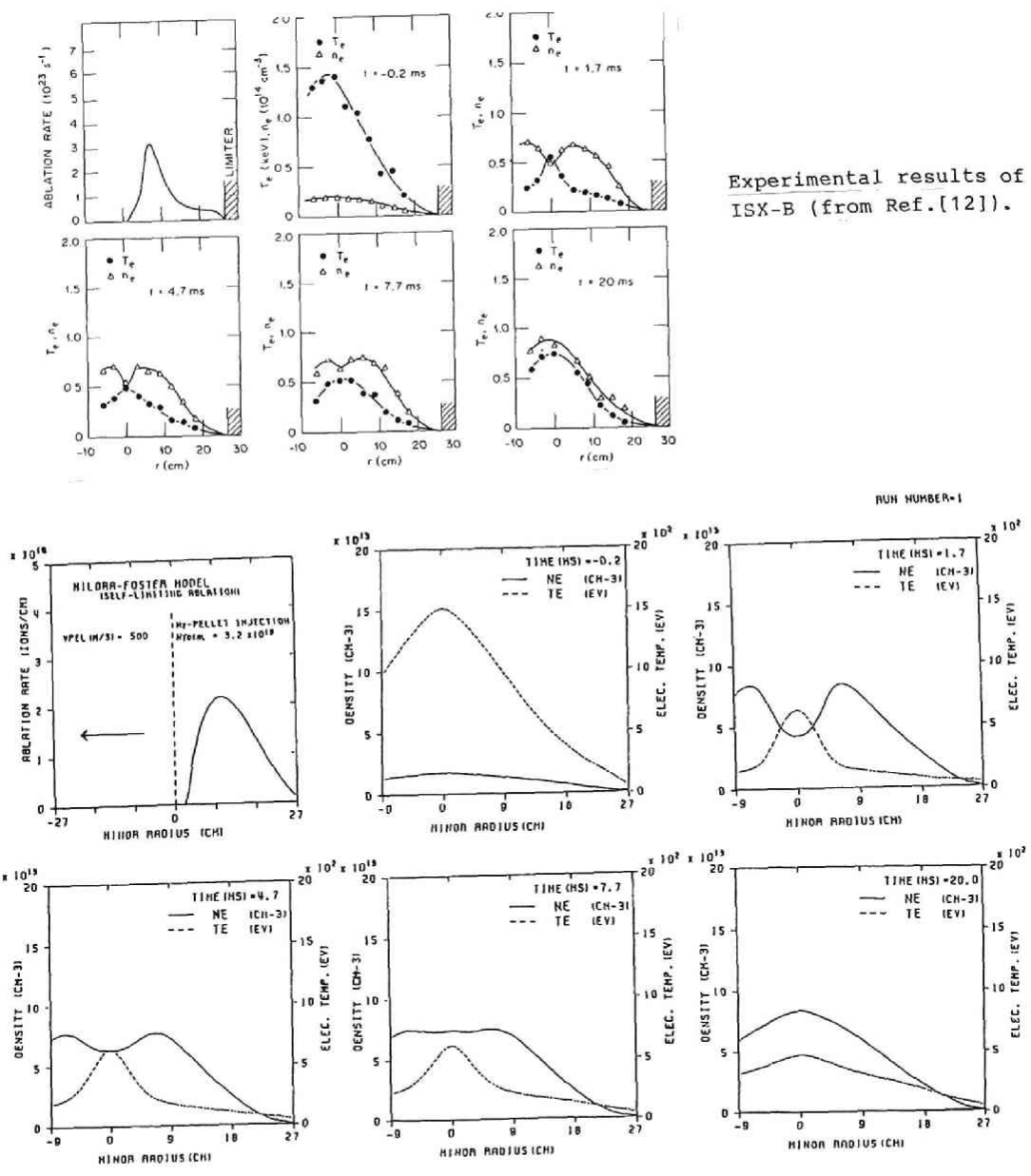

Experimental results of ISX-B (from Ref.[12]).

Fig.6.1. Ablation rate profile and time evolutions of electron density and temperature profile obtained by transport analysis of pellet injection into ISX-B plasma.

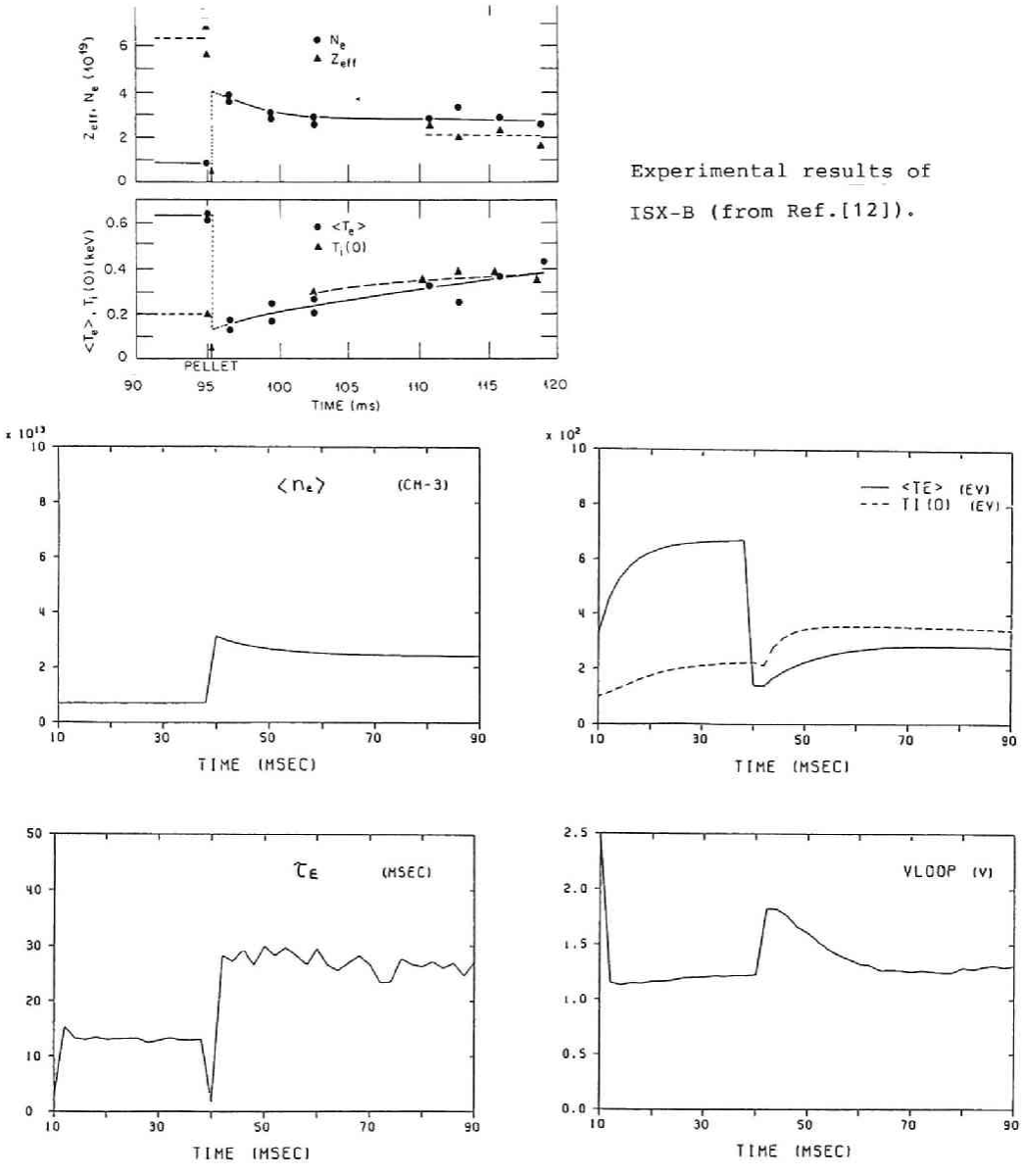

Fig.6.2. Time history of volume-averaged density, volume-averaged electron temperature, central ion temperature, and loop voltage calculated from transport simulation of ISX-B. Pellet is injected at 40 ms.

CHAPTER 7

Analyses of Pellet Injection Experiment in Heliotron E

7.1 Introduction

In Heliotron E, current-free discharges were realized by a combination of ECRH (electron cyclotron resonance heating) and NBI heating. Pellets were injected into such current-free plasmas. In the analysis of the pellet ablation, therefore, the effect of fast ions must be taken into account. We will discuss the ablation profile of the pellet injected into an NBI heated plasma in section 7.2. The ablation rate profile is calculated by using our model and is compared to the experimental results. Numerical results by using other models are also discussed. In these calculations, an elliptic cross-section of the Heliotron E plasma is taken into account for quantitative comparison.

In section 7.3, we will examine the effects of the pellet injection on the transport properties for the Heliotron E plasma. Here we discuss both the model transport calculation for the pellet injection into an Ohmically heated plasma and the transport simulation of the pellet injection experiment into an NBI heated current-free plasma.

In the high β experiment of the NBI heated current-free plasma with the pellet injection, sometimes density fluctuations were observed. In section 7.4, we will discuss stability against interchange modes in a pellet injected current-free high β plasma

by solving reduced MHD equations.

7.2 Study of ablation rate profile

We examine the pellet ablations injected into both high power and low power NBI heated plasmas with the velocity of 580 m/s. In the high power NBI heated plasmas with a magnetic field B=0.94 T, the central electron density is about 4×10^{19} m^{-3} and the central electron temperature is 300 eV ~ 400 eV before the pellet injection. For the low power NBI case, the central electron density is about 3×10^{19} m^{-3} and the central electron temperature is 200 eV ~ 300 eV. For both cases, it is observed that profiles of electron temperature and density before the pellet injection are broad, penetration lengthes of both pellets are almost the same, and they cannot reach to the magnetic axis.

First, we calculate the ablation rate for high power NBI case. Injection energy of the neutral beam is 26 keV. A pellet size injected into the plasma is estimated from the average density increment, $\Delta n_e \sim 2.5\times10^{19}$ m^{-3} , and a radius of 0.577 mm is given (it contains about 4.28×10^{19} atoms). Profiles of the fast ion density, n_f , the electron density, n_e , and the electron temperature, T_e , are given by

$$n_f = 2\times10^{18}\{1-(r/a)^3\}^2 \quad (m^{-3}) ,$$

$$n_e = 4\times10^{19}\{1-(r/a)^{10}\} \quad (m^{-3}) ,$$

$$T_e = 400\{1-(r/a)^6\} \quad (eV) ,$$

where we take broad profiles for electron density and temperature in accordance with the experiment. Their volume averaged values are $\langle n_f \rangle \sim 9\times10^{17}$ m^{-3} , $\langle n_e \rangle \sim 3.3\times10^{19}$ m^{-3} , and $\langle T_e \rangle \sim 300$ eV. The representative fast ion energy and heat flux are obtained from

moments of the distribution function by using Eqs.(4.18) to (4.20). For the above electron density and temperature, the slowing-down time of fast ions, τ_s, is about 6 ms and the NBI power deposited to the plasma is estimated as

$$P_{NBI} \sim eN_f E_{NBI}/\tau_s \sim 1060 \text{ kW},$$

where N_f denotes total number of fast ions at steady state. In the ablation rate calculation, we assume that the pellet path length to the magnetic axis is 0.3 m to take the elliptic shape of Heliotron E plasma into account. Results from the ABLATE code in the case of our ablation model are shown in Fig.7.1. Fig.7.1(a) shows the pellet ablation rate profile, and Fig.7.1(b) shows the electron density profile just before (indicated with dashed line) and just after (with solid line) the pellet injection. The electron temperature profile at the same times are shown in Fig.7.1(c) with dashed and solid line. The pellet cannot reach to the magnetic axis, and a hollow electron density profile appears after the pellet injection.

Next, we calculate the low power NBI case. Neutral beam energy and pellet injection velosity are taken as the same value as those in the higher power case. A pellet radius is 0.524 mm and the pellet contains about 3.2×10^{19} atoms which corresponds to $\Delta n_e \sim 1.9\times10^{19}$ m^{-3}. Profiles of the fast ion density, n_f, the electron density, n_e, and the electron temperature, T_e, are given by

$$n_f = 7\times10^{17}\{1-(r/a)^8\}^2 \quad (m^{-3}),$$
$$n_e = 3\times10^{19}\{1-(r/a)^6\} \quad (m^{-3}),$$
$$T_e = 280\{1-(r/a)^8\} \quad (eV).$$

Their volume averaged values are $\langle n_f \rangle \sim 5\times10^{17}$ m^{-3} , $\langle n_e \rangle \sim 2.25\times10^{19}$ m^{-3} , and $\langle T_e \rangle \sim 220$ eV. Deposited beam power to the plasma is estimated approximately 600 kW. The results are shown in Fig.7.2. Compared to Fig.7.1, the effect of the fast ions on the ablation becomes more significant in the edge region of the plasma and the resultant electron density profile becomes broader than that of the high power case. These results seems to be consistent with the experimental results. Numerical results from the Parks and Turnbull model, and the Milora model for the high power case are shown in Fig.7.3. Figure 7.3(a) shows the result without the effect of fast ions on the ablation (PT model). The longer penetration length is obtained than the experimental result. On the other hand, Fig.7.3(b) shows the case including the effect of fast ions on the ablation (Milora model) and the shorter penetration length is obtained. Although uncertainty of the spatial distribution of fast ions remains, our model gives more reasonable results to explain the experimental data than the Milora model.

7.3 Transport analysis after the pellet injection

In this section, we analyse transport properties in the Heliotron E plasma after the pellet injection by using the 1-D transport code described in section 6.2. Since main purpose of this study is to examine the effect of the pellet injection on the transport properties, we will calculate several model problems.

First, in order to examine the effect of Ohmic current on the transport after the pellet injection, we have done model calculations for the pellet injection into an Ohmically heated plasma. In these simulations the following parameters are given: major radius, 2.2 m, minor radius, 0.2 m, magnetic field at the magnetic axis, 1.98 T, and Ohmic current, 30 kA. An H_2 pellet which contains 4.2×10^{19} atoms is injected at a velocity of 800 m/s. The ablation rate of the pellet by the Milora-Foster model is shown in Fig.7.4 and time evolutions of electron temperature, density, and toroidal current density profiles are shown in Fig.7.5. Total number of plasma electrons before the pellet injection is 5.1×10^{19}. Since electron temperature is low before the pellet injection, the pellet does not ablate completely inside the plasma column and number of pellet particles ablated in the plasma column is only 4×10^{19}. The volume averaged electron density increases up to 5×10^{19} m^{-3} after the pellet injection from 2.9×10^{19} m^{-3} before the injection. Owing to the self-limiting ablation introduced in section 5.2, ablation rate at the magnetic axis is depressed. When a pellet passes through the magnetic axis, it has a tendensy that a pellet goes through out the plasma column, since it meets the background plasma with lower temperature cooled by the pellet

ablation before reaching to the magnetic axis. It is seen that just after the pellet injection, the electron density has a peaked profile at the magnetic axis, and electron and ion temperatures have hollow profiles. Such profiles are sustained for 20 ms and recovery of the temperature is slow. Because of the low Ohmic current, the Ohmic heating power to heat the high density plasma is not enough. Since Spitzer resistivity is proportional to $T_e^{-3/2}$, the current density profile also becomes hollow according to the electron temperature with a time scale of the plasma skin time after the pellet injection. Ohmic heating power to electrons, therefore, becomes maximum around r=0.1 m and the electron temperature has a broader profile than that before the pellet injection at steady state. Since the density before the pellet injection is rather high and a difference between the electron and the ion temperature is small in this case. After the pellet injection, the ion temperature does not recover the value before the pellet injection, which is similar to the pellet injection experiment of ISX-B discussed in section 6.3. The time evolution of the ion temperature is almost the same as that of the electron temperatre.

Figure 7.6 shows time evolution of electron temperature, density and current density in the case of slower pellet injection velocity of 200 m/s. Because of slow injection velocity, pellet cannot reach to the magnetic axis. Therefore, the electron density has a hollow profile just after the pellet injection and broad density profile is obtained at steady state after the pellet injection. On the other hand, profiles of the electron temperature and the current density become peaky. Since shrinkage of the

current channel may induce current-driven instability even in Heliotron E[59], edge cooling of the plasma due to the pellet injection may affect the plasma stability.

Next, we calculate a pellet injection into an NBI heated current-free plasma. In this case, magnetic field is 1.9 T at the magnetic axis and total NBI power is 1.4 MW. In the Heliotron E experiments, the current-free plasma is firstly produced by ECRH and heated by the following NBI. In the numerical calculation, however, an initial plasma with the toroidal current of 10 kA is given. It is heated by NBI during decreasing the plasma current, and almost current-free plasma with the total plasma current of 0.5kA sustained by NBI is obtained in the numerical simulation. Although, neutral beams are injected almost perpendicularly into a plasma in Heliotron E, we assume tangential injection in the numerical model in order to use the Fokker-Planck equation for calculating an energy deposition profile by NBI. A pellet consists of 4.2×10^{19} H-atoms is injected at 150 ms with the injection velocity of 1 km/s. The ablation rate profile and change of electron density and electron and ion temperature profiles by the pellet injection are shown in Fig.7.7. Total number of plasma electrons are approximately 5×10^{19}. In the NBI heated current-free plasma in Heliotron E, heat source is fast ions produced in a plasma by the neutral beam and a birth profile of fast ions is a principal factor to determine the plasma temperature profile. The plasma temperature profile is broad before the pellet injection (at 145 ms), and this becomes further broader at 30 ms after the pellet injection. The reason is that the fast ion birth profile is broad or hollow accompanied by the decrease of the mean free path

due to the density increase. In accordance with this, profile of deposited power from fast ions to electrons and ions becomes flat. In Fig.7.8, histories of significant plasma parameters are shown. The volume averaged electron density, $\langle n_e \rangle$, increases doubly from 2.5×10^{19} to 5×10^{19} m^{-3}. Large increase of the central electron density at the pellet injection means that the pellet exceeds the magnetic axis. Recovery of the temperature is faster than that in the case of Ohmically heated plasma, since fast ions are thermalized rapidly and give thier energy to both electrons and ions efficiently just after the pellet injection. Fig.7.9 shows the power balance of fast ions. At the pellet injection time of 150 ms, there is no change of the deposited power. However, energy transfer from fast ions to the background plasma especially to electrons increases considerably, since fast ions thermalized quickly due to both the rapid increase of the plasma density and the decrease of electron temperature. The characteristic time for thermalization of fast ions, or Spitzer's slowind-down time, is about 15 ms at the plasma center before the pellet injection, and it becomes less than 3 ms after the pellet injection. Another result in Fig.7.9 is decrease of charge-exchange energy loss of fast ions. About one third of input power to fast ions is lost by charge-exchange reaction with thermal neutrals before the pellet injection. When the plasma density increases by the pellet, thermal neutrals are ionized rapidly and the density of thermal neutrals decreases. Furthermore, since the ion temperature decreases by the pellet injection, the energy of neutrals becomes low. This means that the mean free path becomes short and neutrals arrived at central region from the edge decrease. The charge-exchange loss of fast ions,

therefore, decreases after the pellet injection by the decrease of neutrals. The change of pressure profiles by the pellet injection are shown in Fig.7.10. Just after the pellet injection, pressure has a highly peaked profile at the magnetic axis. The density increases and the temperature decreases considerably at the plasma center in accordance with the self-limiting ablation, which is based on the adiabatic process. The peaked part of the pressure profile shows a deviation from the adiabatic low. This may be explained by that rapid thermalization of fast ions and increased energy flow from fast ions to the background plasma is taken place at the plasma center. At 30 ms after the pellet injection, the pressure profile recovers a bell-shape, but pressure gradient becomes larger on the whole regime than that before injection. Pressure diven instabilities related to these pressure profiles will be discussed in the next section. If we need broader pressure profile than that Fig.7.10, slower pellet injection is available. With an injection velocity of 500 m/s, a pellet cannot reach to the magnetic axis and hollow electron density profile appears just after the pellet injection. Behaviors of macroscopic plasma paramters are almost the same as the case with the injection velocity of 1 km/s, but the obtained pressure profile becomes broader than that of Fig.7.10 as shown in Fig.7.11.

7.4 MHD stability related to the pellet injection

In toroidal plasmas without net current in stellarator/heliotron type configuration, the dominant driving force of MHD instabilities is a pressure gradient. In a heliotron configuration with a high shear and a rotational transform above unity at the edge, low m interchange modes can be unstable for increasing β value.

It was demonstrated that central plasma density was effectively by the pellet injection instead of the gas puffing. An interesting result is that the density fluctuations were observed only after the pellet injection.

We study the linear stability against the ideal and the resistive interchange modes for the pressure profile produced by the pellet injection[10]. The β limit due to the pressure driven low m modes is estimated. We solve the reduced MHD equations derived by using the stellarator expansion as an initial and boundary value problem for resistive cylindrical plasmas[60),61)]. The equations are linearlized and the time evolution of the perturbation is calculated for fixed boundary condition. When the perturbation grows exponentially, a linear groth rate and an eigen mode are obtained.

In the equilibrium, a very small current with a parabolic profile with $\iota^J(a)=0.05$ is included, where $\iota^J(a)$ denotes a rotational transform due to plasma current at the plasma surface. It is checked that this current does not bring about any current-driven mode. The resistivity profile is chosen as $\eta(r)\propto 1/j(r)$, where $j(r)$ is the plasma current density profile. The

profile of the external rotational transform ι^h is chosen as $\iota^h(r)=0.51+1.69(r/a)^{2.5}$. The rational surface, $\iota^J+\iota^h=n/m$, for the m=3/m=2, m=1,n=1, and m=2/n=3 modes are r/a=0.26, 0.57, and 0.78, respectively.

Two cases of pressure profiles shown in Fig.7.10 are used for the present study. The pressure profile except for the peaked part in the central region just after the pellet injection (case 1) is broader than that of 30 ms after the pellet injection (case 2).

The linear growth rate γ for the m=1/n=1 pressure driven mode in the case 1 are shown in Fig.7.12(a) for various S value, where S denotes the magnetic Reynolds number measured by the poloidal magnetic field. The abscissa denotes the central beta value $\beta(0)$. The β limit for the ideal m=1/n=1 mode seems $\beta(0)\sim3.5$ % in case 1. Its value is estimated from the extrapolation by assuming the relation that γ^2 is proportional to $\beta(0)$ near the marginal state. Below this value the m=1/n=1 mode is destabilized by the resistivity. For $\beta(0)\sim7$ %, the growth rates are almost independent of S.

Figure 7.12(b) shows the growth rates for the m=3/n=2 mode in the case 1. The ideal beta limit of m=3/n=2 mode is about $\beta(0)$=2.5%. However, the increment rate of γ with the increase of $\beta(0)$ is smaller for the m=3/n=2 ideal mode than that for the m=1/n=1 ideal mode. The growth rates for the resistive modes of the m=1/n=1 and the m=3/n=2 are comparable.

We have also done the stability calculation for the m=2/n=3 mode in the case 1. It is found that the m=2/n=3 ideal mode is linearly stable till $\beta(0)\sim7$ % and that the growth rates of the resistive modes are smaller by a factor ~2 than those of the

m=1/n=1 and the m=3/n=2 modes.

Figure 7.13(a) and (b) show the growth rates for the m=1/n=1 and m=3/n=2 modes, respectively, in the case 2. The ideal β limits are $\beta(0)\sim2.5\,\%$ and $\beta(0)\sim1.5\,\%$ for the m=1/n=1 and the m=3/n=2 modes, respectively. In Fig.7.13(a), the growth rates are almost independent of S for $\beta(0)\sim4\,\%$. We find that the structures of the resistive modes coincide with that of the ideal mode for three modes, the m=1/n=1, m=3/n=2, and m=2/n=3, in the case 2. The m=2/n=3 ideal mode is linearly stable for $\beta(0)<4\%$.

The pellet injection experiments of Heliotron E show that the density fluctuations with the asymmetry around the central chord corresponding to the odd modes appear only after the pellet injection. The experimental pressure profile is between the case 1 and the case 2. And the experimental threshold value of $\beta(0)$ for the appearance of the fluctuations seems to be 1.0 to 1.5%. By comparing these data with our results, both the m=1/n=1 and the m=3/n=2 modes become candidates to explain the experiments in the framework of the linear stability analysis.

7.5 Conclusion

The ablation rate calculation of the pellet injected into an NBI heated plasma in Heliotron E by the ABLATE code demonstrated results consistent with the experiments. The effect of fast ions on the pellet ablation in the edge region of the plasma is shown, and the broad density profiles are obtained after the pellet injection. In the application to PDX, the Milora model predicts a shorter penetration depth than that by the ABLATE code.

In the transport analysis by using the 1-D transport code, the pellet injection into an Ohmically heated plasma in Heliotron E at the velocity of 800 m/s results in a centrally peaked density profile, a hollow electron temperature profile, and a hollow current density profile, which are maintained for 20 ms. In contrast, at the case of slower pellet injection or when the pellet cannot reach to the magnetic axis, profiles of the electron temperature and the current density become peaky. A shrinkage of the current channel due to the slower pellet injection into the Ohmic heating plasma has a possibility to induce a current-driven instability even in Heliotron E.

From the calculation of the pellet injection into an NBI heated current-free plasma, faster recovery of the decreased temperature by the pellet ablation than that in the case injected into an Ohmically heated plasma is obtained because of the rapid thermalization of fast ions. Increase of the plasma density by the pellet injection results in a broad birth profile of fast ions. Accordingly the broad temperature profile is obtained by the heating due to fast ions. In the case of deep pellet injection

beyond the magnetic axis, pressure profile after the pellet injection becomes peaky.

The linear stability analysis against the ideal and the resistive interchange mode suggests that a peaked pressure profile at 30 ms after the pellet injection, which obtained from the transport calculation, may be unstable for $\beta(0)>1\%$. By comparing the experimental data with our results, both the m=1/n=1 and the m=3/n=2 modes become candidates to explain the density fluctuations observed in the pellet injection experiment.

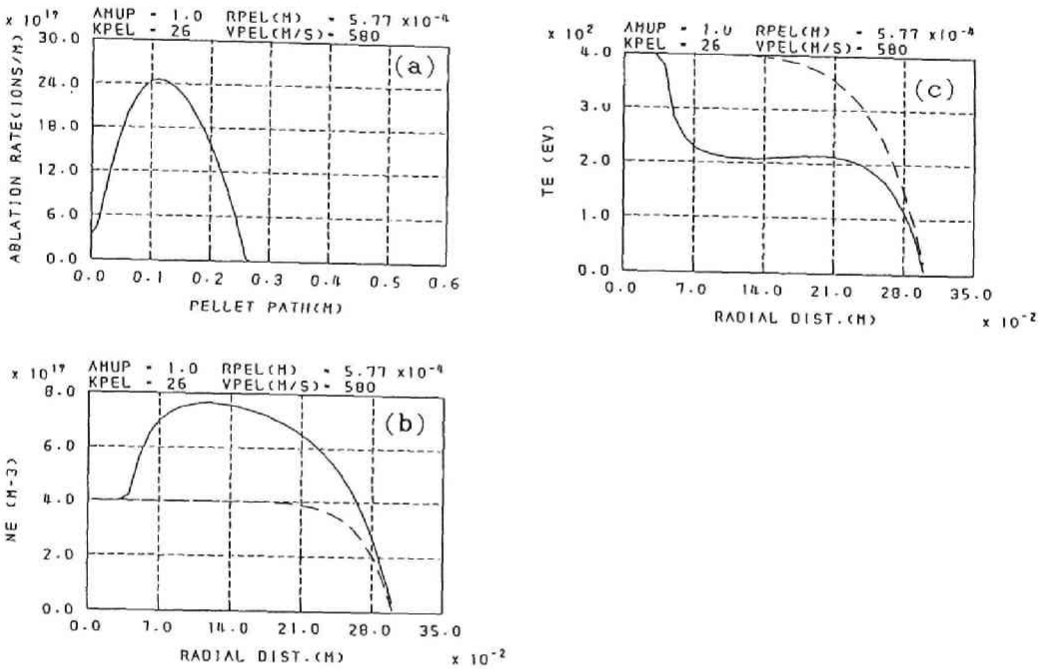

Fig.7.1 Profiles of (a) ablation rate, (b) electron density, and (c) electron temperature just before and just after pellet injection into a high-power NBI heated plasma of Heliotron E.

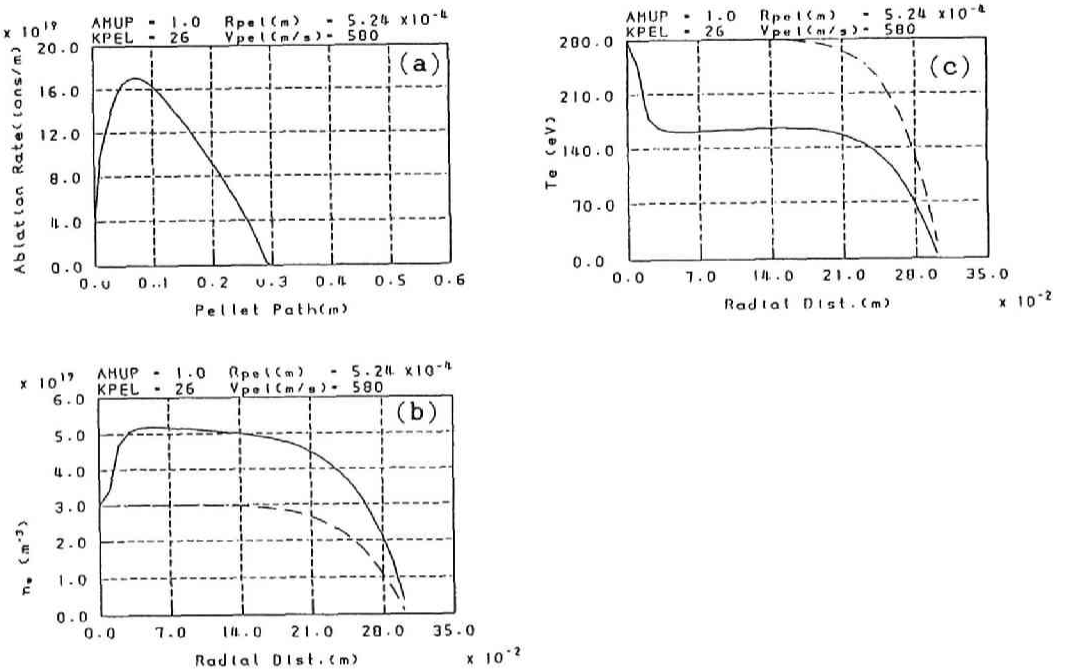

Fig.7.2. Profiles of (a) ablation rate, (b) electron density, and (c) electron temperature just before and just after pellet injection into a low-power NBI heated plasma of Heliotron E.

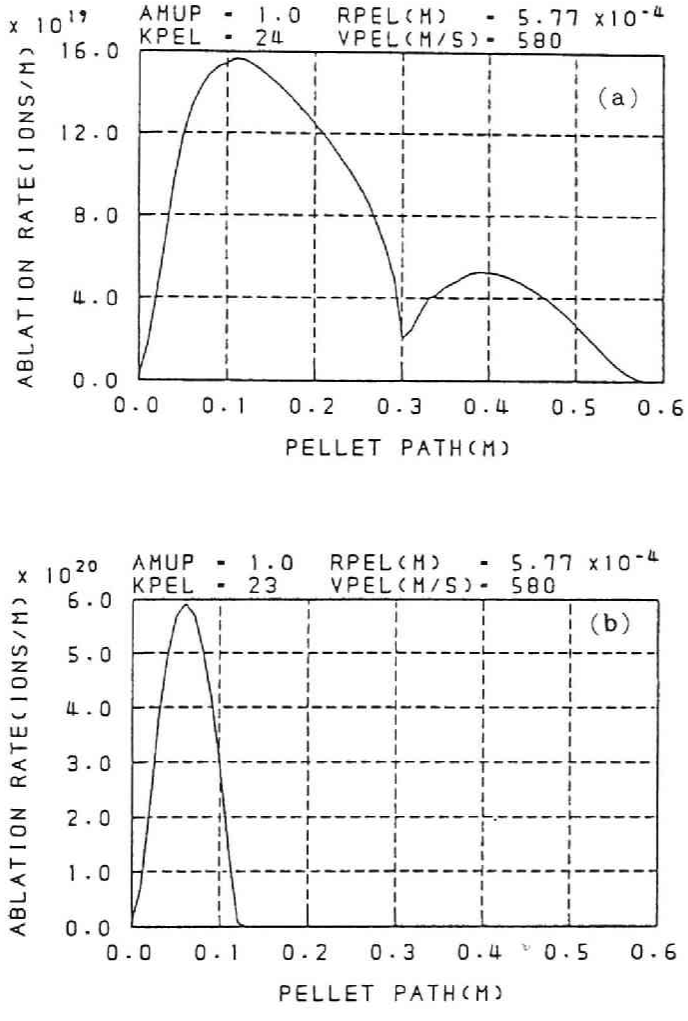

Fig.7.3. Ablation rate profiles calculated from (a) PT model and (b) Milora model for pellet injection into high-power NBI heated plasma of Heliotron E.

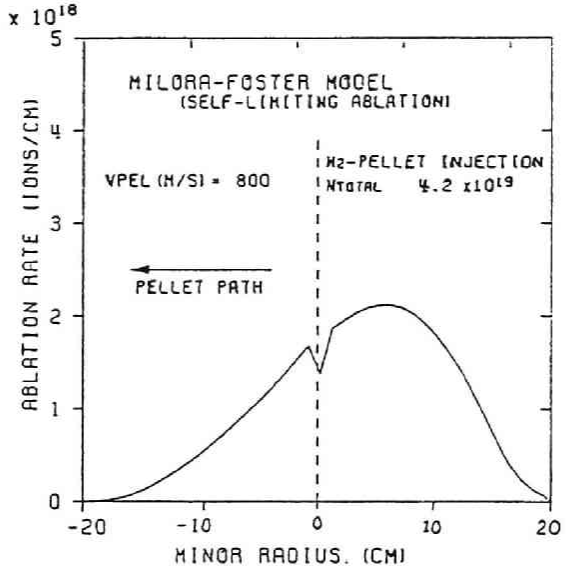

Fig.7.4. Ablation rate profile of pellet injection into Ohmically heated plasma of Heliotron E calculated from MF model.

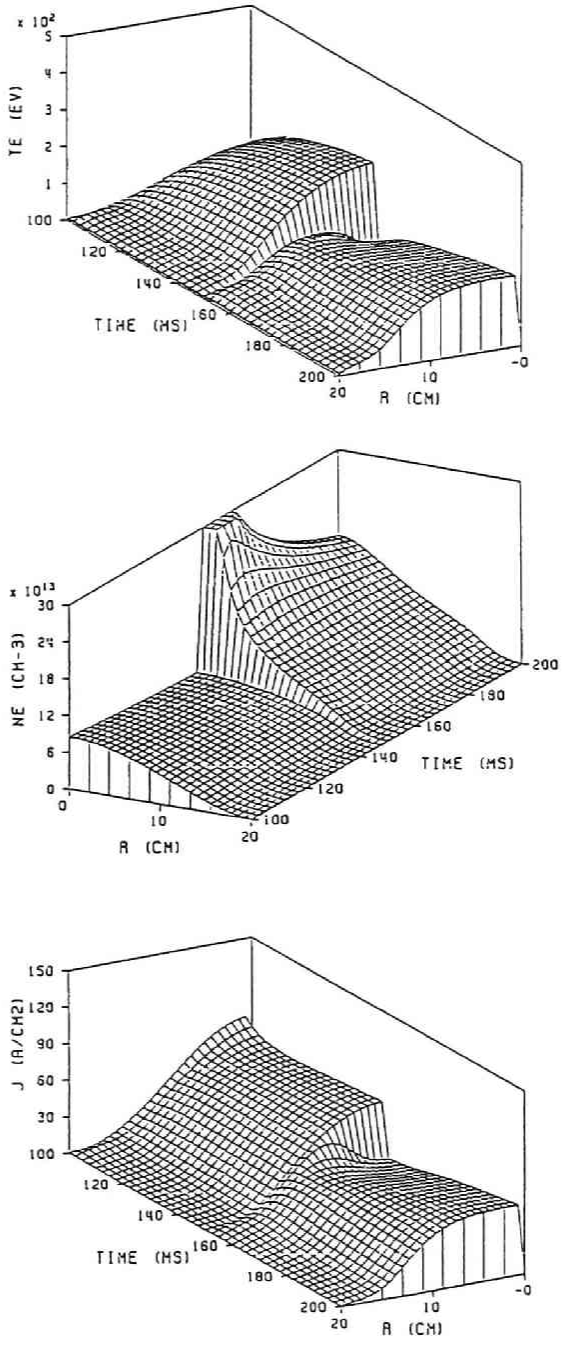

Fig.7.5. Time evolution of electron temperature, electron density, and current density profiles for pellet injection into Ohmically heated plasma of Heliotron E. Pellet is injected at 150 ms.

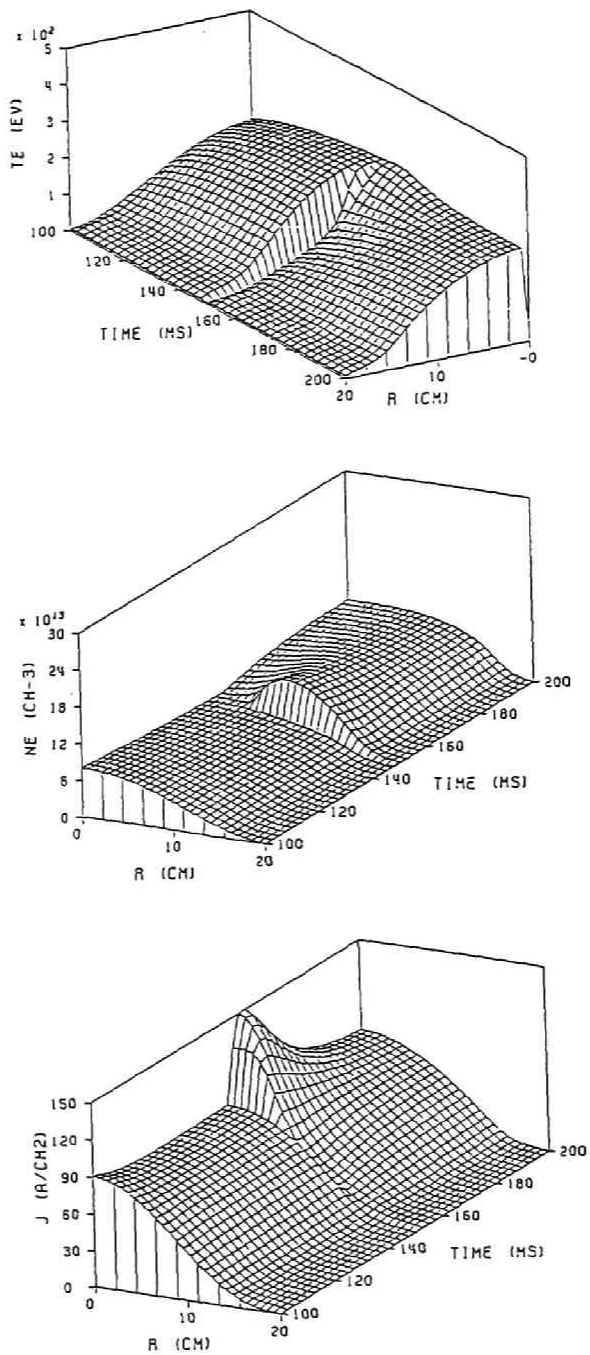

Fig.7.6. Time evolution of electron temperature, electron density, and current density profiles for slower pellet injection than that in Fig.7.5 into Ohmically heated plasma of Heliotron E. Pellet is injected at 150 ms.

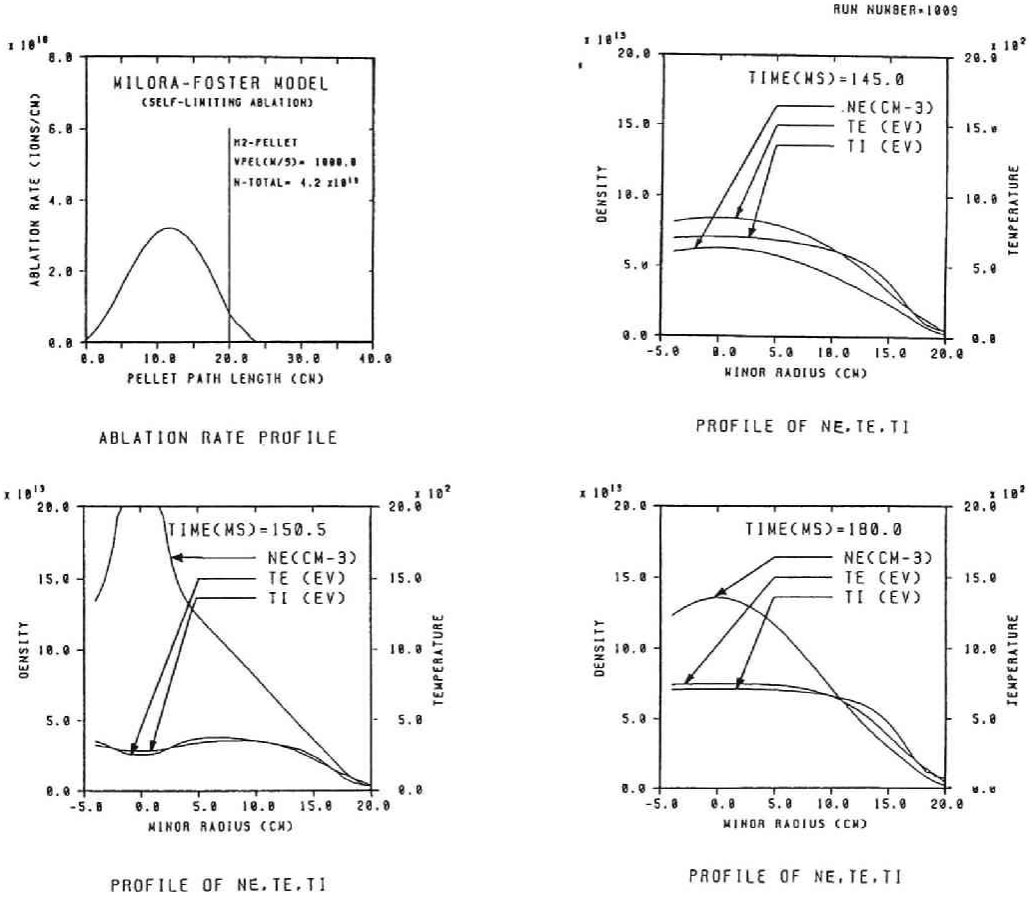

Fig.7.7. Ablation rate profile and change of electron density, electron temperature, and ion temperature profiles due to pellet injection into NBI heated current-free plasma of Heliotron E. Pellet is injected at 150 ms.

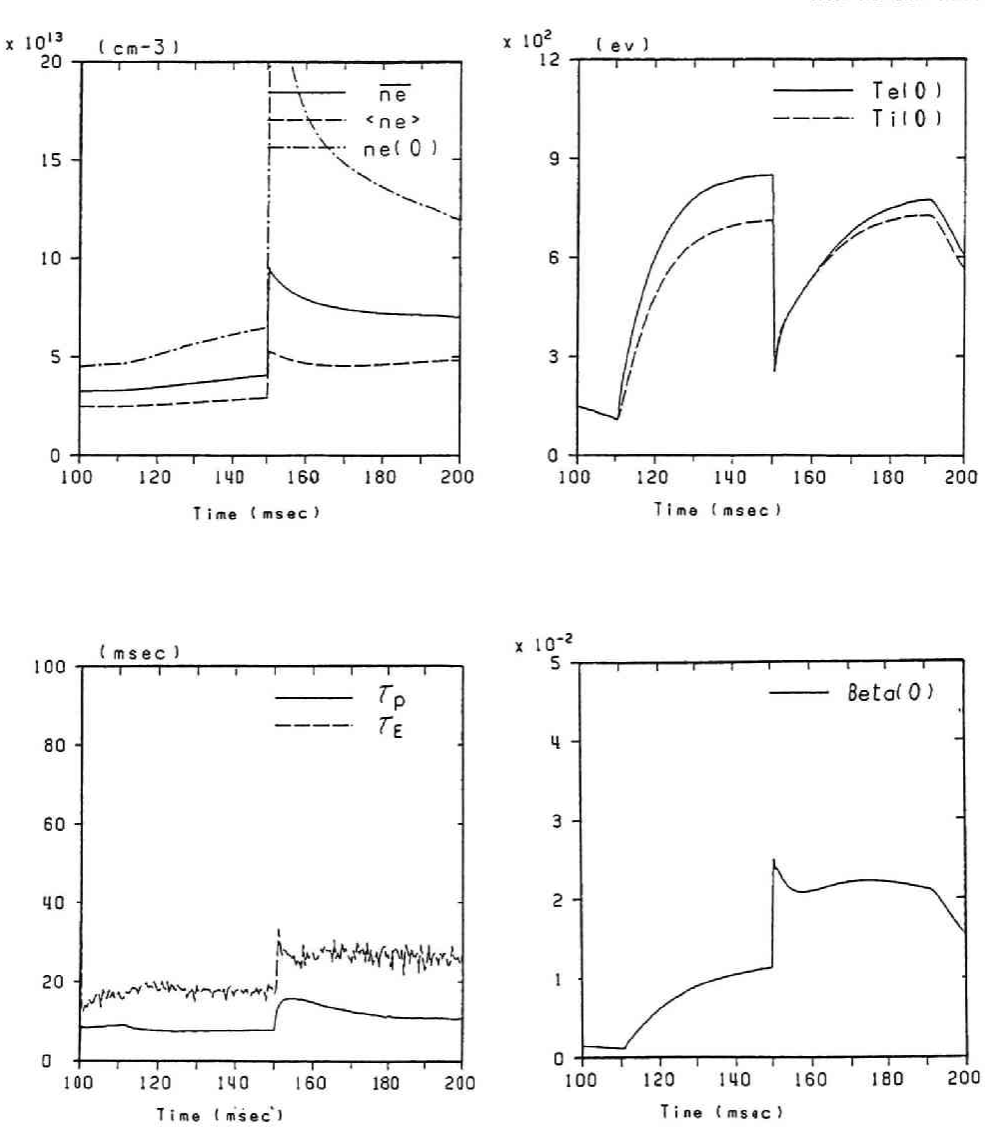

Fig.7.8. Time histories of significant plasma parameters for pellet injection into NBI heated current-free plasma of Heliotron E. Pellet is injected at 150 ms.

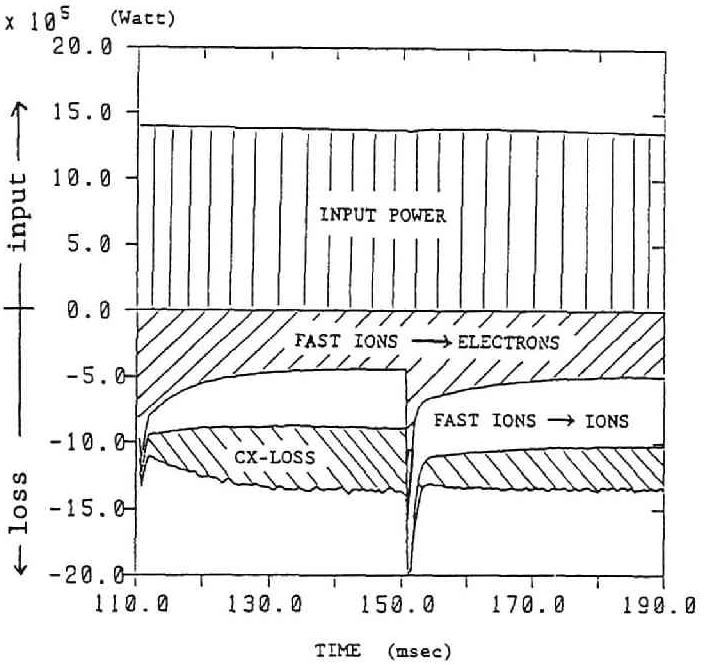

Fig.7.9. Total power balance of fast ions in the case of pellet injection into an NBI heated current-free plasma of Heliotron E. Pellet is injected at 150 ms.

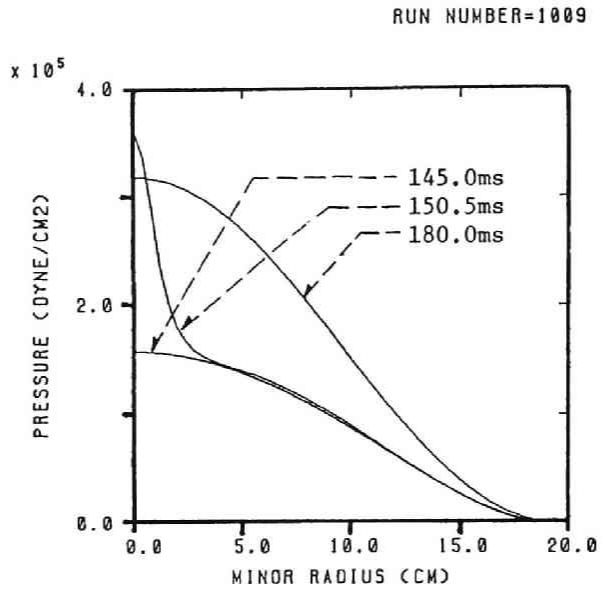

Fig.7.10. Change of pressure profiles due to pellet injection into NBI heated current-free plasma of Heliotron E. Pellet is injected at 150 ms.

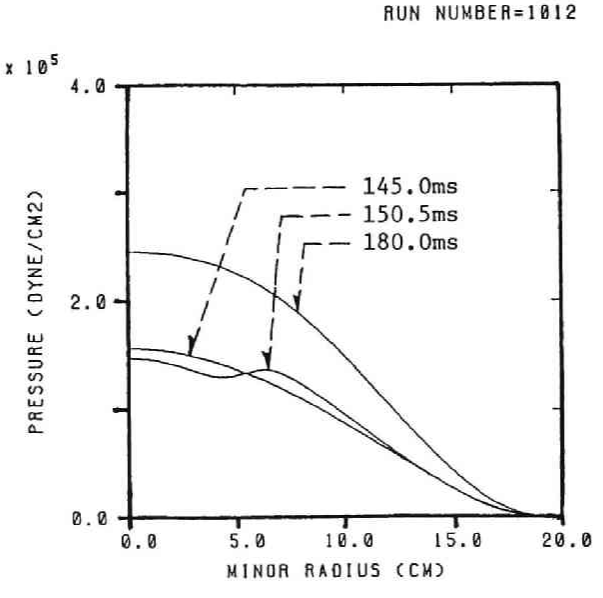

Fig.7.11. Change of pressure profiles due to pellet injection into NBI heated current-free plasma of Heliotron E, for the case pellet does not reach to magnetic axis. Pellet is injected at 150 ms.

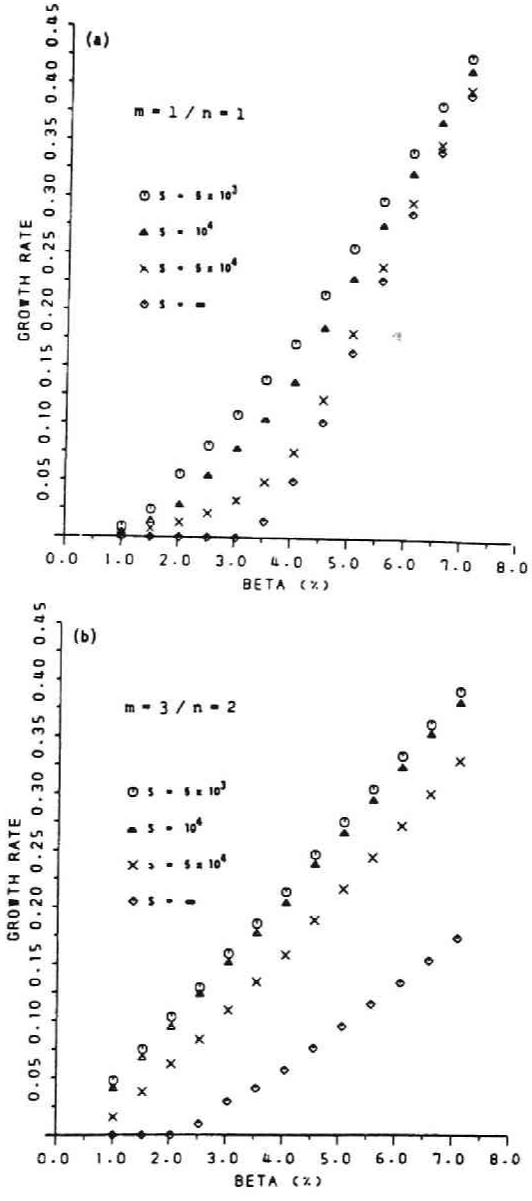

Fig.7.12. Linear growth rates of m=1/n=1 mode (a) and of m=3/n=2 mode (b) versus central beta value in the case 1.

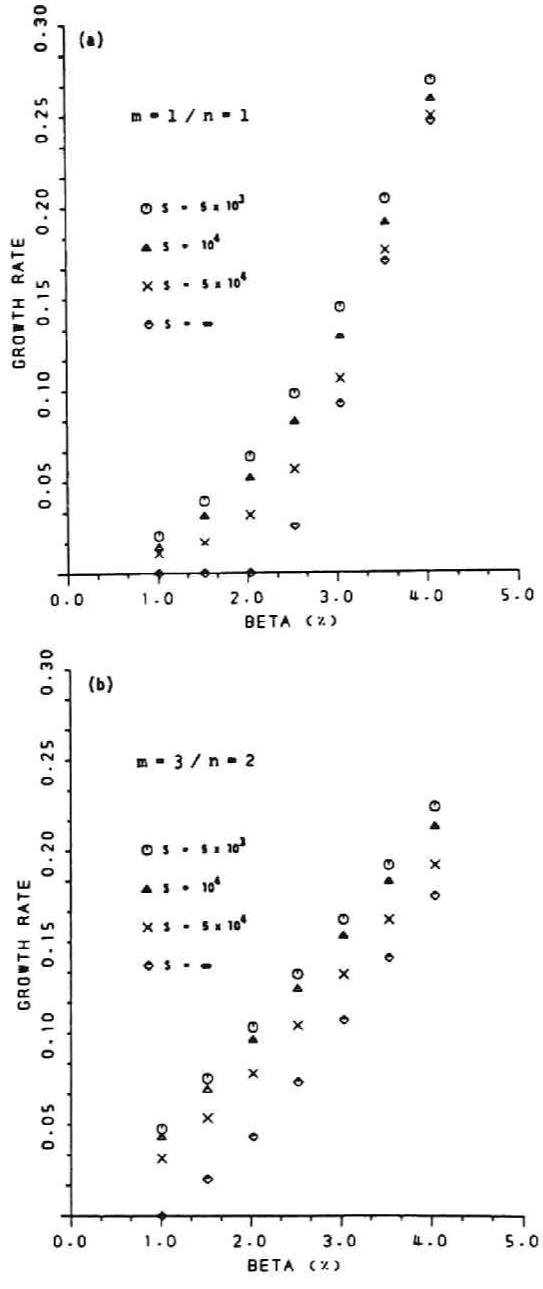

Fig.7.13. Linear growth rates of m=1/n=1 mode (a) and of m=3/n=2 mode (b) versus central beta value in the case 2.

CHAPTER 8

Possibility of Achieving $Q > 1$ by Tritium Pellet Injection into Hot-Ion-Mode Deuterium Plasmas in a Large Tokamak

8.1 Introduction

Recent Japanese large tokamak (JT-60) experiments[62] and experiments in TFTR[63] and JET[64] are progressing towards obtaining hydrogen plasmas with $T_i(0) > 10$ keV and $n\tau_E < 10^{14}$ cm^{-3} s, where n is the electron density and τ_E is the energy confinement time. One of the next important targets of fusion plasma research will be a D-T plasma experiment that satisfies $Q > 1$, Q being the ratio of total fusion output to injected power.

In order to completely investigate the physics of a reacting plasma, we need a next generation device comparable to INTOR[65]. In such a device a perfect tritium handling system will have to be installed and an amount of tritium of the order of one kilo-gram will be consumed to study the engineering aspects of a fusion reactor. Before starting such experiments, first experiments with a D-T plasma will be performed in modifications of the above large tokamaks.

As tritium is radioactive, we hope to minimize the tritium inventory in initial D-T plasma experiments aiming at $Q > 1$. For this purpose, tritium pellet injection into deuterium plasmas heated by neutral deuterium beams is considered.

Here, we assume that the neutral shielding model including

fast ions is applicable to high temperature plasmas having $T_i \sim T_e \sim 10$keV. In the ablation rate profile calculation in section 8.3, we use our ablation model including fast ions which directly solves the fluid dynamics equations describing a neutral cloud with two heat source terms, electrons and fast ions.

To investigate possibility of achieving $Q>1$, we use a transport code for multispecies ions of deuterium and tritium including D-T fusion reaction.

8.2 Description of the transport code for D-T plasma including Two-Component-Torus(TCT) effect

In the transport studies, we consider a JT-60-like large tokamak : a=0.9 m, R_0=3.0 m, B_T=4.5 T, and I_p=2.7 MA. We assume tangential neutral beam heating with a heating power of 17 MW. Therefore, we need additional terms in transport equations and Fokker-Planck equation which are explained in section 6.2. Also, we need additional equations for multispecies ions. In the transport code, coupled with the ABLATE code, we solve the following equations for electron density, n_e, tritium density, n_T, electron temperature, T_e, ion temperature, T_i, and poloidal magnetic field, B_θ :

$$\frac{\partial n_e}{\partial t} = -\frac{1}{r}\frac{\partial}{\partial r}(r\Gamma_e) + \dot{S} , \tag{8.1}$$

$$\frac{\partial n_T}{\partial t} = -\frac{1}{r}\frac{\partial}{\partial r}(r\Gamma_T) - n_D n_T \langle\sigma_{DT} v\rangle - \dot{S}_{TCT} , \tag{8.2}$$

$$\frac{\partial}{\partial t}(\frac{3}{2} n_e T_e) = -\frac{1}{r}\frac{\partial}{\partial r}(rQ_e) + W_e , \tag{8.3}$$

$$\frac{\partial}{\partial t}(\frac{3}{2} n_i T_i) = -\frac{1}{r}\frac{\partial}{\partial r}(rQ_i) + W_i , \tag{8.4}$$

$$\frac{\partial B_\theta}{\partial t} = \frac{\partial}{\partial r}(\frac{\eta}{\mu_0}\frac{1}{r}\frac{\partial}{\partial r}(rB_\theta)), \tag{8.5}$$

where n_i is total ion density, Q_e and Q_i include convection terms as

$$Q_e = \chi_e n_e \frac{\partial T_e}{\partial r} + \frac{3}{2} T_e \Gamma_e , \tag{8.6}$$

$$Q_i = \chi_i n_i \frac{\partial T_i}{\partial r} + \frac{3}{2} T_i \Gamma_e \quad , \tag{8.7}$$

and Γ_e and Γ_T are radial particle fluxes for electrons and tritium ions, respectively ;

$$\Gamma_e = D \frac{\partial n_e}{\partial r} \quad , \tag{8.8}$$

$$\Gamma_T = D \frac{\partial n_T}{\partial r} \quad . \tag{8.9}$$

$\dot{S}$ is the electron source due to ionization of recycled neutrals and beam particles, $\dot{S}_{TCT}$ signifies the loss of tritium particles due to the Two-Component-Torus (TCT) effect[66] (thermal tritium reacting with beam dueterons). The second rhs term of Eq.(8.2) describes the fusion reactions of thermal particles. W_e includes the energy deposition to electrons by NBI and ionization loss and W_i includes the energy deposition to ions by NBI and charge exchange loss. Both terms also include the energy exchange between electrons and ions. We solve the equation for the tritium density after pellet injection, assuming that the deuterium ion temperature and the tritium ion temperature are equal to T_i. Density increase and temperature decrease at the instant of pellet injection are calculated with help of the self-limiting model proposed by Houlberg et al.[51] For alpha particles we solve the following equation,

$$\frac{\partial n_\alpha}{\partial t} = n_D n_T \langle \sigma_{DT} v \rangle + \dot{S}_{TCT} \quad . \tag{8.10}$$

Here we neglect the alpha particle diffusion in (8.10) as we did the alpha heating in (8.4). The alpha heating power is small compared with the neutral beam heating power in $Q \sim 1$ plasmas. The

deuterium density is calculated from $n_D=n_e-n_T-2n_\alpha$. The assumption of no alpha particle diffusion may influence the deuterium profiles, however insignificantly, since $n_\alpha \ll n_T$. Also tritium recycling is assumed to be negligible.

In the calculation of deuterium beam heating, we solve numerically the linearized Fokker-Planck equation which includes DT reaction term. Furthermore, we have assumed tangential injection, different from the NBI system in JT-60.

The TCT term in (8.2) is given by

$$S_{TCT} = 4\pi \int n_T \sigma_{DT}(v) f(v) v^3 dv \qquad (8.11)$$

where the fast deuterium distribution function f is calculated by the Fokker-Planck code, and σ_{DT} is the DT fusion reaction cross-section. The neutral deuterium particles are included in the calculation through a Monte-Carlo method similar to the AURORA code[55], the halo neutrals produced by the NBI are, however, neglected.

For the transport coefficients in Γ_e , Γ_T , Q_e and Q_i , we assume Alcator scaling for the electron thermal transport and particle transport, $\chi_e=(5\times10^{19}/n_e)$ m^2/s and $D=(5\times10^{18}/n_e)$ m^2/s . The ion thermal transport is assumed to be three times as large as the neoclassical value given by Hinton and Hazeltine[58] . It is noted that tokamak confinement usually degrades for high power neutral beam injection and that confinement scaling in that case is different from the Alcator scaling. However, if H-mode operation can be realized in large tokamaks, the plasma confinement may be comparable to that given by the Alcator scaling[67] . If the Ware pinch effect is included, the tritium density in the central region

is expected to increase and more optimistic results than the present model may be obtained. The impurity effect is included through Z_{eff}=2 and the radiation loss is simulated by enlarging the electron ionization loss energy to 40 eV.

For pellet injection, the pellet size and injection velocity are decisive parameters. We chose the smallest pellet to minimize tritium consumption in the experiment for $Q > 1$. The maximum size of pellets produced by present injectors is 2 mm (radius)[36]. We assume such a 2 mm radius tritium pellet in the following calculations. The total number of atoms in this pellet is 2.164×10^{21} and the radioactivity is 3.881×10^{12} Bq. Its weight is 10.85 mg. In order to understand the physics of reacting plasmas, we may need about one thousand pellets. Thus, this size will be reasonable in the initial experiments. In general, it is difficult to inject pellets smaller than 2 mm radius into the central region of a large tokamak, when the pellet velocity is limited within a few km/s. The maximum pellet velocity realized in TFTR is 1.5 km/s[37]. However, this velocity is not sufficient to inject a pellet of 2 mm radius into the central plasma core. We assume that an injection velocity 5 km/s will be realized in the near future by further development in the injection technology. The following development seems possible. The maximum velocity of a pellet accellerated by applying a high-pressure hydrogen propellant is $v_{max} = 5C_H$, where C_H is the sound velocity of hydrogen. At room temperature, v_{max} = 6.5 km/s and at 100 K, v_{max} = 3.8 km/s[68]. Thus an injection velocity of 4 to 5 km/s may be possible.

8.3 Results of numerical calculations

We will now explain the achievement of $Q > 1$ through our transport model. Figure 8.1(a) shows an ablation profile calculated by using ABLATE code discussed in section 5.2. The model predicts a penetration depth consistent with the pellet injection into the NBI heated plasmas of Heliotron E[46]. Since the ratio between the fast ion heat flux to the electron heat flux is relatively small, the effect of fast ions on the ablation is not significant in this case. The pellet size is 2 mm (radius) and its velocity is 5 km/s. The target plasma has a central ion temperature, $T_i(0)\sim 28$ keV, a central electron temperature, $T_e(0)\sim 9.5$ keV, and a central density, $n_e(0)\sim 8.5\times 10^{13}$ cm^{-3} , as shown in Fig.8.1(b),(c), and (d). The neutral beam energy is assumed to be 135 keV. The temperatures and the density just after pellet injection are designated by continuous lines in contrast to the dashed lines which signify the discharge before the pellet injection. Here, we assumed a self-limiting ablation process[51] (see section 5.2). The target plasma is called a 'hot-ion-mode' plasma, in accordance with Ref.(69).

Figure 8.2(a) shows the time evolution of both the average ion and electron temperatures. The profiles of T_i and T_e are shown in Fig.8.4(c) and (d), the corresponding Q value in Fig.8.2(c). From t=3.2 s to t= 3.85s, $Q > 1$ is obtained. During this period the TCT reaction is responsible for approximately one third of all the reactions. The sharp peak in the Q value just after the pellet injection is due to reactions between the injected tritium and the fast dueterium ions before the rapid energy relaxation as a result

of the pellet injection. The decay of the peaked Q value contains information on the slowing down process of the fast ions (see Fig.8.3(c) and Fig.8.4(b)). Figure 8.2(b) shows the energy and particle confinement times. The ion energy confinement time is about 4 s before and after pellet injection. The electron energy confinement time increases from ~ 150 ms to ~ 300 ms. This tendency is expected from the Alcator scaling law. Energy deposition from the neutral beam to the ions and the electrons is shown in Fig.8.2(d).

The time evolution of electron, deuterium, and tritium densities is shown in Fig.8.3(a) and (b). The decay of the electron density before pellet injection (Fig.8.3(a)) is due to an assumed recycling rate less than unity, which is also assumed after the pellet injection. The density of fast ions is given in Fig.8.3(c). The increase of the average deuterium density after the pellet injection (Fig.8.3(b)) is due to an enhancement of the energy relaxation of fast deuterium ions, caused by an increase of the electron density and a rapid decrease of the electron temperature just after the pellet injection. This is confirmed by the observed decrease of the fast deuterium as shown in Fig.8.3(c). The corresponding time evolution of n_T and that of the fast ion density profiles are shown in Fig.8.4(a) and (b), respectively. In order to understand the most important factor for obtaining $Q > 1$, the fast ion profile as shown in Fig.8.4(b) is crucial. Before the pellet injection the fast ion density is peaked at the magnetic axis. After the pellet injection the fast ion density has a shallow peak at $r/a \sim 0.6$. It moves gradually to the magnetic axis. The reaction rate profiles for both the thermonuclear reactions and the TCT

reactions are shown in Fig.8.5(a) and (b). In this calculation the tritium density is peaked at the center except during approximately 100 ms after the pellet injection (Fig.8.4(a)).

The main cause for Q to exceed the value Q=1 in the case shown in Figs.8.1-8.5 are : (1) the tritium pellet penetration is fairly deep, and (2) the fast ions can penetrate into the central region except just after the pellet injection and the ion temperature increases fairly rapidly (see Fig.8.2(a)). The first point depends on the pellet velocity, the pellet size, and the ablation model. The second point depends on the calculation of the NBI heating process. For both points we believe our approaches are reasonable even for a quantitative prediction.

We will now make a few remarks on phenomena that may affect our results. In the above model calculation we neglected the alpha particle heating which is of the order of 3 MW, and, thereby, may be instrumental in keeping Q>1. During the period when Q exceeds 1, the central beta value, $\beta(0)$, increases up to 6.5%, whereas, the average value, $\overline{\beta}$, is 0.7-0.8% as shown in Fig.8.3(d). These values are close to the ideal MHD beta limit of a circular cross-section tokamak, but these are realistic since in the JFT-2 experiment, $\overline{\beta}$ reached a value of $\sim$ 2% [70]. There is a possibility that pellet injection triggers a disruption. This depends on the injection condition. Pellet injection with a sufficient penetration depth into a NBI heated plasma, however, does not necessarily trigger a disruption. At the instant of pellet injection, the pressure profile does not change significantly since the self-limiting process is adiabatic. This means that the current density profile and the safety factor profile also do not change appreciably. An

additional consideration is that, since the NBI heating heats the plasma edge region, a shrinkage of the current density profile may be supressed during the transient phase after the pellet injection.

Figure 8.6 shows the case that the pellet velocity is 2 km/s and the pellet radius is 2 mm. The penetration depth is roughly 80% compared to that of Fig.8.1(a). The maximum Q value is now 0.91 as shown in Fig.8.6(d). Fig.8.6(c) shows that the behaviors of the average electron and ion temperature are similar to those of Fig.8.2(a). The reduction of the Q value can be explained by the fact that the tritium density in the central high ion temperature region becomes lower and the fast ion density profile becomes broader than those in Figs.8.1-8.5 due to the short-range penetration of the pellet.

Figure 8.7 shows the case that the pellet velocity is 2 km/s and the pellet radius is 2.2 mm. The total number of tritium atoms is now 2.88×10^{21} which is 33% larger than that of the 2 mm radius pellet. Also for these values $Q > 1$ is possible within our transport model. An existing pellet injector such as used for TFTR may realize these values upon improvement of the injector.

When the pellet velocity is limited within 2 km/s, an idea to inject tritium atoms deeply into the plasma column without increasing the total tritium weight might be the injection of a deuterium-coated tritium pellet. For example, the total radius of such a pellet could be 2.5-3 mm, while that of the tritium sphere is only 2 mm. The technology of producing coated pellets can also be applied to study two-ion hybrid cyclotron heating in magnetically confined plasmas.

8.4 Conclusion

In order to achieve $Q > 1$ with minimum tritium consumption in reacting plasma experiments, tritium pellet injections into deuterium plasmas heated by neutral deuterium beams with $E_{BEAM} > 100$ keV look promising. In the presented computation a tokamak transport code is combined with a pellet ablation code based on a neutral shielding model including fast ion effects in the ablation process. $Q > 1$ is realized during half a second by injecting a pellet with a radius of 2 mm and a velocity of 5 km/s into a plasma of $T_i(0)$=25-30 keV, $T_e(0)$=9.5 keV, and $n_e(0)=8.5\times10^{13}$ cm^{-3}, i.e a 'hot-ion-mode' plasma. The tokamak parameters are : a(minor radius) = 0.9 m, R_0(major radius) = 3.0 m, B_T(toroidal magnetic field) = 4.5 T, and I_p = 2.7 MA. The anomalous electron transport is assumed to follow Alcator scaling and the ion transport is assumed three times larger than the neoclassical value. The total neutral beam power is 17 MW. The total energy confinement time is approximately 0.5 s and the average electron density is around 6.5×10^{13} cm^{-3} during $Q > 1$. For larger pellet radii, smaller injection velocities appear feasible.

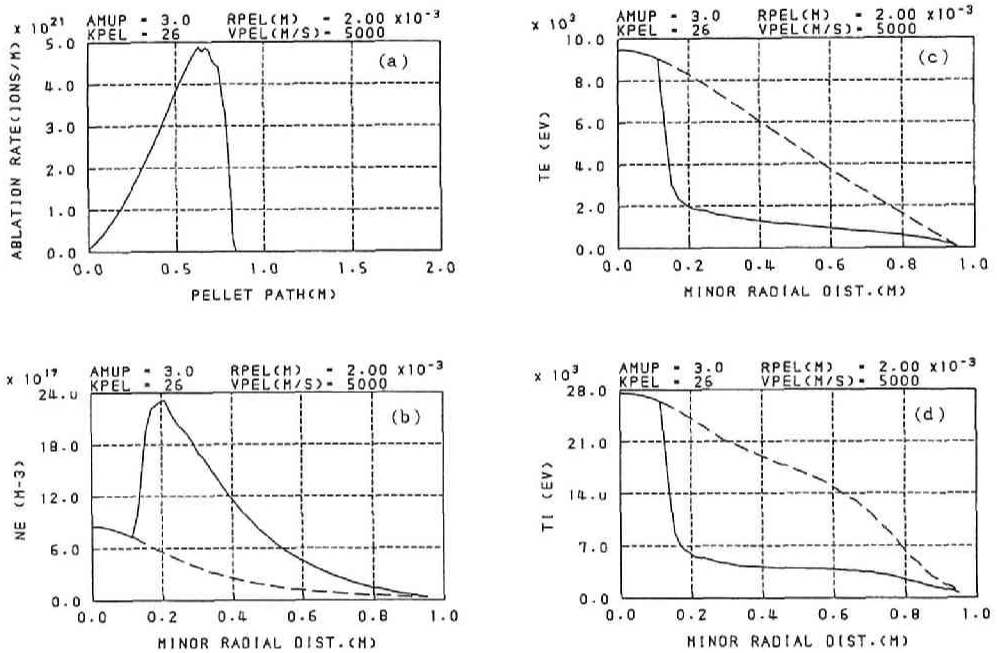

Fig.8.1. (a) : Ablation profile for T_2 pellet injection into a deuterium plasma of a JT-60-like large tokamak (R_0=3 m, a=0.9 m). Penetration depth is 0.82 m. Initial pellet radius is 2 mm (2.164×10^{21} atoms) and injection velocity is 5 km/s. (b),(c),(d) : electron density, electron and ion temperature profiles just before (dashed lines) and just after (solid line) pellet injection, respectively.

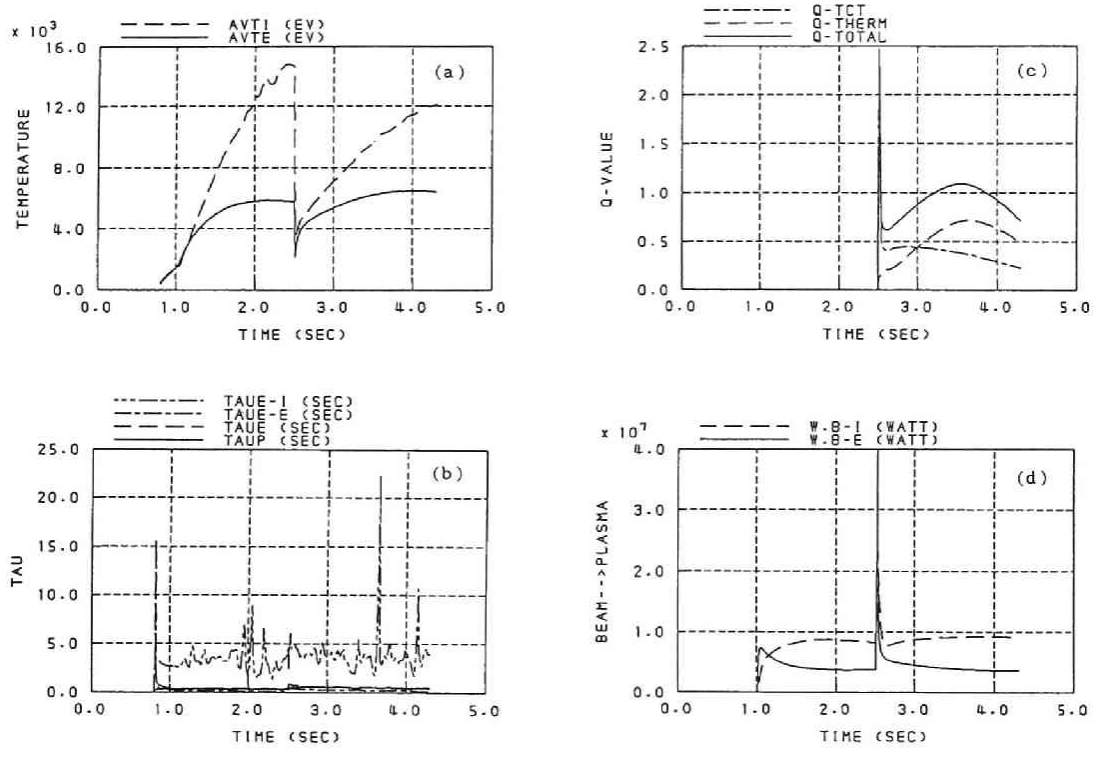

Fig.8.2. Time evolution of (a) average electron temperature (solid line) and ion temperature (dashed line), (b) particle confinement time (solid line), total energy confinement time (dashed line), electron energy confinement time (dot-dashed line) and ion energy confinement time (dot-dot-dashed line), (c) total Q value (solid line), Q value due to thermonuclear reactions (dashed line) and TCT reactions (dot-dashed line), (d) energy deposition to thermal electrons (solid line) and thermal ions (dashed line) due to NBI. Pellet is injected at 2.5 s.

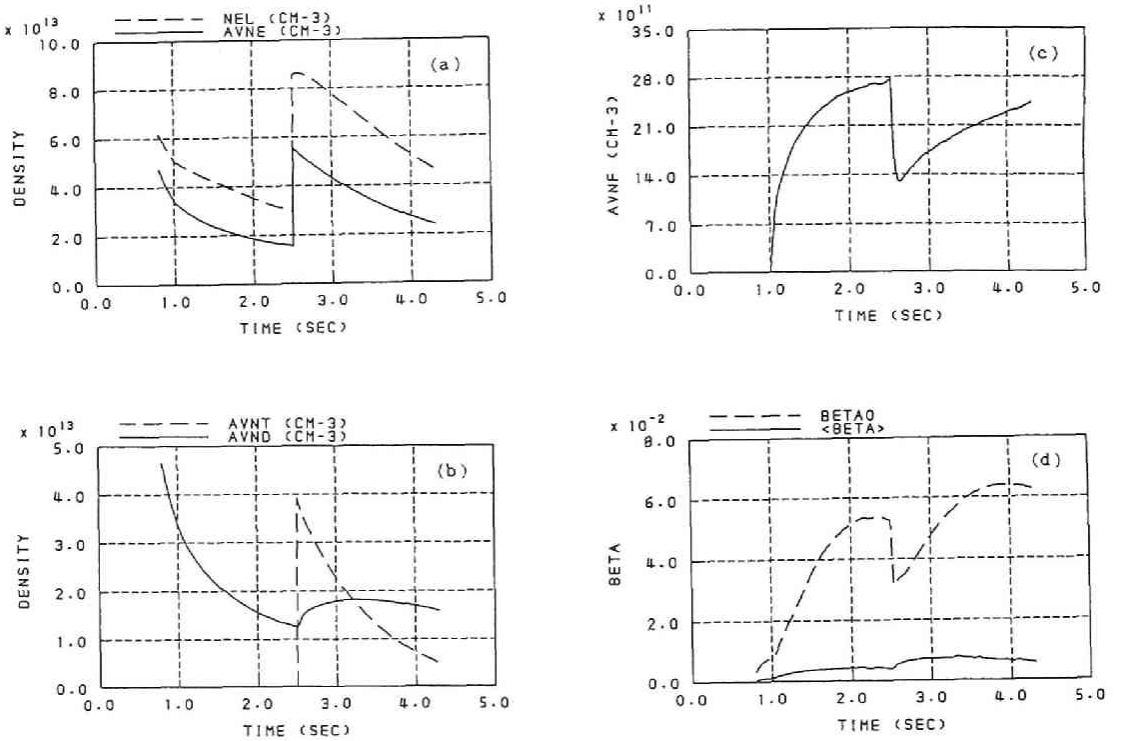

Fig.8.3. Time evolution of (a) volume-averaged (solid line) and line-averaged (dashed line) electron density, (b) volume-averaged deuterium (solid line) and tritium (dashed line) density, (c) volume-averaged fast deuterium density, (d) average β value (solid line) and central β value (dashed line).

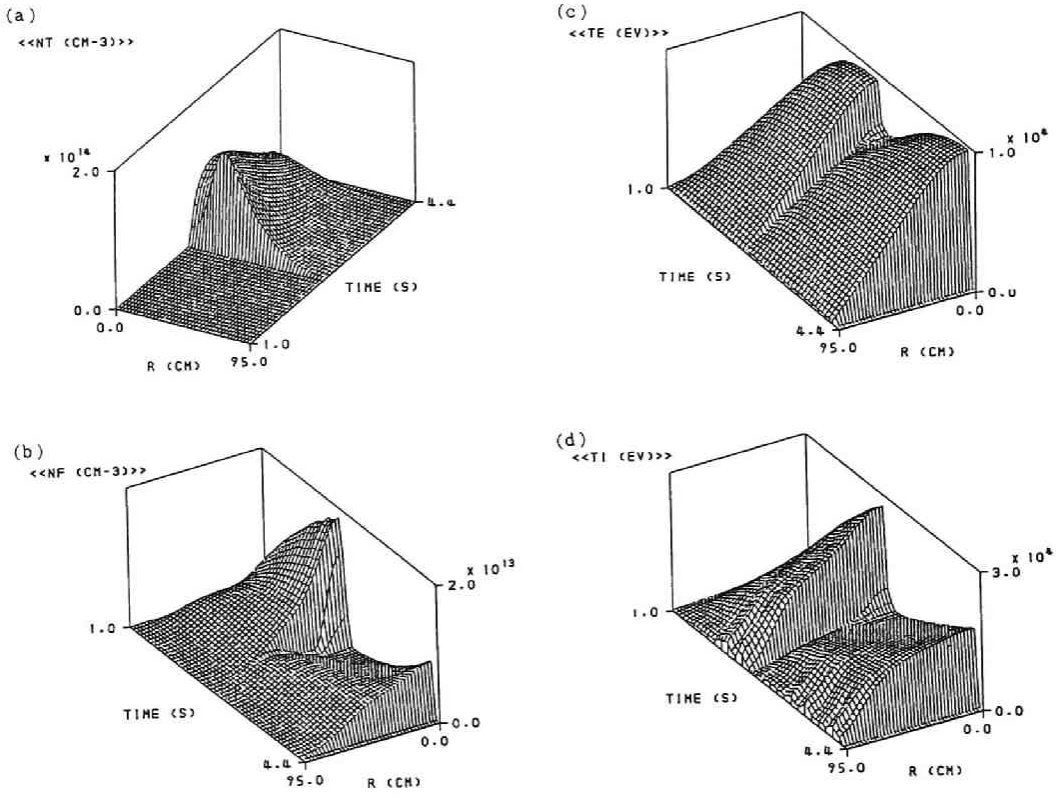

Fig.8.4. Time evolution of (a) tritium density profile, (b) fast deuterium density profile, (c) electron temperature profile, (d) ion temperature profile corresponding to Fig.8.1. Initial tritium density profile is shown in Fig.8.1(a).

(a)

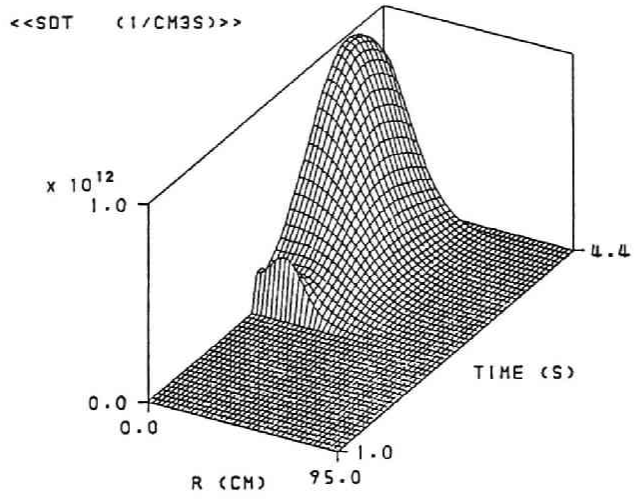

(b)

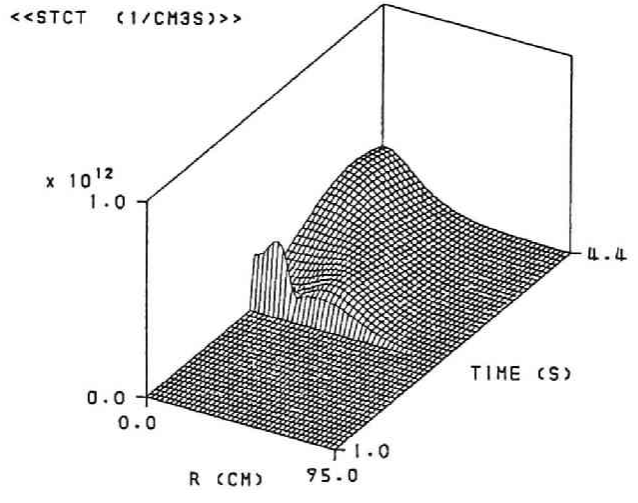

Fig.8.5. Time evolution of fusion reaction rates for (a) thermonuclear reactions, $n_D n_T \langle \sigma_{DT} v \rangle$, and (b) TCT reactions, S_{TCT} .

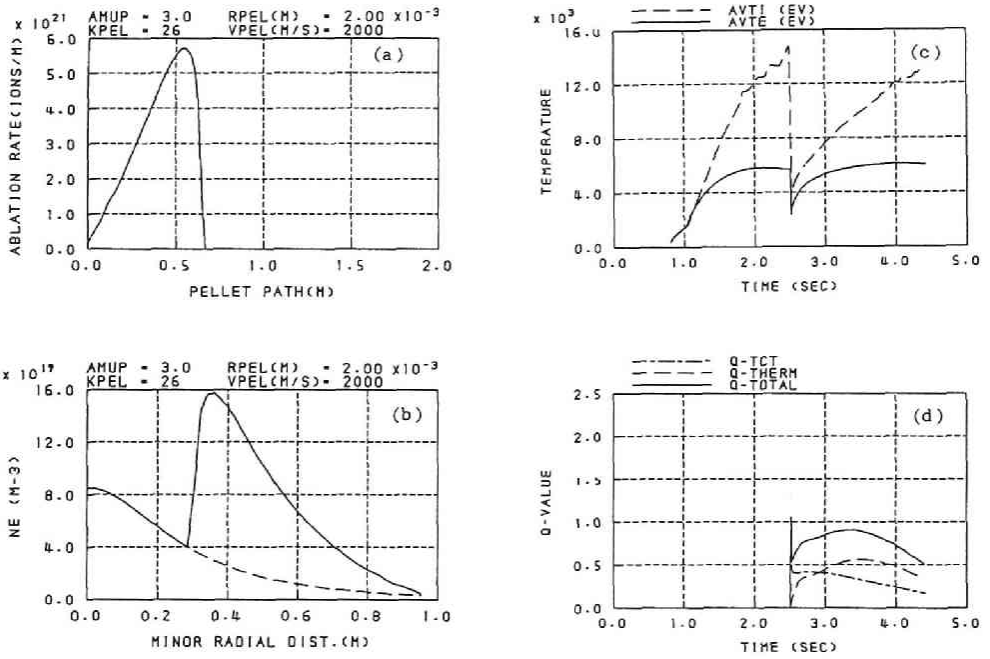

Fig.8.6. Results for slower pellet injection velocity than that of Fig.8.1 : (a) ablation profile, (b) electron density profile just before (dashed line) and just after (solid line) pellet injection. (c) time evolution of volume-averaged electron (solid line) and ion (dashed line) temperature, (d) time evolution of total Q value (solid line), Q value for thermonuclear reactions (dashed line) and TCT reactions (dot-dashed line). Pellet radius is 2 mm and pellet velocity is 2 km/s.

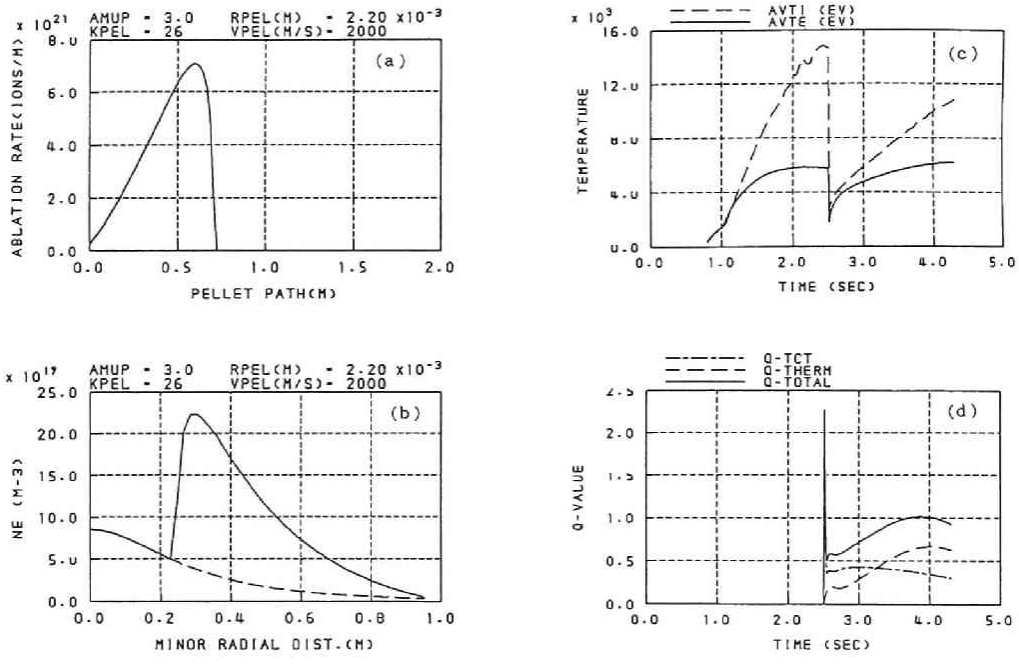

Fig.8.7. Results for slower pellet injection velocity and larger pellet radius than those of Fig.8.1 : (a) ablation profile, (b) electron density profile just before (dashed line) and just after (solid line) pellet injection, (c) time evolution of volume-averaged electron (solid line) and ion (dashed line) temperature, (d) time evolution of total Q value (solid line), Q value for thermonuclear reactions (dashed line) and TCT reactions (dot-dashed line). Pellet radius is 2.2 mm and pellet velocity is 2 km/s.

CHAPTER 9

Concluding Remarks

Theoretical analyses of several physical problems relating to the pellet injection into magnetically confined plasmas have been described. Main results of this study are summarized as follows.

(1) On the basis of the neutral cloud shielding model by Parks and Turnbull[6], a new ablation model applicable to the case that multiple energy carriers exist in the ablation cloud has been developed. This model is useful especially to analyse pellet injection experiments into NBI heated plasmas.

(2) The model has been applied to the cases including both thermal electrons and fast ions, and including both thermal electrons and non-thermal electrons as incident heat fluxes, respectively. The ablation rate essentially depends on the range of the multiple energy carriers in the cloud. The effect of fast ions on the ablation rate was more milder than that by the Milora model.

(3) When the incident heat flux of fast ions produced by the neutral beam injection governs the ablation process, the simple scaling law[7] for the ablation rate has been presented and it saves computational time for analysing the pellet ablation.

(4) The ABLATE code based on the present model has been developed, which calculates the ablation rate profile of the pellet injected into the magnetically confined toroidal plasma. Analysis for a neutral beam heated toroidal plasma by the ABLATE code made clear that the fast ions enhanced the pellet ablation

especially in the edge region of the plasma column as observed in many experiments. Generally, our model gave a larger pellet penetration depth than that by the Milora model[8] in which the effect of fast ions was treated without solving the cloud dynamics directly. It was shown that non-thermal electrons yield the high pellet ablation for $E_f/T_e \geq 16$ and $n_f/n_e \geq 0.003$, where E_f is an energy of non-thermal electrons and n_f is a density of non-thermal electrons.

(5) The transport code including the ABLATE code has been developed to investigate transport properties after the pellet injection. By using this transport code, the pellet injection experiment into the Ohmically heated plasma in ISX-B[12] was simulated. A consistent result was obtained by assuming the anomalous transport known as the Alcator scaling.

(6) By the ABLATE code, it was shown that our model can explain the penetration depth of the pellet injected into Heliotron E, when the plasma was heated by the NBI. The Milora model gave a shorter penetration depth than that observed experimentally.

(7) In the analysis of an Ohmically heated Heliotron E plasma by the transport code, a shrinkage of the current channel was obtained after the pellet injection, when the pellet penetration depth was shallow. This is because the plasma is cooled and the conductance is reduced in the peripheral region by the shallow pellet injection. If it makes the rotational transform exceed unity in the central region, it has a possibility to induce a current driven instability. In the calculation of the pellet injection into the NBI heated current-free plasma, quick recovery of the electron and ion temperatures was obtained in

contrast with the case of the Ohmic heating plasma, since thermalization of fast ions is enhanced by the rapid density increase and the associated electron temperature decrease.

(8) The linear stability analysis on Heliotron E against the ideal and the resistive interchange modes (G modes) suggested that a peaked pressure profile after the pellet injection may make the plasma unstable against the G modes when $\beta(0)$ exceeds 1%[10].

(9) Possibility of achieving $Q>1$ by the tritium pellet injection into deuterium tokamak plasmas with the neutral deuterium beam heating[11] was investigated. By using the transport model for D-T burning plasmas including the TCT effect, it was revealed that the sufficient TCT effect and the deep penetration of the tritium pellet are essential to achieve $Q>1$ in a tokamak similar to JT-60 with 17MW NBI heating. These were obtained by the pellet injection into the 'hot-ion-mode' plasma heated by the high energy NBI.

There are limitations in our new ablation model based on the neutral cloud shielding. When the assumption of the surface ablation becomes invalid, our model will not be applicable. In other words, simplified boundary conditions used in chapter 4 (or conditions that the flow velocity of the cloud and the incident heat flux are negligibly small on the pellet surface. See Eqs.(4.10) and (4.11)) is not applicable, for example, when the heat flux at the pellet surface is significantly high. So far, our model seems to be valid for the conditions of the present pellet injection experiments, and it will be applicable even to the pellet injection experiment in reactor relevant large tokamaks such as TFTR. The remaining problem is an alpha particle effect on the

pellet ablation in D-T burning plasmas.

In future, the effect of the Maxwellian energy distribution of thermal electrons, instead of monochromatic electrons in the present study, should be taken into account in our model with appropriate boundary conditions discussed in chapter 3. Furthermore, additional shielding mechanisms, such as magnetic shielding and plasma shielding by a plasma spread along the field line, should be examined to establish an ablation model applicable to the pellet injection into a future reactor plasma.

From technological point of view, the ABLATE code is useful to optimize teh pellet velocity and the pellet size in the design of a new pellet injector for a new experimental device.

APPENDIX

We shall present here briefly the basic equations and solutions of the Milora model, given in Ref.[8] concerning our present article.

The basic equations determining the ablation rate of a pellet can be written as

$$\frac{dr_p}{dt} = -\frac{1.25}{r_p\rho_s}\left(\frac{\gamma-1}{2}e\langle W\rangle r_p\right)^{1/3}\int_{r_p}^{\infty}\rho dr \qquad (A.1)$$

and

$$\frac{dr_p}{dt} = -\frac{Q_p}{4\pi r_p^2\lambda n_s} \qquad (A.2)$$

where $\langle W\rangle$ is the average heating power per mass of the ablation cloud in eV/kg· sec, Q_p is heating power at the pellet surface in eV/sec, and λ is the ablation energy per pellet atom. Equation (A.1) is called the shielding equation of the cloud and gives a scaling relation between the heating power and the integrated column density of the cloud, D, defined as

$$D \equiv \int_{r_p}^{\infty}\rho dr \ .$$

The scaling relation (A.1) is obtained from numerical calculations of the fluid equations for the cloud, including electron heat flux only[19] . This scaling relation is assumed to be unchanged by the presence of fast ions. Eq.(A.2) is energy balance equation at the pellet surface. Here we use sublimation energy as the ablation energy and λ = 0.005eV/atom for a hydrogenic pellet. If a relation among $\langle W\rangle$, D, and Q_p is found, Eqs.(A.1) and (A.2) can be regarded

as a closed set of equations.

From the attenuation equation of the electron heat flux, the column density of the cloud is related to the electron heat flux at the pellet surface as

$$D(y) = \begin{cases} \dfrac{m}{\alpha_e}\ln\left(\dfrac{2q_{e0}}{yq_{e\infty}}-1\right)+m\displaystyle\int_{E_{e0}}^{E_{e\infty}}\frac{dE_e}{L_e} & for \quad E_{ep}<E_{e0} \\ m\displaystyle\int_{yE_{e\infty}}^{E_{e\infty}}\frac{dE_e}{L_e} & for \quad E_{ep}\geqq E_{e0}. \end{cases} \qquad (A.3)$$

Here, $y\equiv q_{ep}/q_{e\infty}$, $E_e=3/2T_e$, $E_{e0}=20$ eV, and numerical factor $\alpha_e=2\times10^{-20}$. In Eq.(A.3), the logarithmic term denotes the effect of elastic collisions at low electron energy ($E_e<E_{e0}$), and q_{e0} is the heat flux at $E_e=E_{e0}$. When $E_e\geqq E_{e0}$, elastic collisions are negligible. If we neglect the energy scattering of the fast ions in the cloud, the heat flux of the fast ions on the pellet surface is related to column density D by

$$q_{fp} = \frac{\pi m_f}{2e}\int_{v_{min}}^{\infty} v_p^3 f(v_f)\, v_f^2 dv_f \ , \qquad (A.4)$$

where

$$v_p = \left[\frac{2e}{m_f}\left\{\left(\frac{m_f v_f^2}{2e}\right)^{3/5}-\frac{3\alpha_f D}{5m}\right\}^{5/3}\right]^{1/2}$$

and

$$v_{min} = \left[\frac{2e}{m_f}\left(\frac{3\alpha_f D}{5m}\right)^{5/3}\right]^{1/2}$$

Here v_p is obtained by integrating Eq.(3.15) with (4.8). q_{fp} is also considered to be a function of y through Eq.(A.3). Here $\alpha_f=1.93\times10^{-20}$. In the slab approximation, the average heating power in the cloud, $\langle W\rangle$, as a function of y is given by

$$\langle W\rangle = \{f_{Be}q_{e\infty}(1-y)+f_{Bf}(q_{f\infty}-q_{fp}(y))\}/D(y) \qquad (A.5)$$

and the heating power on the pellet surface is

$$Q_p = y q_{e\infty} A_e + q_{fp}(y) A_f \qquad (A.6)$$

where A_e and A_f are effective cross sections of the pellet for electrons and fast ions, respectively. We assume $A_e=2\pi r_p^2$ and $A_f=4\pi r_p^2$. Since $\langle W \rangle$, Q_p, and D are expressed in terms of y, Eqs.(A.1) and (A.2) become closed equations for dr_p/dt and y. The ablation rate, dr_p/dt, is obtained by solving these equations, when the ambient plasma parameters are given. If there is no solution for y in the region $(\varepsilon,1)$ with $\varepsilon=10^{-70}$, y is regarded as zero, and Eq.(A.3) cannot used any longer In this case, since $\langle W \rangle$ and Q_p can be expressed as functions of D, Eqs.(A.1) and (A.2) are solved for dr_p/dt and column density D. This corresponds to the case where incident electrons cannot reach the pellet surface; however, the heating power in the cloud is still assumed uniform and the average heating power $\langle W \rangle$ of (A.5) is used.

REFERENCES

[1] C.T.Chang,L.W.Jorgensen,P.Nielsen,L.L.Lengyel ; Nucl.Fusion 20 (1980) 859.

[2] S.L.Milora ; J.Fusion Energy 1 (1981) 15.

[3] J W.M.Paul,et al. ; in Proc. 6th IAEA Conf. on Plasma Physics and Controlled Nucl. Fusion Research (London,1984) Vol.2,15.

[4] S.L.Milora,C.L.Schmidt,W.A.Houlberg,V.Arunasalam, S.E.Attenberger,et al. ; Nucl.Fusion 22 (1982) 1263.

[5] P.B.Parks,R.J.Turnbull,C.A.Foster ; Nucl.Fusion 17 (1977) 539.

[6] P.B.Parks,R.J.Turnbull ; Phys.Fluids 21 (1978) 1735.

[7] Y.Nakamura,H.Nishihara,M.Wakatani ; Nucl.Fusion 26 (1986) 907.

[8] MILORA,S.L. ; Oak Ridge National Laboratory Rep., ORNL/TM-8616 (1983).

[9] Y,Nakamura,H.Nishihara,M.Wakatani ; Kakuyugo-Kenkyu 52 (1984) 173 (in Japanese).

[10] M.Yamagiwa,M.Wakatani,Y,Nakamura ; J.Phys.Soc.Jpn. 54 (1985) 15.

[11] Y.Nakamura,M.Wakatani,S.Yoshimura,A.Iiyoshi ; to be published in Nucl.Fusion

[12] S.L.Milora,C.A.Foster,C.E.Thomas,C.E.Bush, J.B.Wilgen,et al. ; Nucl.Fusion 20 (1980) 1491.

[13] L.L.Lengyel ; Max-Planck Institut für Plasmaphysik Rep , IPP-1/232 (1984).

[14] H.Sorensen ; J.Appl.Phys. 48 (1977) 2244.

[15] S.L.Gralnick ; Nucl.Fusion 13 (1973) 703.

[16] D.J.Rose ; Culham Laboratory Technical Division Memorandum No.82 (1968).

[17] C.A.Foster,R.J.Colchin,S.L.Milora,et al. ; Nucl.Fusion 17 (1977) 1067.

[18] D.F.Vaslow ; IEEE Trans.Plasma Sci. PS-5 (1977) 12.

[19] S.L.Milora,C.A.Foster ; IEEE Trans.Plasma Sci. PS-6 (1978) 578.

[20] L.L.Lengyel ; Phys.Fluids 23 (1980) 656.

[21] S.Sudo ; Kakuyugo-Kenkyu 55 (1986) 272 (in Japanese).

[22] F.S.Felber,P.H.Miller,P.B.Parks,et al. ; Nucl.Fusion 19 (1979) 1061

[23] C.T.Chang ; Nucl.Fusion 15 (1975) 595.

[24] L.L.Lengyel ; Phys.Fluids 21 (1978) 1945.

[25] P.B.Parks ; Nucl.Fusion 20 (1980) 311.

[26] F.J.Mayer ; Phys.Rev.Lett. 48 (1982) 1400.

[27] F.J.Mayer ; Phys.Rev.Lett. 55 (1985) 1673.

[28] M.Kaufmann,K.Lackner,L.Lengyel,W.Schneider, Nucl.Fusion 26 (1986) 171.

[29] K.Büchl ; in Proc. 9th Intl. Vac. Congr. (Madrid,1983) 195.

[30] TFR Group ; in Proc. 13th Europ. Conf. on Controlled Fusion and Plasma Heating (Schliersee,1986) Part.I,200

[31] V.Lunsford,et al. ; in Proc. 9th Sympo. on Engineering Problems of Fusion Research (1981) Vol.2,1721.

[32] S.Sengoku,M.Abe,K.Hoshino,K.Itoh,A.Kameari,el at. ; in Proc. 10th IAEA Conf. on Plasma Physics and Controlled Nucl.Fusion Research (London,1984) Vol.1,405.

[33] Oak Ridge National Laboratory, Fusion Energy Division, Annual

Progress Rep. (1984), ORNL-6111.

[34] G.Vlases,M.Kaufmann,O.Gruber,G.Haas,et al. ; in Proc. 12th Europ.Conf. on Controlled Fusion and Plasma Phys. (Budapest,1985) Part.I,78.

[35] R.B.Wysor,L.R.Baylor,W.E.Bryan,et al., in Proc. 11th Sympo. on Fusion Engineering (Austin,1985) Vol.2,755.

[36] S.K.Combs,S.L.Milora,C.R.Foust,et al. ; Rev.Sci.Instrum. 56 (1985) 1173.

[37] G.L.Schmidt,S.L.Milora,M.G.Bell,et al ; in Proc. 12th Europ.Conf. on Controlled Fusion and Plasma Phys. (Budapest,1985) Part.Ⅱ ,674.

[38] R.V.Lansford,R.B.Wysor,W.E.Bryan,et al., in Proc. 11th Sympo. on Fusion Engineering (Austin,1985) Vol.2,763.

[39] P.W.Fisher,L.R.Baylor,W.E.Bryan,et al., in Proc. 11th Sympo. on Fusion Engineering (Austin,1985) Vol.2,759.

[40] S.L.Milora,C.A.Foster,P.H.Edmonds,G.L.Schmidt ; Phys.Rev.Lett. 42 (1979) 97

[41] M.Greenwald,D.Gwinn,S.Milora ; in Proc. 10th IAEA Conf. on Plasma Physics and Controlled Nucl.Fusion Research (London,1984) Vol.1,45.

[42] S.M.Wolfe,M.Greenwald,R.Gandy,et al. ; Nucl.Fusion 26 (1986) 329.

[43] H.Niedermeyer,K.Büchl,M.Kaufmann,et al. ; in Proc. 13th Europ. Conf. on Controlled Fusion and Plasma Heating (Schliersee,1986) Part.I,168.

[44] S.Sengoku,N.Nagami,M.Abe,et al. ; Nucl.Fusion 25 (1985) 1475.

[45] D.K.Owens ; to be published in Proc. 11th IAEA Conf. on Plasma Phys. and Controlled Nucl.Fusion Research

(Kyoto,1986).

[46] S.Sudo,O.Motojima,M.Sato,H.Zushi,et al. : Nucl.Fusion 25 (1985) 94.

[47] N.L.Vasin,N.M.Gegechkori,S.M.Egorov,et al. ; Sov.J.Plasma Phys. 10 (1984) 650.

[48] V.Andersen ; in Proc. 12th Europ.Conf. on Controlled Fusion and Plasma Phys. (Budapest,1985) Part.Ⅱ ,648.

[49] W.W.Heidbrink ; Princeton Univ. Plasma Phys. Laboratory Rep.,PPPL-2299 (1986).

[50] M.Sasao,K.N.Sato,Y.Nakamura,M.Wakatani ; to be published in Nucl.Fusion.

[51] W.A.Houlberg,M.A.Iskra,H.C.Howe,S.E.Attenberger ; Oak Ridge National Laboratory Rep., ORNL/TM-6549 (1979).

[52] M.Okamoto,T.Amano ; J.Comp.Phys. 26 (1978) 80.

[53] K.Shimizu,M.Okamoto,T.Amano ; J.Phys.Soc.Jpn. 50 (1981) 1366.

[54] R.H.Fowler,J.D.Callen,J.A.Rome,J.Smith ; Oak Ridge National Laboratory Rep., ORNL/TM-5487 (1976).

[55] M.H.Hughes,D.E.Post ; J.Comp.Phys. 28 (1978) 80.

[56] L.L.Lengyel ; Max-Planck Institut für Plasmaphysik Rep., IPP-1/213 (1983).

[57] H.Zushi,M.Wakatani,K.Takeuchi ; Nucl.Fusion 24 (1984) 305.

[58] F.L.Hinton,R.D.Hazeltine ; Rev.Mod.Phys. 48 (1976) 239.

[59] M.Wakatani,H.Shirai,H.Zushi,et al. ; Nucl.Fusion 23 (1983) 1669.

[60] H.R.Strauss ; Phys.Fluids 22 (1980) 733.

[61] M.Wakatani,H.Shirai,M.Yamagiwa ; Nucl.Fusion 24 (1984) 1407.

[62] JT-60 Team, in Proc. 12th European Conf. on Controlled Fusion and Plasma Physics (Budapest,1985) vol.1,375.

[63] P.C.Efthimion,N.Bretz,M.Bell,M.Bitter,W.R.Blanchard,et al. ; in Proc. 10th IAEA Conf. on Plasma Physics and Controlled Nucl. Fusion Research (London,1984) vol.1,29.

[64] P.H.Rebut,D.V.Bartlett,G.Baumel,K.Behringer,R.Behrisch,et al. ; in Proc. 10th IAEA Conf. on Plasma Physics and Controlled Nucl. Fusion (London,1984) vol.1,p.11.

[65] INTOR group ; Nucl.Fusion 25 (1985) 1791

[66] J.M.Dawson,H.P.Furth,F.H.Tenney ; Phys.Rev.Lett. 26 (1971) 1156.

[67] R.J.Goldston ; Plasma Phys. 26 (1984) 87.

[68] C.Andelfinger,K.Büchl,R.S.Lang,H.B.Schilling,M.Ulrich ; Max-Planck Institut für Plasmaphysik, IPP-1/193 (1981)

[69] J.F.Clarke ; Nucl.Fusion 20 (1980) 563.

[70] S.Yamamoto,M.Maemo,N.Suzuki,M.Azumi,S.Tokuda,et al. ; Nucl.Fusion 21 (1981) 993.

[71] W VII-A Team, in Proc. 9th IAEA Conf. on Plasma Physics and Controlled Nucl. Fusion (Baltimore,1982) vol.2,p.241.

[72] K.Uo ; Plasma Phys. 13 (1971) 243.

[73] K.Uo ; Nucl.Fusion 13 (1973) 661.

[74] K.Uo et al. ; Nucl.Instruments and Methods 207 (1983) 151.